

AD-A053 809 OHIO STATE UNIV COLUMBUS AERONAUTICAL AND ASTRONAUTI--ETC F/6 20/4  
ADVANCED TWO-PHASE INVESTIGATION IN AN EROSION-ABLATION FACILITY--ETC(U)  
AUG 77 K D KORKAN, S L PETRIE, T S RICE F33615-76-C-3002

UNCLASSIFIED

AFFDL-TR-77-78

NL

1 OF 2  
AD  
A053809



AD No.

DDC FILE COPY

AD A 053809

AFFDL-TR-77-78

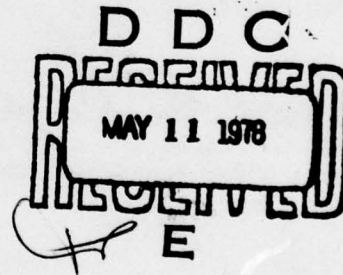
1  
2

## **ADVANCED TWO-PHASE FLOW INVESTIGATION IN AN EROSION-ABLATION FACILITY INCLUDING FLOW DIAGNOSTICS**

*THE AERONAUTICAL AND ASTRONAUTICAL RESEARCH LABORATORY  
THE OHIO STATE UNIVERSITY  
COLUMBUS, OHIO*

AUGUST 1977

TECHNICAL REPORT AFFDL-TR-77-78  
Final Report July 1975 – December 1976



Approved for public release; distribution unlimited.

AIR FORCE FLIGHT DYNAMICS LABORATORY  
AIR FORCE WRIGHT AERONAUTICAL LABORATORIES  
AIR FORCE SYSTEMS COMMAND  
WRIGHT-PATTERSON AIR FORCE BASE, OHIO 45433

NOTICE

When Government drawings, specifications, or other data are used for any purpose other than in connection with a definitely related Government procurement operation, the United States Government thereby incurs no responsibility nor any obligation whatsoever; and the fact that the government may have formulated, furnished, or in any way supplied the said drawings, specifications, or other data, is not to be regarded by implication or otherwise as in any manner licensing the holder or any other person or corporation, or conveying any rights or permission to manufacture, use, or sell any patented invention that may in any way be related thereto.

This report has been reviewed by the Information Office (OI) and is releasable to the National Technical Information Service (NTIS). At NTIS, it will be available to the general public, including foreign nations.

This technical report has been reviewed and is approved for publication.

Kenneth R. Cramer

KENNETH R. CRAMER  
Project Engineer

FOR THE COMMANDER

Alfred C. Draper

ALFRED C. DRAPER  
Assistant for Research & Technology  
Aeromechanics Division

"If your address has changed, if you wish to be removed from our mailing list, or if the addressee is no longer employed by your organization please notify AFFDL/FXE, W-PAFB, OH 45433 to help us maintain a current mailing list".

Copies of this report should not be returned unless return is required by security considerations, contractual obligations, or notice on a specific document.

## UNCLASSIFIED

62201F  
SECURITY CLASSIFICATION OF THIS PAGE (When Data Entered)

19) REPORT DOCUMENTATION PAGE		READ INSTRUCTIONS BEFORE COMPLETING FORM
1. REPORT NUMBER 11) AFFDL-TR-77-78	2. GOVT ACCESSION NO.	3. RECIPIENT'S CATALOG NUMBER
4. TITLE (and Subtitle) 6) Advanced Two-Phase Investigation In An Erosion-Ablation Facility Including Flow Diagnostics.		5. TYPE OF REPORT & PERIOD COVERED Technical-Final Technical July 1975-Dec 1976
7. AUTHOR(s) 10) K. D. Korkan, S. L. Petrie, T. S. Rice, E. McCovey		8. CONTRACT OR GRANT NUMBER(s) 15) F33615-76-C-3002 Pre
9. PERFORMING ORGANIZATION NAME AND ADDRESS OSU The Aeronautical and Astronautical Research Laboratory, The Ohio State University, Columbus, O.		10. PROGRAM ELEMENT, PROJECT, TASK AREA & WORK UNIT NUMBERS 16) 1988-01-19 17) 01
11. CONTROLLING OFFICE NAME AND ADDRESS Air Force Flight Dynamics Laboratory (FXE) Wright-Patterson AF Base, OH 45433		12. REPORT DATE 11) August 1977
14. MONITORING AGENCY NAME & ADDRESS (if different from Controlling Office)		13. NUMBER OF PAGES 88 12) 99p
		15. SECURITY CLASS. (of this report) Unclassified
		15a. DECLASSIFICATION/DOWNGRADING SCHEDULE
16. DISTRIBUTION STATEMENT (of this Report)  Approved for public release; distribution unlimited.		
17. DISTRIBUTION STATEMENT (of the abstract entered in Block 20, if different from Report)		
18. SUPPLEMENTARY NOTES		
19. KEY WORDS (Continue on reverse side if necessary and identify by block number) Particle accelerator, Particle feed system, Laser velocimeter, Signal processor, Hydrogen-air		
20. ABSTRACT (Continue on reverse side if necessary and identify by block number)  Theoretical and experimental research was conducted to investigate the geometrical and fluid mechanical parameters important in the acceleration of solid particles to hypersonic velocities. A combination-heated erosion-ablation facility providing flows with reservoir enthalpies up to 2000 Btu/lb was assembled and techniques for injecting well-controlled amounts of silicon dioxide particles into the nozzle flow were developed. A laser doppler velocimeter was at the nozzle exit. A digital signal processor capable of measuring particle velocities up to 8000 ft/sec was designed and assembled. Performance characteristics of the		

400 111

50B

UNCLASSIFIED

SECURITY CLASSIFICATION OF THIS PAGE(When Data Entered)

20. (cont) various system components are discussed.

UNCLASSIFIED

SECURITY CLASSIFICATION OF THIS PAGE(When Data Entered)

## FOREWORD

This report was prepared by The Aeronautical and Astronautical Research Laboratory of The Ohio State University, Columbus, Ohio and summarizes their work under Contract F33615-76-C-3002. This effort was supported under Project 1988 Aerothermodynamic Simulation Technology & Task 1988-01-19, Aerothermo Simulation Methodology. Dr. L. A. Walchli and Mr. Kenneth R. Cramer of The Thermomechanics Branch of the Air Force Flight Dynamics Laboratory (AFFDL/FXE), Wright-Patterson Air Force Base, Ohio were the contract monitors.

This effort was initiated in July 1975 and completed in December 1976.

The technical report was released for publication by the author in December 1976.

ACCESSION FOR	
NTIS	White Section <input checked="" type="checkbox"/>
DDC	Buff Section <input type="checkbox"/>
UNANNOUNCED	<input type="checkbox"/>
JUSTIFICATION.....	
BY.....	
DISTRIBUTION/AVAILABILITY CODES	
Dist.	AVAIL and/or SPECIAL
A	

## TABLE OF CONTENTS

<u>Section</u>	<u>Page</u>
I      INTRODUCTION	1
II     TWO-PHASE NOZZLE FLOW THEORETICAL ANALYSES	4
A.    OVERALL SYSTEM ANALYSIS	4
B.    NOZZLE DESIGN	9
C.    PARTICLE SIZE EFFECTS	9
D.    COUPLED/UNCOPLED THEORETICAL ANALYSES	12
III    PARTICLE INJECTION SYSTEMS	19
A.    REVIEW OF PARTICLE INJECTION SYSTEMS	19
B.    BENCH-TOP PARTICLE INJECTION FACILITY	19
C.    RESULTS AND ANALYSIS	20
IV    EROSION-ABLATION COMBUSTION TEST FACILITY	35
V    LASER DOPPLER VELOCIMETER	41
A.    LASER	41
B.    OPTICAL ARRANGEMENT	41
C.    AARL SIGNAL PROCESSOR	44
D.    SPECIFICATIONS AND OPERATIONAL CONSIDERATIONS	58
E.    CALIBRATION OF AARL SIGNAL PROCESSOR	62
F.    FILTER SELECTION	62
G.    AARL COMPUTER INTERFACE	67
VI    TWO-PHASE FLOW DIAGNOSTICS	70
A.    TEST CONDITIONS	70
B.    PARTICLE VELOCITY/SIZE ANALYSIS	71
VII   SUMMARY AND CONCLUSIONS	77
APPENDIX A - AARL SIGNAL PROCESSOR WIRING DIAGRAMS	79
APPENDIX B - AARL SIGNAL PROCESSOR PARTS LIST	83
REFERENCES	87

PRECEDING PAGE BLANK-NOT FILMED

## LIST OF ILLUSTRATIONS

<u>Figure</u>	<u>Page</u>
1. Particle Velocity-Total Enthalpy Envelope for Present Multicomponent Study.	2
2. Correlation of 100 $\mu\text{m}$ $\text{SiO}_2$ Particle Velocities at Fixed A/A* Locations for Various Nozzle Half Angles and Throat Radii ( $\alpha = 0, 1.0$ ).	6
3. Maximum Thermodynamic Velocity of $\text{H}_2/\text{Air}$ , $\text{H}_2/\text{O}_2$ , $\text{CH}_4/\text{O}_2$ Mixtures as Functions of Addition of Moles of Helium ( $P_0 = 2500$ psia).	8
4. Volume and Mass Distribution by Particle Class For Particles Used in Present Study.	10
5. Theoretical Particle Velocity for $\text{SiO}_2$ Sample at Nozzle Exit on Centerline ( $L = 2.86$ ft, $\lambda = 0$ ).	11
6. Representative Theoretical $\text{SiO}_2$ Sample Particle Temperature Histories in Selected Nozzle Design.	13
7. Theoretical Particle Temperatures for $\text{SiO}_2$ Sample at Nozzle Exit on Centerline ( $L = 2.86$ ft, $\lambda = 0$ ).	14
8. Coupled to Uncoupled Particle Velocity Ratio as Function of Particle Loading for $\text{SiO}_2$ Sample at Nozzle Exit on Centerline ( $L = 2.86$ ft.).	15
9. Coupled to Uncoupled Particle Temperature Ratio as Function of Particle Loading for $\text{SiO}_2$ Sample at Nozzle Exit on Centerline ( $L = 2.86$ ft.).	17
10. Coupled to Uncoupled Maximum Particle Temperature Ratio on Nozzle Centerline as Function of Particle Loading for $\text{SiO}_2$ Sample.	18
11. Schematic of Bench Top Particle Feed System.	21
12. Particle Injection Bench Top Facility.	22
13. Particle Mass Flow Rate Measurement Schematic.	23
14. Schematic of Fluidized Bed Particle Feed System.	24
15. Nondimensional Intensity Variation for Fluidized Bed.	25
16. Nondimensioned Intensity Variation for Dry Feed Small Tank.	27

LIST OF ILLUSTRATIONS (continued)

<u>Figure</u>	<u>Page</u>
17. Intensity Variation as a Function of Time for Large Tank - 2/3 Particle/H <sub>2</sub> O Mixture by Volume ( $\Delta P = 110$ inches H <sub>2</sub> O).	28
18. Weight Variation as a Function of Time for Large Tank - 2/3 Particle/H <sub>2</sub> O Mixture by Volume ( $\Delta P = 110$ inches H <sub>2</sub> O).	29
19. Mass Flow Rate of H <sub>2</sub> O and H <sub>2</sub> O/Particle Mixtures as a Function of Pressure Differential Between Particle Container and Facility (0.108 in Orifice).	30
20. Weight Variation as a Function for Modified Particle Injector-Motor Activated.	32
21. Components of Modified Particle Injector.	33
22. Modified Particle Injector Installed on Bench Top Facility.	34
23. Schematic of Erosion/Ablation Combustion Facility.	36
24. Erosion/Ablation Facility and Associated Control Panel.	37
25. Electroformed Design Nozzle for Erosion/Ablation Combustion Facility.	38
26. Schematic of Erosion/Ablation Combustion Facility Particle Injection System.	39
27. Modified Particle Injection System Installed on Erosion/Ablation Combustion Facility.	40
28. Optical Schematic for Laser Doppler Velocimeter.	42
29. Optical Arrangement for the Laser Doppler Velocimeter.	43
30. Signal Processor Functional Block Diagram.	46
31. Signal Processor Printed Circuit Board No. 1.	47
32. Signal Processor Printed Circuit Board No. 2.	48
33. Assembled Signal Processor in NIMBIN.	49

LIST OF ILLUSTRATIONS (continued)

<u>Figure</u>	<u>Page</u>
34. Block Diagram of Signal Processor	50
35. Signal Processor Error Circuit.	52
36. Signal Processor Timing Diagrams.	54
37. Output of Comparator 1 (400 KHz Signal).	55
38. Output of Comparator 2 (400 KHz Signal).	55
39. Output of 8 Cycle Counter (2 mHz Signal).	56
40. Output of 4 Cycle Counter (2 mHz Signal).	56
41. Differential 8 Cycle Pulse (2 mHz Signal).	57
42. TAC Output Pulse (2 mHz Signal).	57
43. +8 Error Output (400 KHz Signal).	59
44. -8 Error Output (400 KHz Signal).	59
45. Top Waveform - Processor Output Bottom Waveform - Error Output Amplifier 400 KHz Signal.	60
46. Sample & Hold No. 1 Strobe (400 KHz Signal).	60
47. Top Waveform - Sample & Hold No. 2 (Processor Output). Bottom Waveform - Sample & Hold No. 1 Output (400 KHz Signal).	61
48. Calibration Curve for AARL Signal Processor.	63
49. Signal Processor Filter Network.	66
50. Laser Doppler Velocimeter Signal Processor Computer Interface Block Diagram.	68
51. Fringe Pattern Obtained Utilizing Present Optical Arrangement (Wire Diameter 0.003 inches).	73
52. Typical Doppler Traces of Particles Utilizing Present Optical Arrangement.	74

LIST OF ILLUSTRATIONS (continued)

<u>Figure</u>	<u>Page</u>
53. Particle Diameter/Fringe Spacing Ratio Versus Visibility Function.	75
54. Experimental Values of Particle Velocity/Size for Cold Flow Using Design Nozzle.	76

### LIST OF SYMBOLS

Symbol	Definition
A	Area
$A_*$	Nozzle throat area
C	Specific heat capacity
$C_D$	Drag coefficient based on cross-sectional area
$C_p$	Specific heat at constant pressure
d	Diameter; distance between fringes
$f_g$	$\text{Nu}/\text{Nu}_{\text{Stokes}}$
$f_p$	$C_D/C_{D\text{Stokes}}$
H	Total enthalpy
L	Length
M	Mach number
$\dot{m}$	Mass flow rate
$m$	Molecular weight
N	Number of data samples
Nu	Nusselt number
R	Gas constant
$R^*$	Nozzle throat radius
Re	Reynolds number
r	Radius
T	Temperature
$u, v$	Velocity component along the particle streamline
V	Visibility function
$\bar{V}$	Average mean velocity
W	One half of laser beam width

LIST OF SYMBOLS (continued)

Symbol	Definition
$z$	Axial coordinate
$\alpha$	Mass fraction of helium
$\gamma$	Ratio of specific heats
$\delta$	Fringe spacing
$\delta^*$	Boundary layer displacement thickness
$\epsilon$	Emissivity
$\zeta$	Nozzle half angle
$\theta$	Included angle between dual laser beams
$\lambda$	Particle loading
$\lambda_0$	Primary wavelength of laser
$\mu$	Viscosity
$\rho$	Density
$\sigma$	Stefan-Boltzmann constant; standard deviation
$\omega$	Frequency

Subscripts

$D$	Doppler
$g$	Gas
$i$	Initial
$o$	Total conditions
$p$	Particles and $H_2O$
$\infty$	Freestream

## SECTION I

### INTRODUCTION

Facilities designed to test the ablation response of various materials have been the subject of continuing research. Recently, however, there has been increased interest in erosion by hypervelocity impact within a high temperature environment. For example, both erosion and ablation may occur as a missile encounters a cloud of solid or liquid particles at hypersonic velocities. Such multi-component clouds could contain particles with diameters up to 500  $\mu\text{m}$ . Impact of the particles on the vehicle surface removes surface material through a complex thermo-mechanical process and increases the overall heat transfer rates.

Various facilities have been constructed to simulate certain aspects of hypersonic erosion. Among the most notable are the AEDC Dust Erosion Tunnel (AEDC DET)<sup>(1)</sup>, and the Boeing Hypersonic Wind Tunnel (BHWT)<sup>(2)</sup>. Both of these facilities operate with relatively low reservoir enthalpies so that the ablative character of the hypersonic environment cannot be simulated in the presence of erosion. Recently, however, as an outgrowth of the RHEA studies<sup>(3)</sup>, a facility configuration employing dynamic interaction of solid particles and light gas flows<sup>(4)</sup> has been investigated as a possible technique for supplying a combined erosion-ablation environment.

The purpose of the present studies was to examine in detail the geometrical and fluid mechanical mechanisms important in the acceleration of solid particles to high velocities within a high enthalpy gas stream. The particle velocity - total enthalpy envelope investigated is shown in Figure 1. The high enthalpy gas streams were provided by a hydrogen-air combustor connected to a particle injection chamber and a conical convergent-divergent exhaust nozzle with a low expansion angle. Detailed theoretical analyses were conducted to determine the nozzle configuration and gas conditions which maximize the particle velocities at the nozzle exit. Particular emphases was placed on developing a particle injection system which allowed accurate control of the particle injection rate.

The particle axial velocity and size distributions were examined with a real-fringe laser doppler velocimeter. Because of the high particle velocities and low particle concentrations, conventional frequency tracking techniques for determining particle velocity could not be used. Instead,

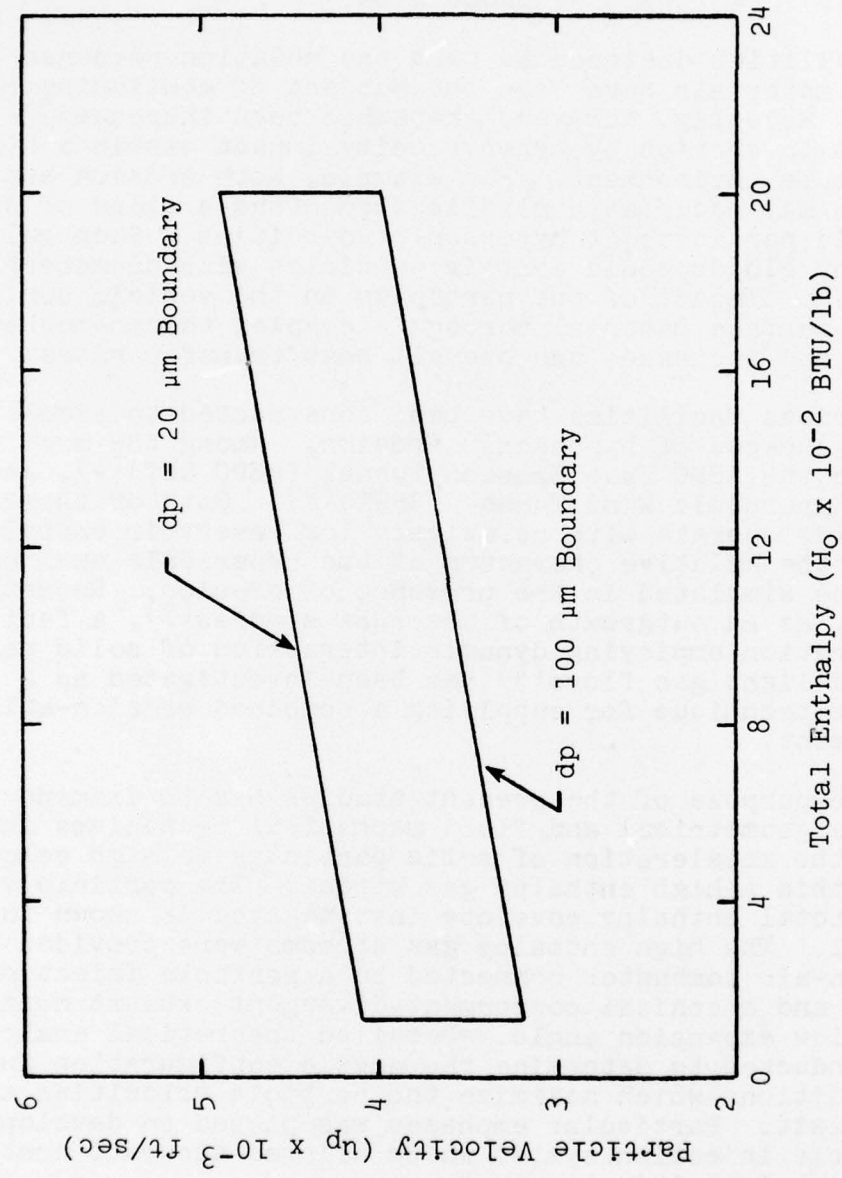


FIGURE 1. PARTICLE VELOCITY-TOTAL ENTHALPY ENVELOPE FOR PRESENT MULTICOMPONENT STUDY.

a digital signal processor was designed and assembled to allow measurement of doppler frequencies up to 90 MHz. The signal processor was interfaced to a high speed digital computer to provide real-time analyses of the particle velocity.

Detailed discussions of the theoretical and experimental analyses are included in the following sections.

## SECTION II

### TWO-PHASE NOZZLE FLOW THEORETICAL ANALYSES

#### A. OVERALL SYSTEM ANALYSIS

A theoretical analysis was conducted to determine the effects of such factors as nozzle geometry, gas flow thermodynamic properties and coupling between the gaseous and particulate flows on the particle velocities at the exit of a convergent-divergent nozzle. A computer program previously developed(5,6) was employed to solve the coupled one-dimensional two-component flow equations(7) in the following form:

$$\frac{du_g}{dz} = \frac{\frac{RT_g}{A} \frac{dA}{dz} - \left(\frac{\lambda}{1-\lambda}\right) \left[ u_g \frac{du_p}{dz} - R \frac{C}{C_{pg}} \frac{dT_p}{dz} - \frac{Ru_p}{C_{pg}} \frac{du_p}{dz} \right]}{u_g \left[ 1 - \frac{R}{C_{pg}} \right] - \frac{RT_g}{u_g}} \quad (1)$$

$$\frac{dT_g}{dz} = - \frac{1}{C_{pg}} \left[ u_g \frac{du_g}{dz} + \left(\frac{\lambda}{1-\lambda}\right) \left( C \frac{dT_p}{dz} + u_p \frac{du_p}{dz} \right) \right] \quad (2)$$

$$\frac{du_p}{dz} = \frac{9}{2} \left[ \frac{u_g f_p}{\rho_p r_p^2} \right] \frac{(u_g - u_p)}{u_p} \quad (3)$$

$$\frac{dT_p}{dz} = \frac{3}{r_p \rho_p C u_p} \left[ \frac{C_{pg} u_g (T_p - T_g) f_g}{r_p} + \epsilon_p \sigma (T_p^4 - T_g^4) \right] \quad (4)$$

In equation (1),  $f_p$  is defined as

$$f_p = \frac{C_D}{C_{D_{\text{Stokes}}}} \quad (5)$$

where  $C_D$  is the drag coefficient of the particles and  $C_{D_{\text{Stokes}}}$  is the drag coefficient in Stokes flow. The sphere drag

coefficient correlation developed earlier by Korkan et al.<sup>(5)</sup> was used. The correlation fits the available experimental data within  $\pm 15\%$  over a wide range of slip Mach numbers (0.1 to 7.0) and Reynolds numbers (4.9 to  $7.7 \times 10^4$ ) and includes the effects of varying particle temperature.

The term  $f_g$  in equation (2) is given by

$$f_g = \frac{N_u}{N_{u \text{stokes}}}$$

and is given by Carlson and Hoglund<sup>(8)</sup> as

$$f_g = \frac{2 + 0.459 \text{ Re}^{0.55}}{1 + 3.42(M/\text{Re})(2 + 0.459 \text{ Re}^{0.55})} \quad (6)$$

Equations (1) - (6) were solved numerically with a digital computer program described in detail in Ref. 5. A number of numerical experiments were performed with the computer program to investigate the particle velocities which could be expected at the exit of a convergent-divergent nozzle. The computations were conducted for two types of facility heating systems: (1) an electrical resistance heater operating with air delivering a maximum reservoir temperature of  $2600^\circ\text{R}$  and (2) a gas combustor operating with a variety of reactants.

The electrical resistance heater is considerably simpler than the combustor system but does not supply the high reservoir temperatures available with the combustor. Previous studies<sup>(9)</sup> indicated that addition of helium to an air flow will increase the maximum velocity appreciably, but requires considerably more electrical power at a given reservoir temperature.

A series of calculations was performed with various mixtures of helium and air for a number of conical nozzle expansion half angles and nozzle throat sizes. Silicon dioxide particles with a diameter of  $100 \mu\text{m}$  were assumed to be injected into the subsonic region of the nozzle and all calculations were conducted for a reservoir pressure and temperature of 2500 psia and  $2600^\circ\text{R}$ , respectively. The particle velocity for various nozzle exit area ratios are shown in Figure 2 as functions of the parameter  $\tan \zeta/R^*$ .

It is evident that the particle velocity is maximized by decreasing the value of  $\tan \zeta/R^*$ . This is accomplished

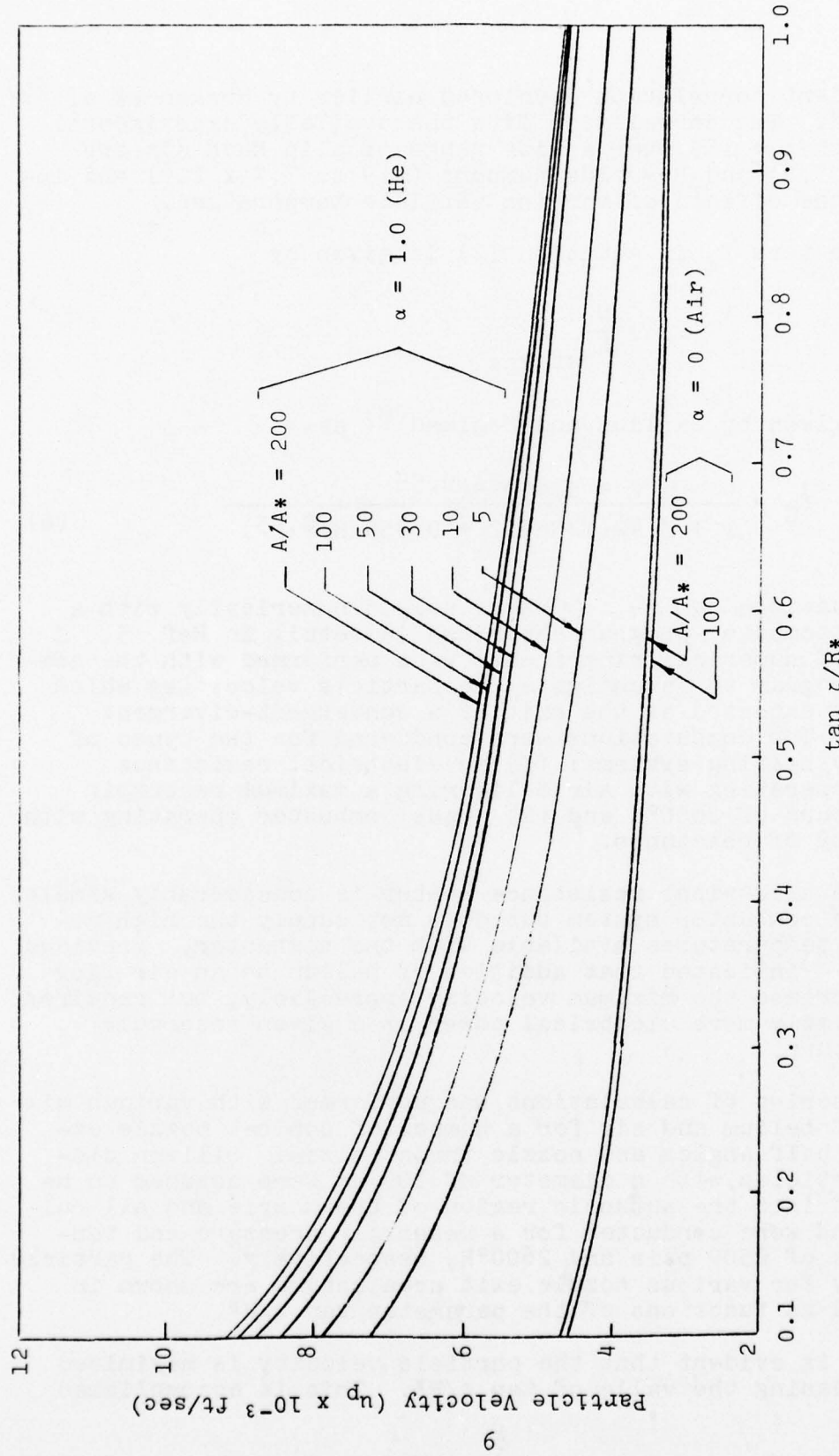


FIGURE 2. CORRELATION OF 100  $\mu\text{m}$   $\text{SiO}_2$  PARTICLE VELOCITIES AT FIXED  $A/A^*$  LOCATIONS FOR VARIOUS NOZZLE HALF ANGLES AND THROAT RADII ( $\alpha = 0, 1.0$ )

by either decreasing the nozzle half angle ( $\zeta$ ) or increasing the throat radius ( $R^*$ ). At a fixed area ratio, decreasing  $\tan \zeta/R^*$  increases the particle resident time in the flow field and leads to a more gradual acceleration of the particles. Hence, decreasing  $\tan \zeta/R^*$  allows the particles more time to respond to the gas velocity increases.

With air, the maximum particle velocity is approximately 5000 ft/sec while with helium velocities near 9000 ft/sec can be achieved. The results also indicate that only small increases in particle velocity result from increasing the nozzle area ratio above approximately 25. Finally, at a fixed nozzle geometry, addition of helium beyond a helium mass fraction of 0.6 leads to little additional increases in particle velocity. Note, however, that a helium mass fraction of 0.6 corresponds to a mole fraction of 0.92 so that the nozzle flow is nearly pure helium at this mass fraction.

Comparable calculations were performed for a combustion heated facility. Stoichiometric mixtures of hydrogen and air, methane and air, and hydrogen and oxygen at a reservoir pressure of 2500 psia were investigated. Adiabatic flame temperatures were calculated with a modification of the computer program described in Ref. 10. The maximum thermodynamic velocities obtained with these combustion systems with varying amounts of helium addition are shown in Figure 3. The maximum thermodynamic velocity is given by  $\sqrt{2}H_o$  and is a measure of the maximum particle velocity which could be expected regardless of the nozzle configuration. For a perfect gas, it can be expressed as  $\sqrt{\frac{2\gamma R}{(\gamma-1)m}}T_o$ .

From Figure 3 it can be seen that little is gained by adding helium in a combustion heated flow. The velocity increase due to the decrease in gas molecular weight resulting from helium addition is offset by the decrease in adiabatic flame temperature ( $T_o$ ).

Particle velocities near 8000 ft/sec were considered adequate in these studies and can be obtained with  $H_2$ -air combustion if a high velocity recovery can be achieved. While  $H_2$ - $O_2$  and  $CH_4$ - $O_2$  combustion systems will yield much higher velocities, the added complexity of handling high pressure (2500 psi) oxygen at high flow rates was not warranted. Hence, the  $H_2$ -air system was selected for further study.

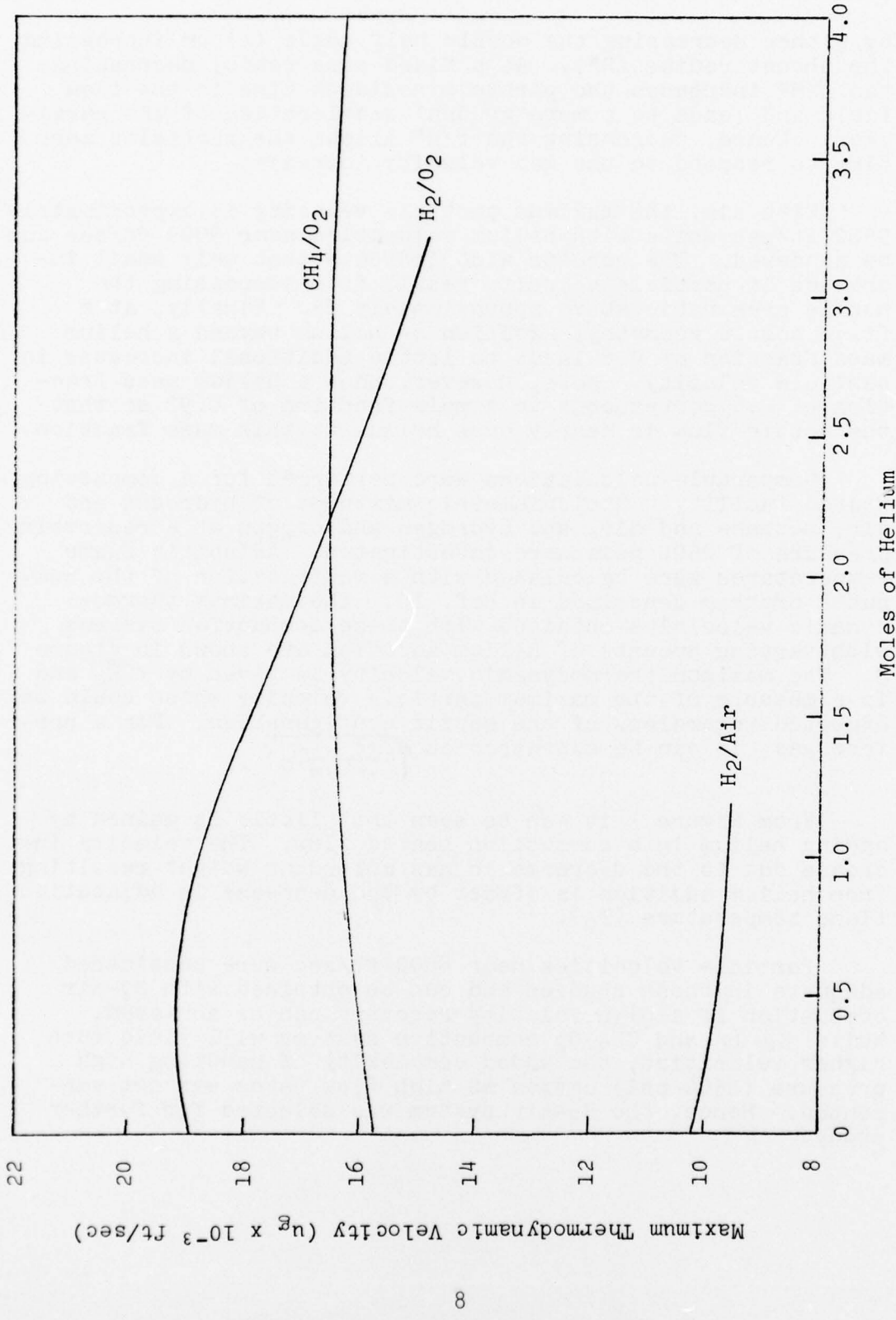


FIGURE 3. MAXIMUM THERMODYNAMIC VELOCITY OF H<sub>2</sub>/AIR, H<sub>2</sub>/O<sub>2</sub>, CH<sub>4</sub>/O<sub>2</sub> MIXTURES AS FUNCTIONS OF ADDITION OF MOLES OF HELIUM ( $P_o = 2500$  psia).

## B. NOZZLE DESIGN

As discussed in the previous section, maximum particle velocities are obtained in a convergent-divergent nozzle by minimizing the parameter  $\tan \zeta/R^*$ . While the nozzle half-angle should be minimized, the nozzle boundary layer should not be allowed to fill the entire flow field. Hence, an analysis of the boundary layer thickness distribution within the nozzle and its effects on the overall flow field was conducted. The empirical correlation developed by Lee<sup>(11)</sup> for the boundary layer displacement thickness in the form

$$\frac{\delta^*}{Z} = \frac{.0064 M^{1.25}}{Re_x^{1.14}} \quad (7)$$

was used and the effects of displacement interaction on the flow field were included.

The minimum reservoir pressure of interest was 600 psia at an H<sub>2</sub>-air adiabatic flame temperature of 3160°R. With a geometric nozzle area ratio of 20 and a throat diameter of 0.10 inches, the nozzle boundary layer will just fill the nozzle at the exit when the nozzle expansion half-angle is 0.50°. This gives an effective inviscid flow half angle of 0.25°, an effective area ratio of 16, a value of  $\tan \zeta/R^*$  of .087 and a nozzle length (throat to exit) of 2.9 feet.

## C. PARTICLE SIZE EFFECTS

Any commercially available solid particle will contain particles with various diameters. The particle velocity distribution at the nozzle exit will depend upon the range of particle sizes injected into the flow. A sample of silica dioxide known as Silica Gel (Grace Chemical Corp.) was analyzed to determine the distribution of particle sizes in a sample with a nominal particle diameter of 100  $\mu\text{m}$ . The results are shown in Figure 4 in terms of particle volume and mass distribution. It can be seen that the particle diameters of the sample range from 20 to 100  $\mu\text{m}$  with an average particle diameter of 80  $\mu\text{m}$ .

The variation in particle size will lead to variations in the particle velocities at the nozzle exit. The particle diameter distribution of Figure 4 was used to compute a velocity distribution at the low pressure design conditions of 600 psia at a reservoir temperature of 3160°R accounted for the presence of the nozzle boundary layer. The results of these studies are given in Figure 5, displayed as a velocity histogram. As expected, the smallest particles have

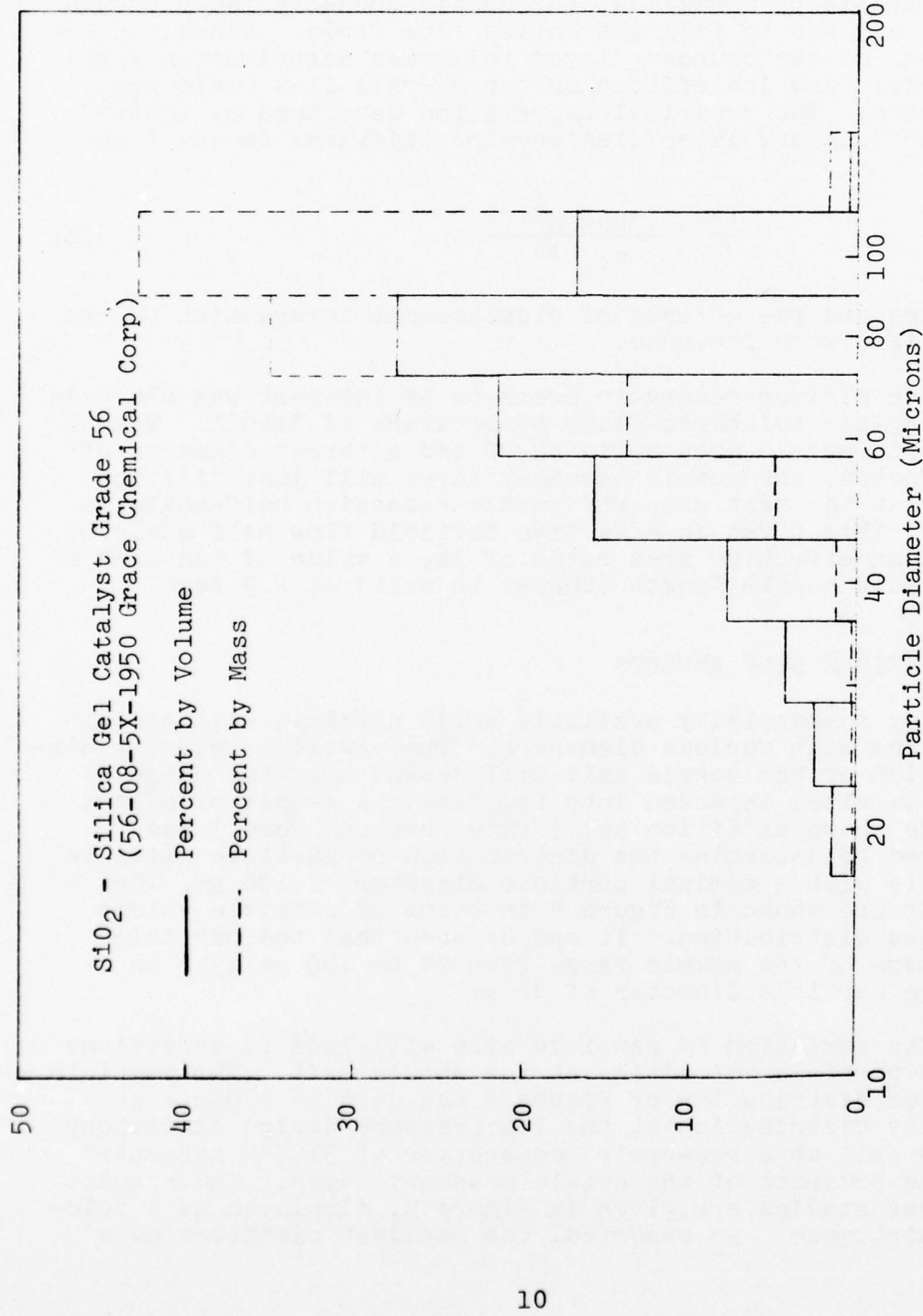


FIGURE 4. VOLUME AND MASS DISTRIBUTION BY PARTICLE CLASS FOR PARTICLES USED IN PRESENT STUDY.

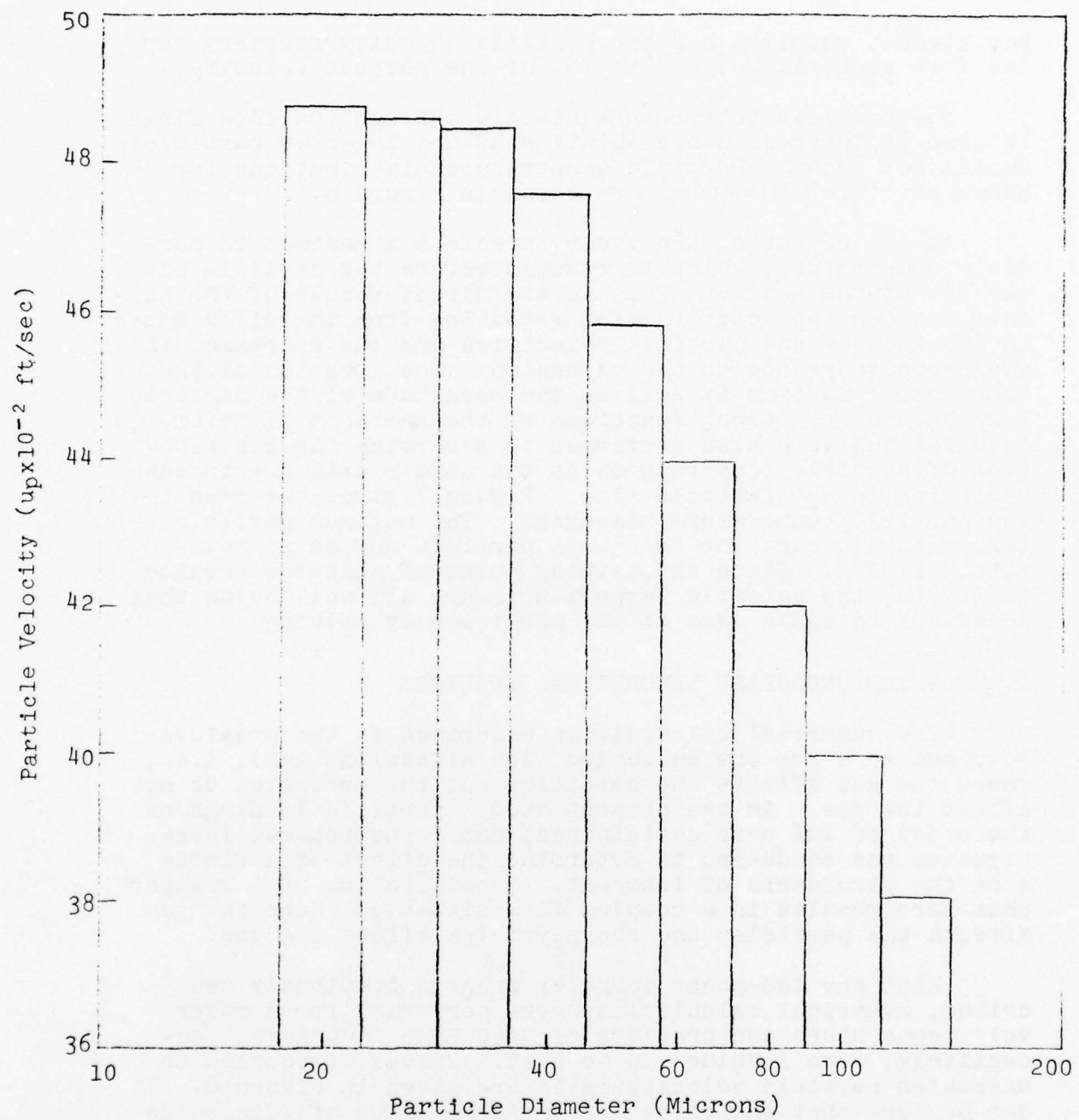


FIGURE 5. THEORETICAL PARTICLE VELOCITY FOR  $\text{SiO}_2$  SAMPLE AT NOZZLE EXIT ON CENTERLINE ( $L = 2.86$  ft,  $\lambda = 0$ )

the highest velocity and the particle velocity recovery varies from approximately 58 to 75% of the gaseous velocity.

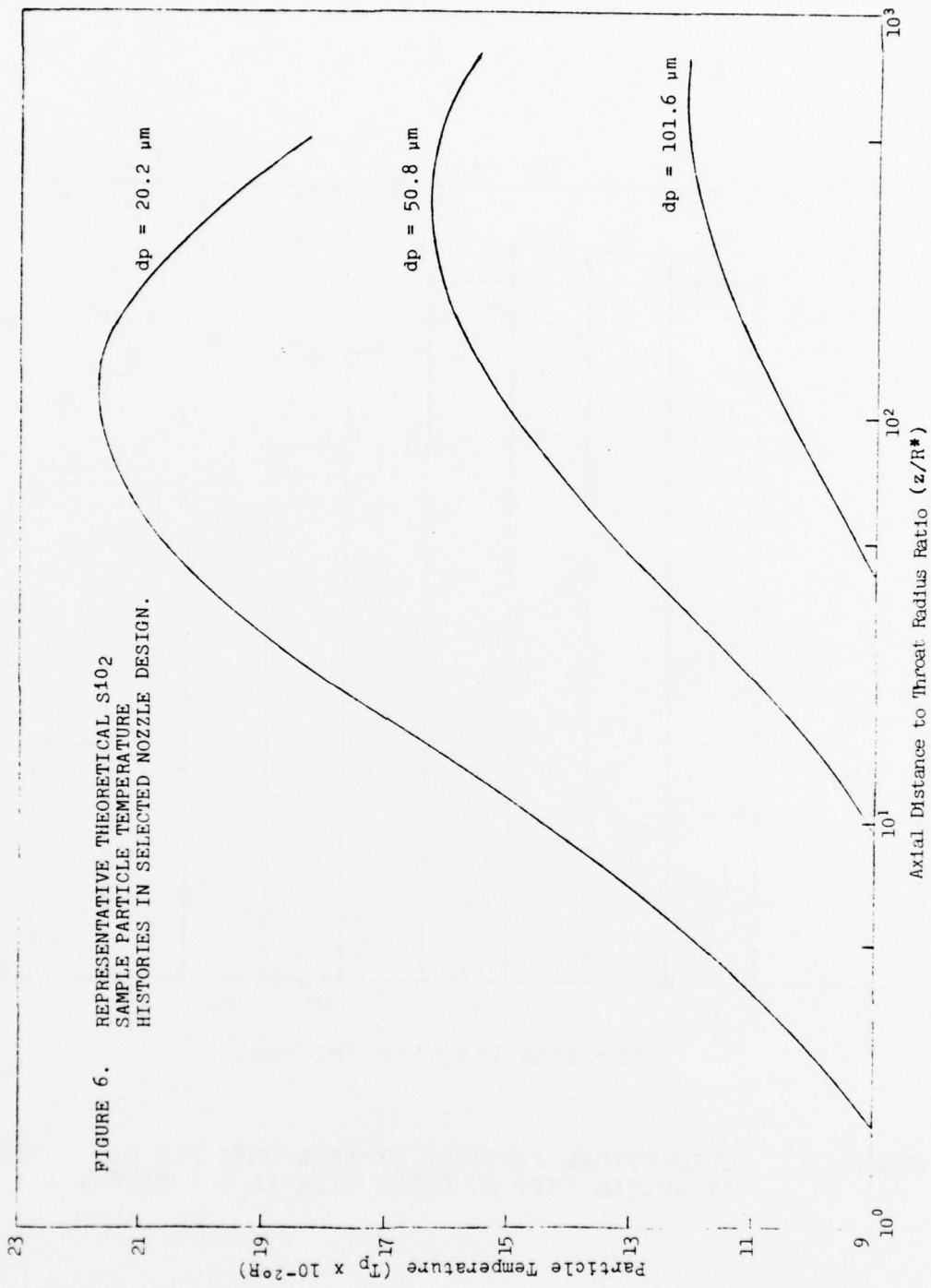
The particle temperature history through the flow field is also of interest since ablation of the injected particles should not occur. Particle temperature distributions for three particle diameters are shown in Figure 6.

As can be noted, the theory predicts a maximum in particle temperature, which is reached before the particle passes out of the nozzle. This is the direct result of the balance between the heat transfer resulting from the differences in the gaseous and particle velocities and the decreases in gas temperature due to the expansion. The location of the temperature maximum as well as the magnitude of the particle temperature are strong functions of the particle diameter. Calculations were also performed to determine the distribution of particle temperatures at the nozzle exit due to the variation in the particle size. Figure 7 gives the resulting particle temperature histogram. The maximum particle temperature occurs for the 30  $\mu\text{m}$  particle and is approximately  $1700^{\circ}\text{R}$ . Since the melting point of silicone deoxide is  $3870^{\circ}\text{R}$ , the particle temperatures are all well below that necessary to cause loss of the particles by melting.

#### D. COUPLED/UNCOPLED THEORETICAL ANALYSES

The numerical calculations described in the previous Sections were for the uncoupled flow situation ( $\lambda=0$ ), i.e., where the gas affects the particles but the particles do not affect the gas. In the present study, particle loadings on the order of 10% were anticipated, and a theoretical investigation was conducted to determine the effect of a finite  $\lambda$  on the parameters of interest. Consideration of  $\lambda$  greater than zero results in a coupled flow situation where the gas affects the particles and the particles affect the gas.

With the two-phase computer program previously described, numerical calculations were performed for a reservoir temperature and pressure of  $3160^{\circ}\text{R}$  and 600 psia, respectively, with  $\lambda$  values up to 0.15. Values of coupled to uncoupled particle velocity ratio are given in Figure 8. It can be seen that the effect of a finite value of  $\lambda$  is to decrease the predicted particle velocity. Further, the results indicate that as the particle diameter is increased from 20.2  $\mu\text{m}$  to 32.0  $\mu\text{m}$ , the effect of  $\lambda$  becomes more severe. That is, at a  $\lambda$  of 0.15 for a particle diameter of 32.0  $\mu\text{m}$ , the particle velocity would be over-predicted by approximately 9% with the uncoupled flow solution. However, as the particle diameter increases above 32.0  $\mu\text{m}$ , the effect of  $\lambda$



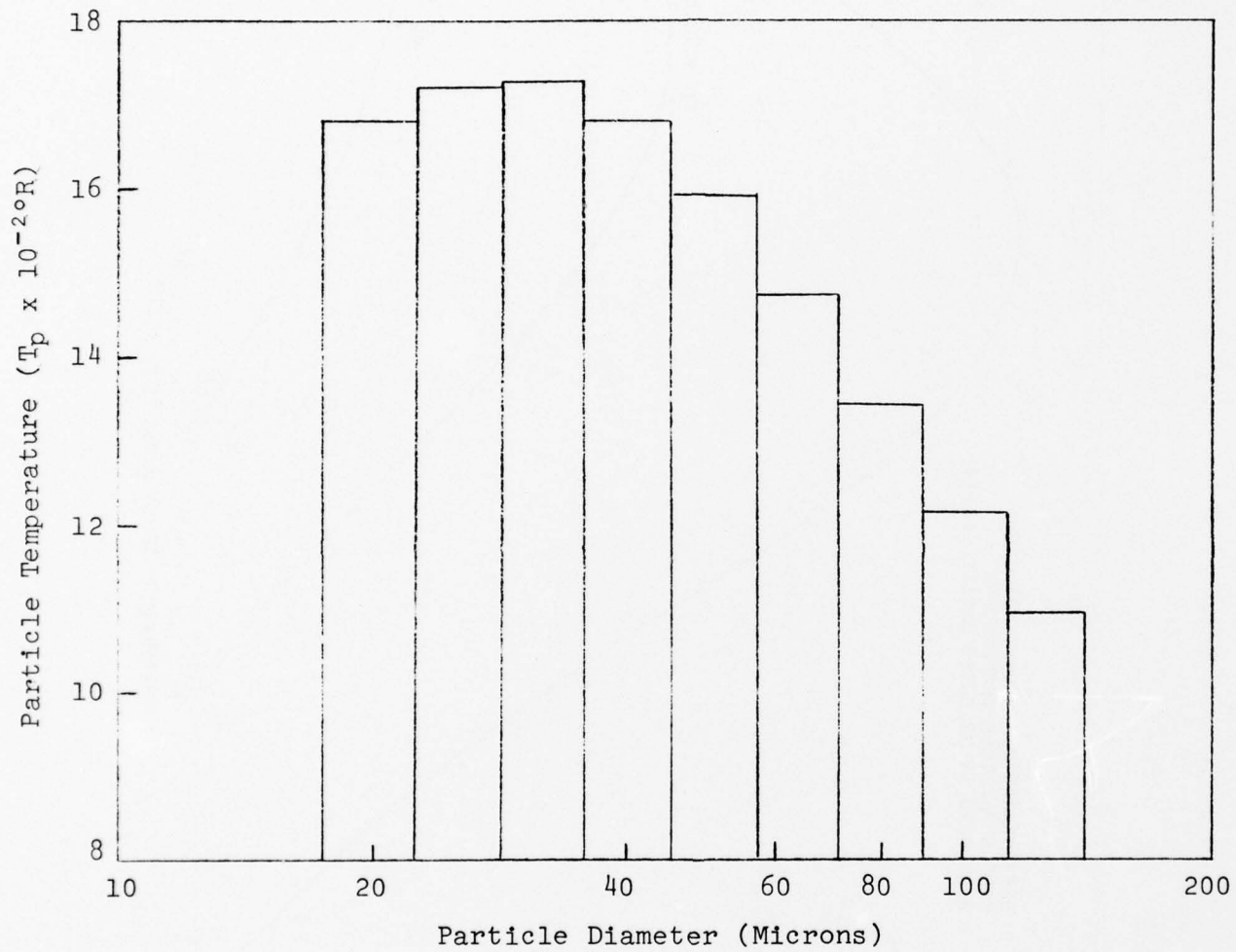


FIGURE 7. THEORETICAL PARTICLE TEMPERATURES FOR  $\text{SiO}_2$  SAMPLE AT NOZZLE EXIT ON CENTERLINE ( $L = 2.86 \text{ ft}$ ,  $\lambda = 0$ )

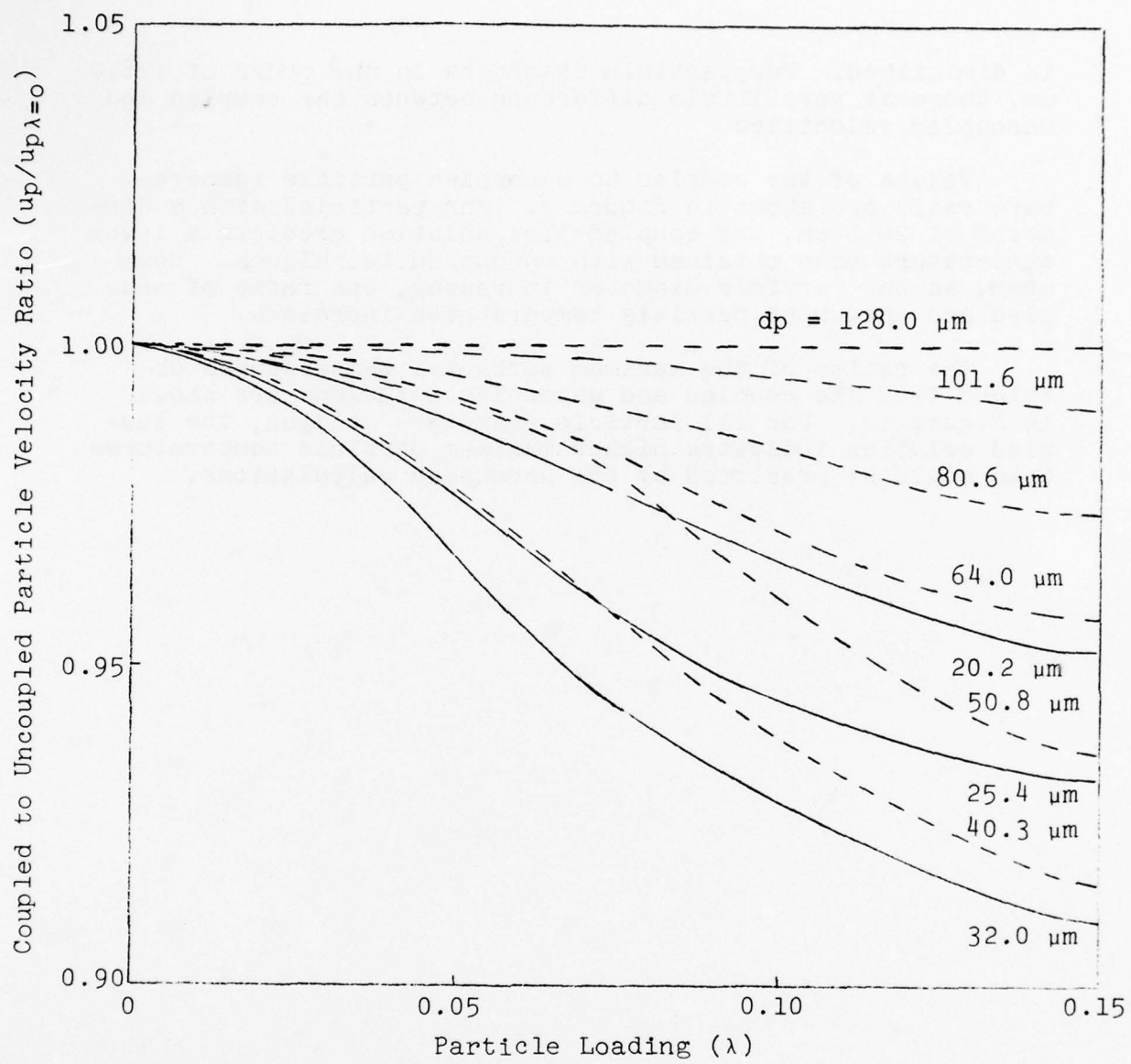


FIGURE 8. COUPLED TO UNCOUPLED PARTICLE VELOCITY RATIO AS FUNCTION OF PARTICLE LOADING FOR  $\text{SiO}_2$  SAMPLE AT NOZZLE EXIT ON CENTERLINE ( $L = 2.86$  ft).

is diminished. For particle diameters on the order of 128.0  $\mu\text{m}$ , there is very little difference between the coupled and uncoupled velocities.

Values of the coupled to uncoupled particle temperature ratio are shown in Figure 9. For particles with a diameter of 20.2  $\mu\text{m}$ , the coupled flow solution predicts a lower temperature than obtained with uncoupled techniques. However, as the particle diameter increases, the ratio of coupled and uncoupled particle temperatures increases.

The ratios of the maximum particles temperatures obtained from the coupled and uncoupled solutions are shown in Figure 10. For all particle diameters studied, the coupled solution indicates higher maximum particle temperatures than would be predicted by the uncoupled calculations.

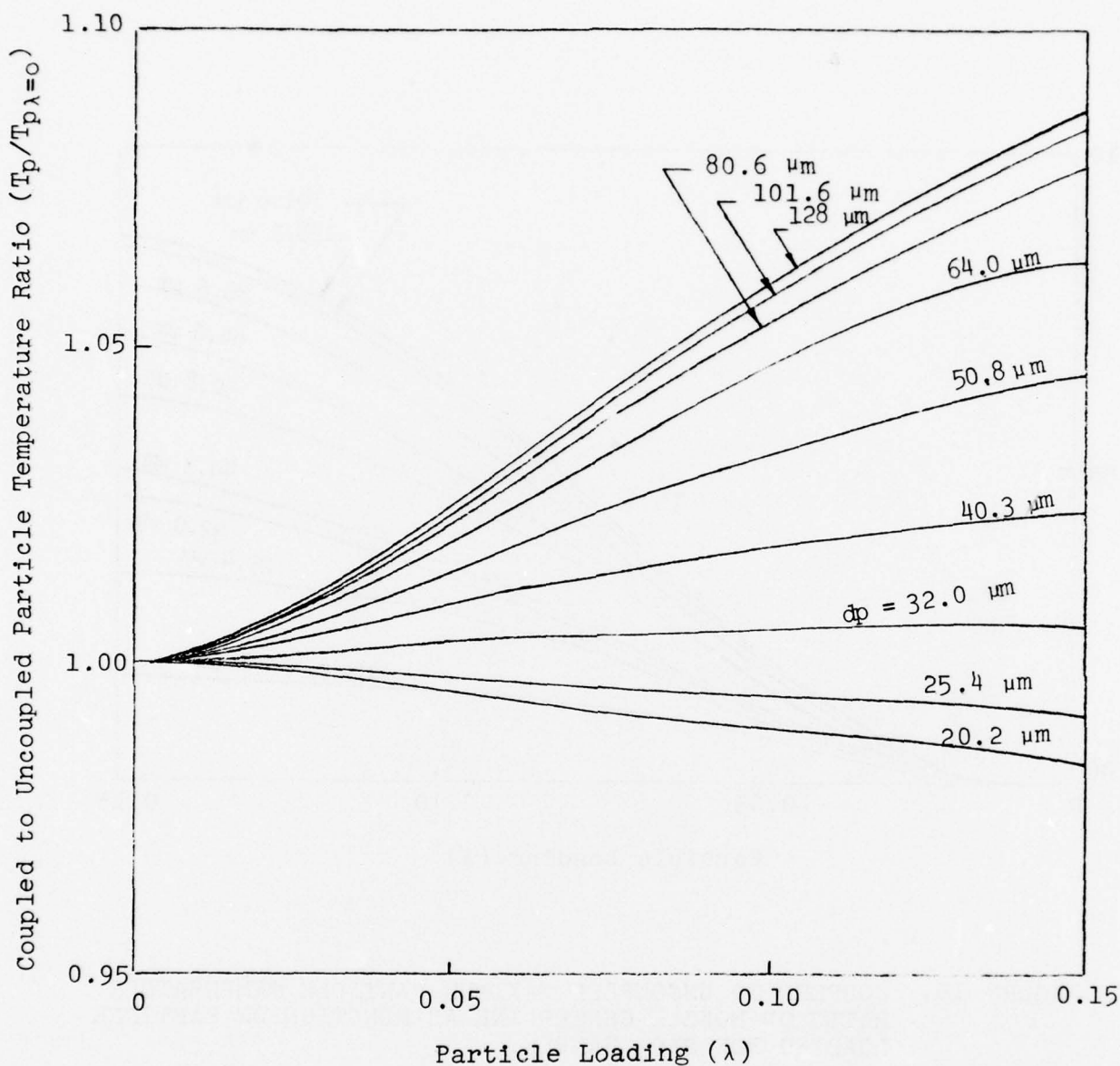


FIGURE 9. COUPLED TO UNCOUPLED PARTICLE TEMPERATURE RATIO AS FUNCTION OF PARTICLE LOADING FOR  $\text{SiO}_2$  SAMPLE AT NOZZLE EXIT ON CENTERLINE ( $L = 2.86$  ft).

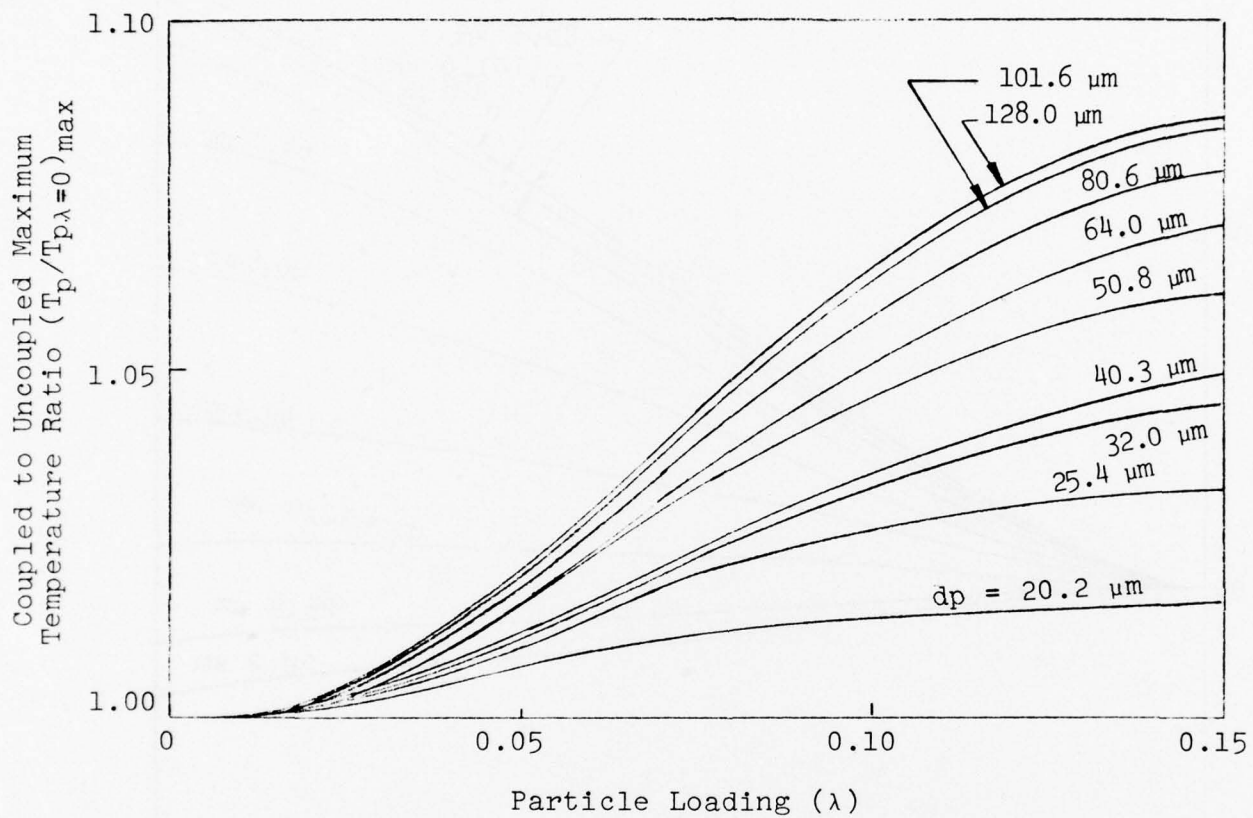


FIGURE 10. COUPLED TO UNCOUPLED MAXIMUM PARTICLE TEMPERATURE RATIO ON NOZZLE CENTERLINE AS FUNCTION OF PARTICLE LOADING FOR  $\text{SiO}_2$  SAMPLE.

## SECTION III

### PARTICLE INJECTION SYSTEMS

#### A. REVIEW OF PARTICLE INJECTION SYSTEMS

In dealing with multicomponent flows, the injection of particles into a flowing stream with good control of the particle flow rate is a formidable problem. Various techniques have been devised which apply in different particle flow rate ranges. However, in the present study, the particles must be injected into a high enthalpy stream and particles with relatively large diameters must be employed. A review of particle injection techniques is given in Ref. 12 and several of these techniques are discussed below.

The simplest particle injection system consists of a conical hopper where a pressure differential is created by reducing the pressure in the feed tube with a venturi. It is recommended that the angle of the side walls be equal to or greater than the angle of repose for the particles and an agitator should be used to reduce clogging. However, the venturi limits the pressure ratio available across the particle supply tank.

A lead screw which carries the particles from the container to the feed tube can be used to increase the controllability of the particle flow rates. The conical hopper in this device is pressurized and the particle feed rate can be controlled by the particle container pressure ratio and the speed of the lead screw. However, rotating seals for the lead screw must be used and can cause difficulties in a high enthalpy test facility.

The vortex pump has been used extensively to transfer powder to and from vortex chambers. It consists of a cylindrical chamber with air injected tangentially which creates a vortex. In this device, the particle flow rates can be controlled by the air pressure driving the vortex. However, the complexity of the system is a major drawback. The design must be optimized for a given particle size to achieve maximum pumping efficiency.

#### B. BENCH-TOP PARTICLE INJECTION FACILITY

A bench-top particle injection facility for testing various particle injection techniques was assembled. Various particle injector methods were tested with the intent of developing a technique suitable for use with an erosion-ablation test facility with particle flow rates up to 10% of the facility mass flow rate.

The bench-top facility is shown in Figures 11 and 12. It consists of a conical nozzle with an exit Mach number of approximately 3.6 ( $A/A^* \approx 7.3$ ) exhausting as a free jet. A Barton pressure differential gauge was installed to accurately measure the difference in the total pressure of the facility and that of the particle container. The flow of particles was regulated by the differential pressure supplied to the particle container and an orifice located in the feed tube. Various orifice sizes were used and it was found that the orifice size controls the sensitivity of the particle mass flow rate to the applied pressure differential. While small orifices were subject to clogging, the particle flow through large orifices was less controllable. Orifice sizes from 0.1 to 0.25 inches were found to be optimum for the particle size range of interest here.

Laser scattering techniques were employed to measure the time history of the particle flow through a point on the free jet centerline one inch downstream of the nozzle exit plane. A 3 mw helium-neon laser was projected across the free jet and the scattered light from the particles was collected and measured with a 1P28A photomultiplier tube. The signal was preamplified and sent to an A/D converter where it was digitally sampled and displayed in real time on a cathode ray tube.

To obtain the particle mass flow rates, the variation of the weight of particle container with time was measured with the instrumentation system shown schematically in Figure 13. The mass of the container and particles was monitored by a strain gage arrangement placed on a thin wafer attached to a cantilever beam. To reduce beam vibrations, a small oil dashpot was attached to the end of the beam. The signal was conditioned with a portable Consolidated Engineering Corporation Type 8-108 unit, preamplified, and digitized.

### C. RESULTS AND ANALYSIS

Because of the success achieved on a previous study (3) with a fluidized bed particle feed system, this was the first injector to be tested on the bench-top facility. The test configuration, identical to that of Reference 3, is shown schematically in Figure 14. The variation of scattered laser light versus time is shown in Figure 15. The fluidized bed injector typically exhibits a large initial burst of particles, followed by a severe drop in particle mass flow rate to constant level which persists until the supply of particles is

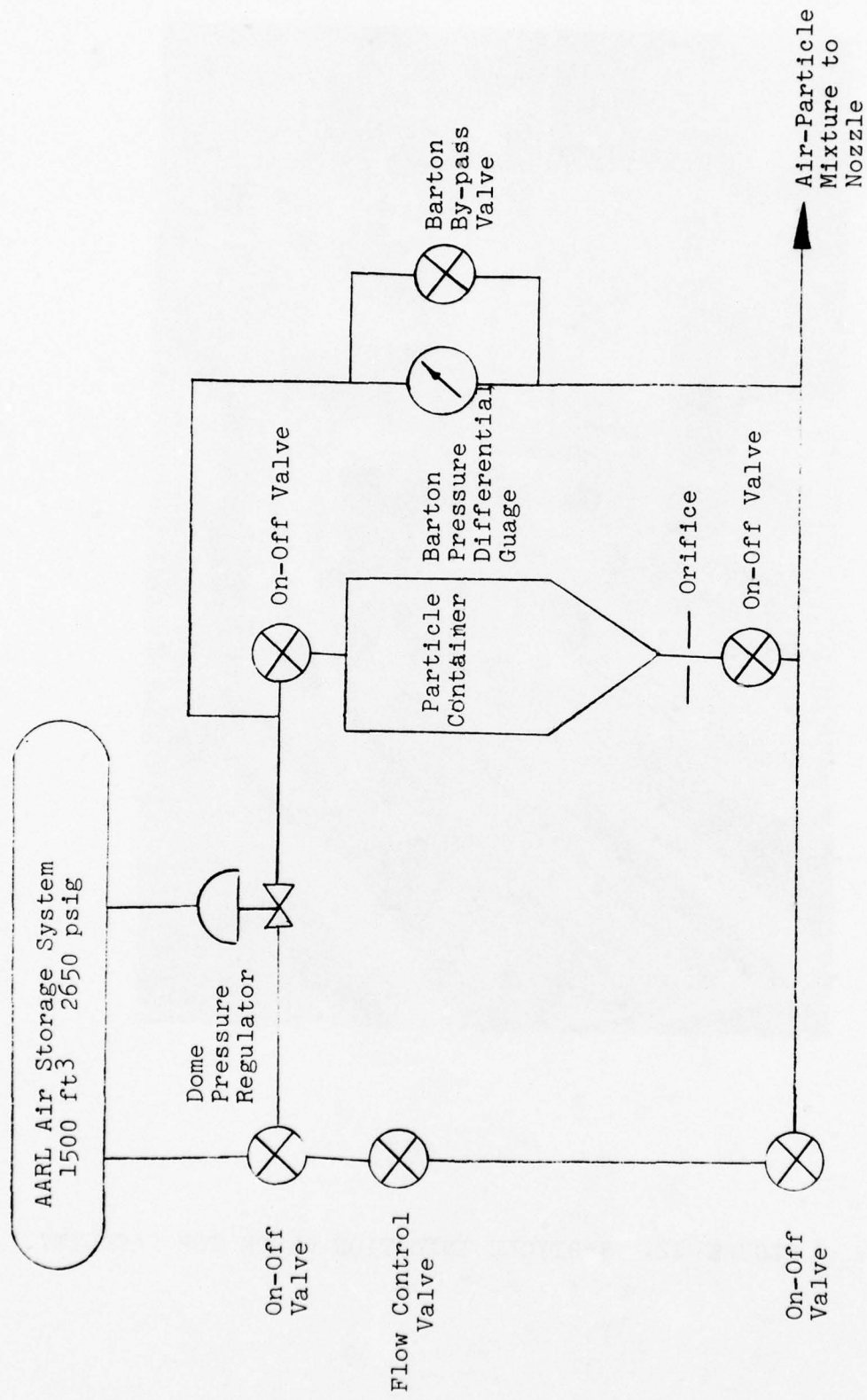


FIGURE 11. SCHEMATIC OF BENCH TOP PARTICLE FEED SYSTEM.

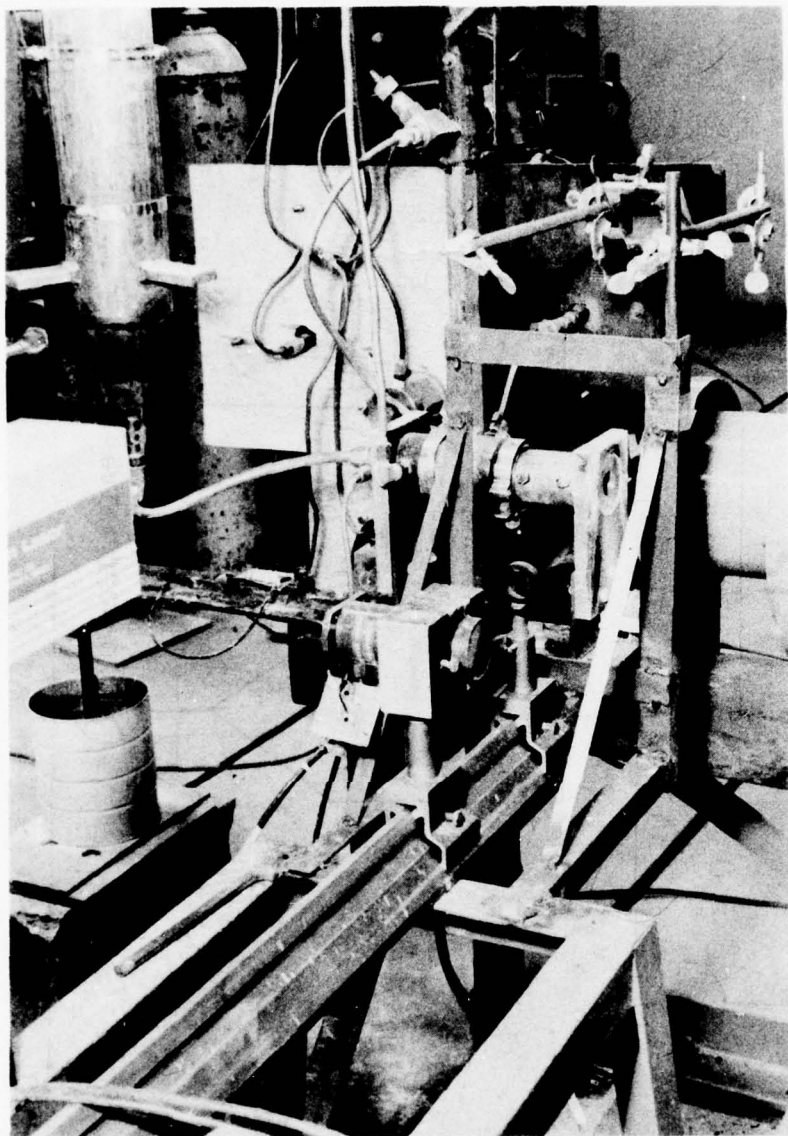


FIGURE 12. PARTICLE INJECTION BENCH TOP FACILITY.

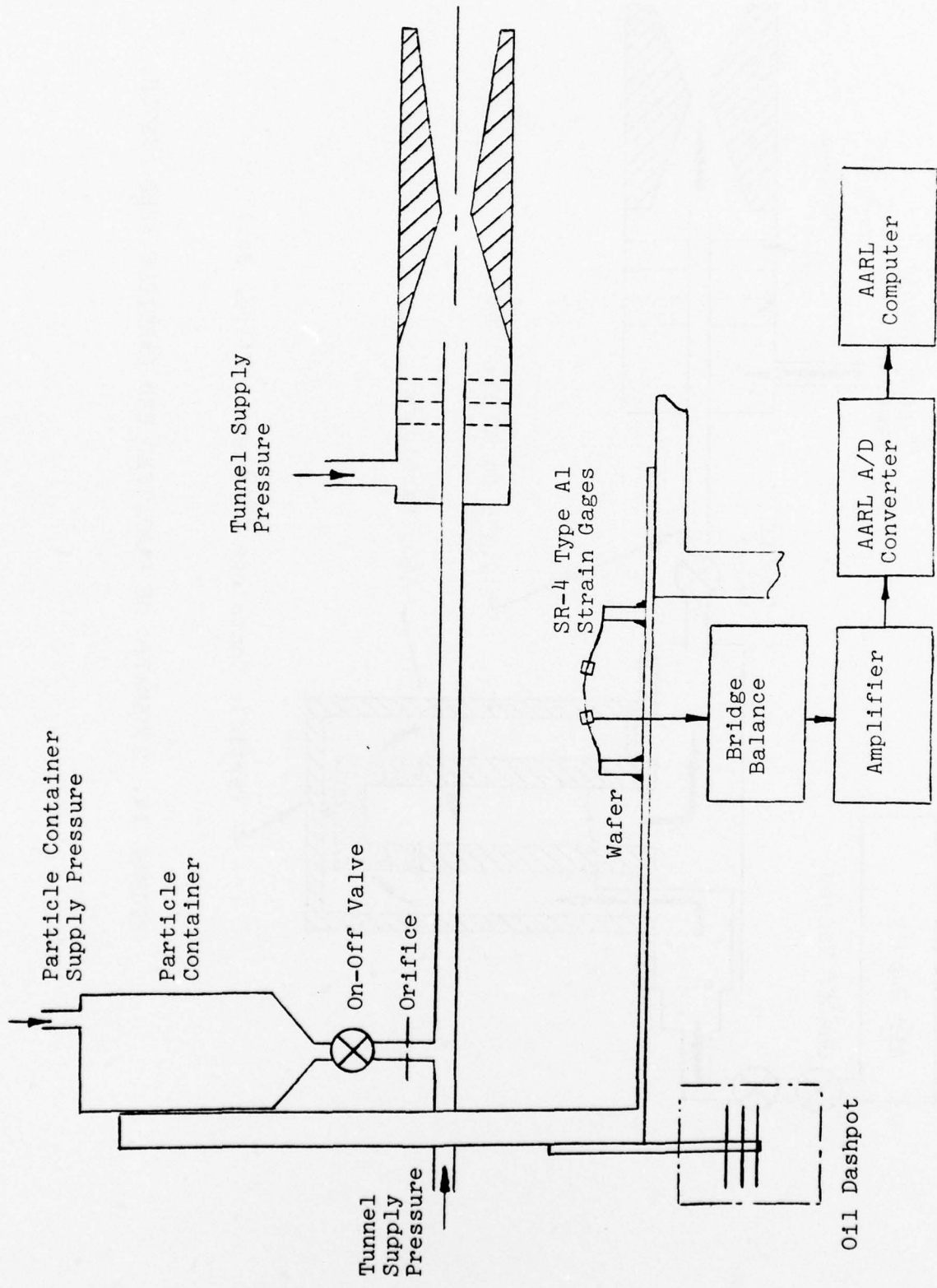


FIGURE 13. PARTICLE MASS FLOW RATE MEASUREMENT SCHEMATIC.

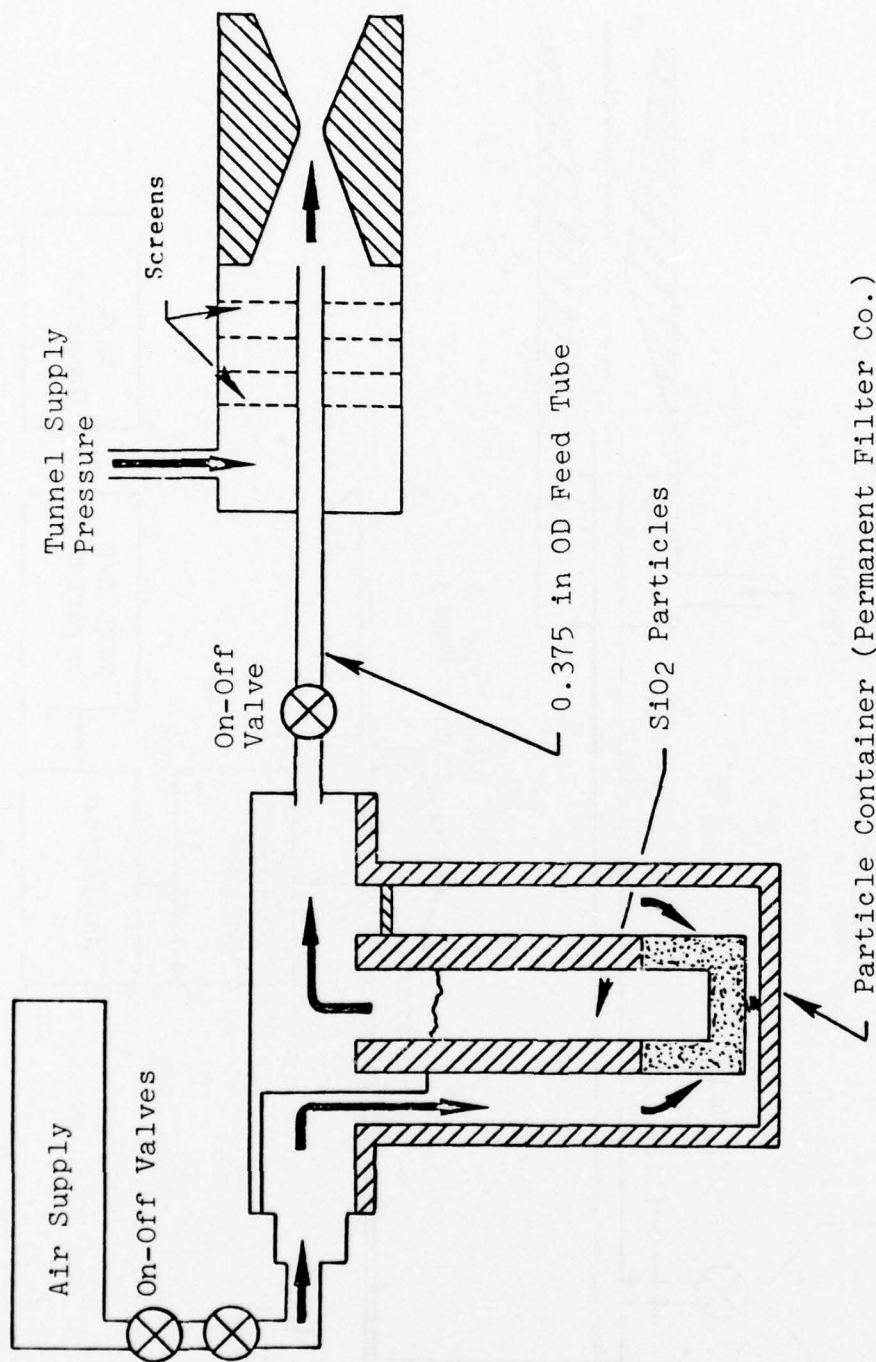


FIGURE 14. SCHEMATIC OF FLUIDIZED BED PARTICLE FEED SYSTEM.

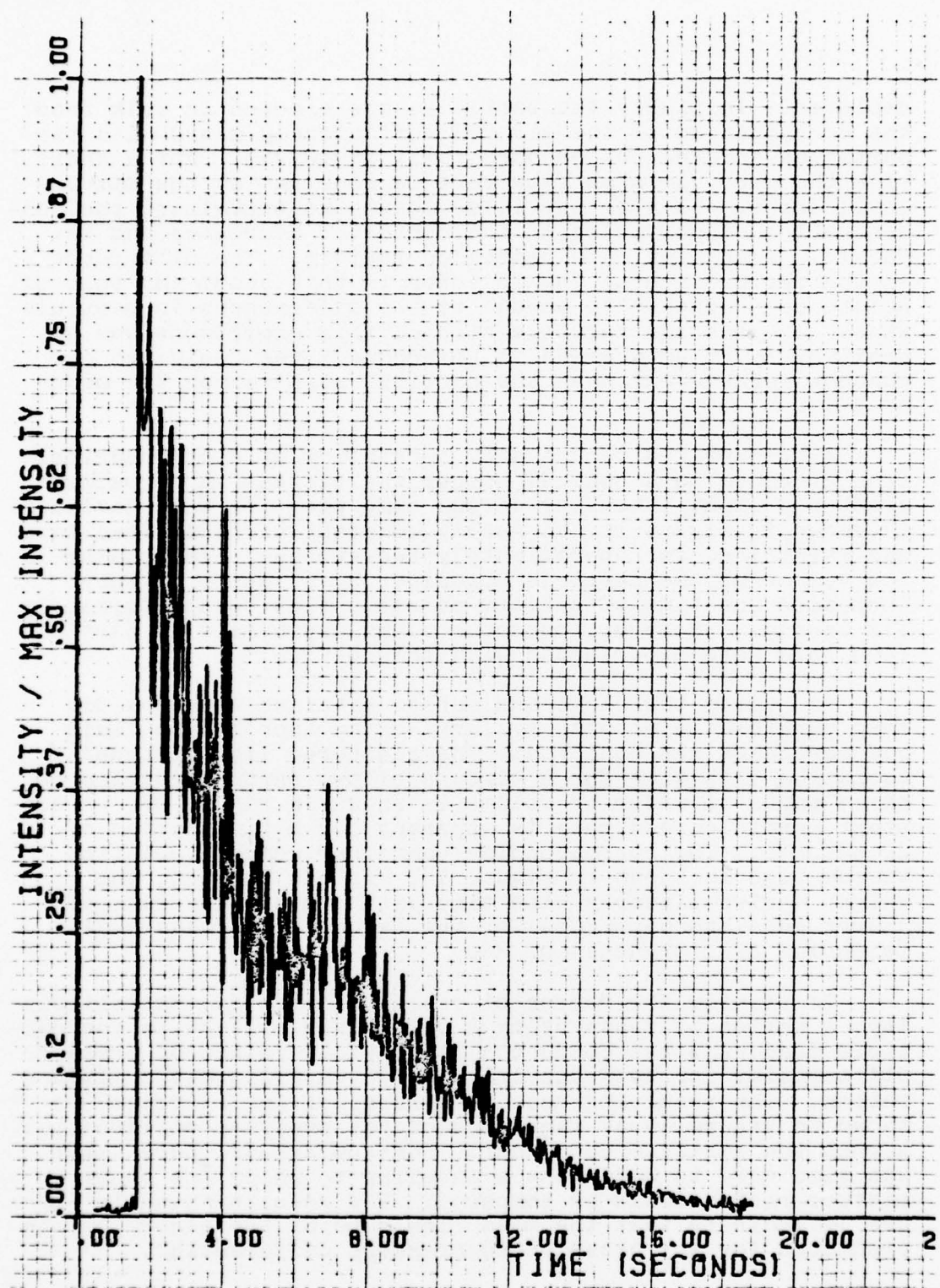


FIGURE 15. NONDIMENSIONAL INTENSITY VARIATION  
FOR FLUIDIZED BED.

depleted. Initially the particles are ejected in bulk from the container until the air has sufficiently mixed with the particles and the bed becomes fully fluidized. For a short time the particle mass flow rate is constant as the mixture level drops. As more particles leave the container, the concentration of particles in the container decreases and the particle mass flow rate decreases rapidly. The difference in the performance of the injector in this study and that of Reference 5 appears to be due to the differences in particle size. The average particle size of this experiment was approximately 80  $\mu\text{m}$  whereas in Reference 5 the fluidized bed concept worked well when the particle size was on the order of 1  $\mu\text{m}$ .

A pressurized tank system consisting of a cylindrical tank attached to a conical hopper was tested. A normalized scattered light intensity versus time plot for this device is shown in Figure 16. A nearly constant particle feed rate was maintained for approximately two seconds. Increasing the volume of the particle container by a factor of four increased the time of uniform particle flow to approximately six seconds. However, numerous clogs and bursts in particle feed rate were experienced with this device.

To reduce the clogs and bursts obtained with the dry feed particle injectors, a slurry of an appropriate fluid and particles was employed. The scattered light intensity variation with time for a mixture of two parts particles to three parts of water by volume is shown in Figure 17. A constant particle feed rate is apparent for a time period of 22 seconds. The corresponding container weight variation versus time is shown in Figure 18. As can be seen, the weight varied linearly with time with a mass flow rate of slurry equal to 93gm/sec, for the associated pressure differential of 110 inches of  $\text{H}_2\text{O}$ .

To examine the degree of repeatability and controllability, a series of tests using a 0.108-inch orifice in the particle feed tube was conducted for various values of pressure differential for both the 1/1 and 3/2 water/particle mixture ratios. The resulting mass flow rates of the slurries are shown in Figure 19 as functions of the pressure differential across the particle container. For comparison, pure water was also used to determine a baseline to which the other mixture ratios could be compared. The results shown in Figure 19 indicate that the mass flow rate of the slurry can be predicted for any preselected pressure differential.

The only significant problem encountered with the slurries was associated with settling of the particles within the container. To eliminate settling, the particle injector

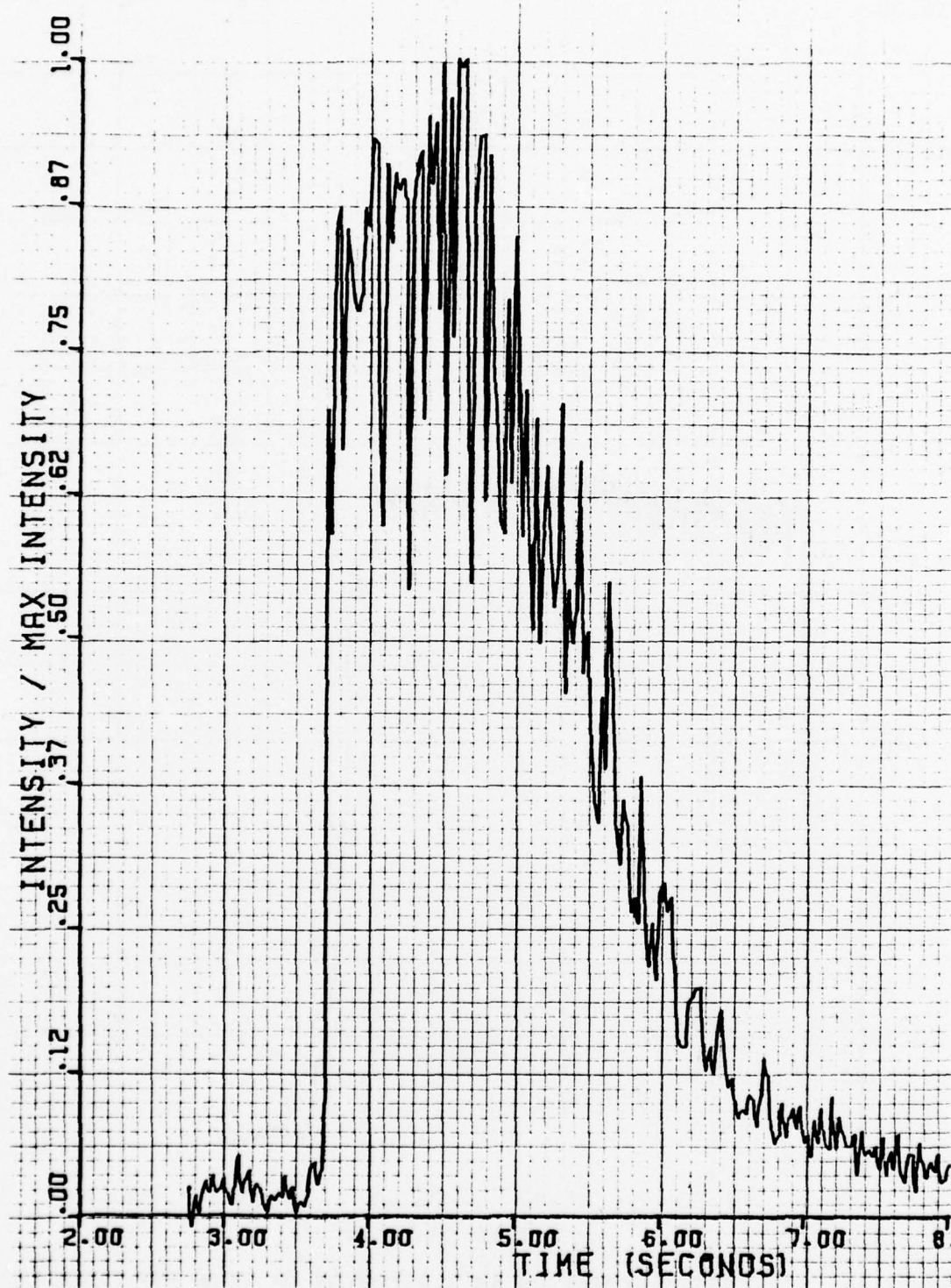


FIGURE 16. NONDIMENSIONALIZED INTENSITY VARIATION  
FOR DRY FEED SMALL TANK.

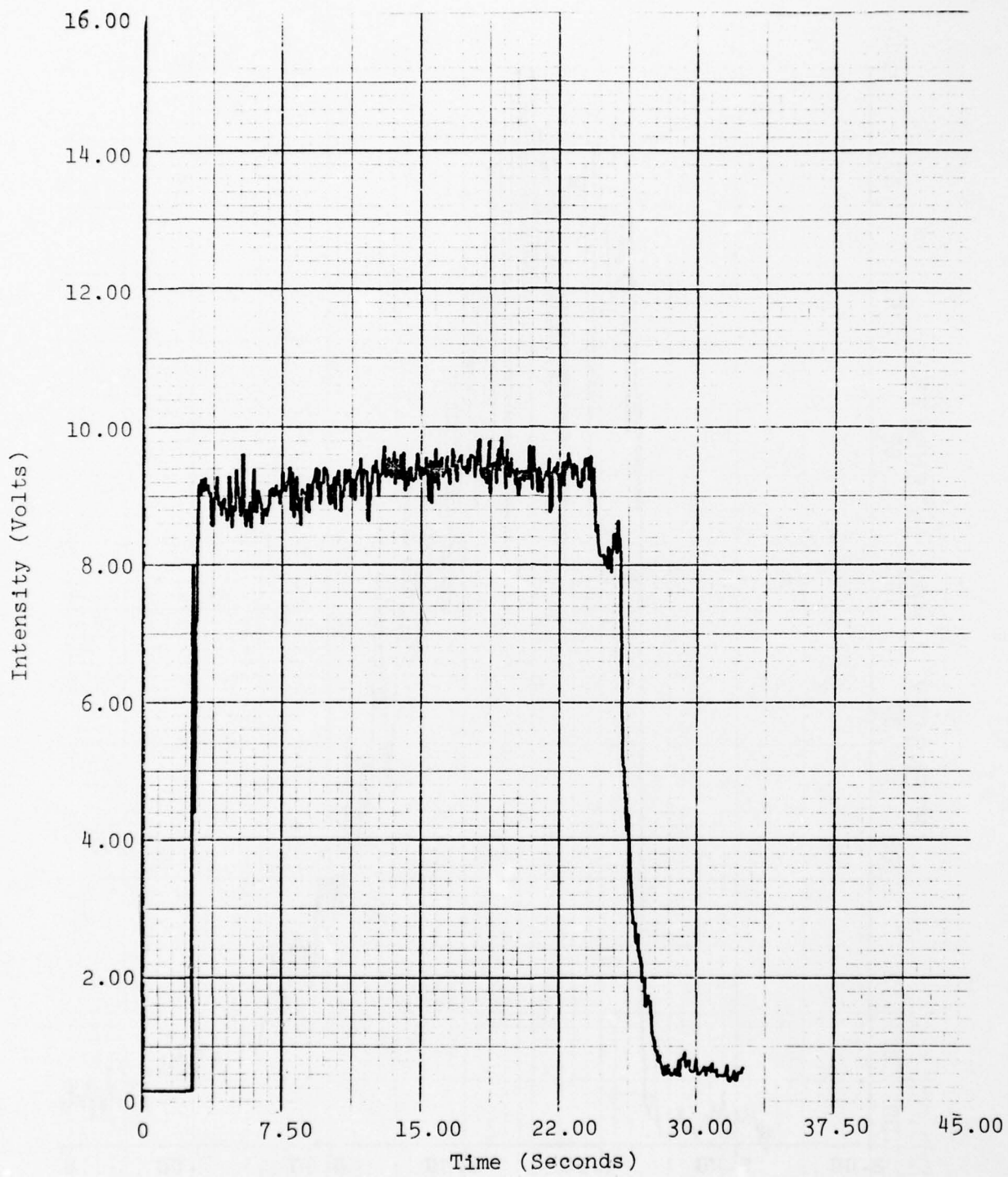


FIGURE 17. INTENSITY VARIATION AS A FUNCTION OF TIME FOR LARGE TANK -  
2/3 PARTICLE/H<sub>2</sub>O MIXTURE BY VOLUME ( $\Delta P = 110$  inches H<sub>2</sub>O)

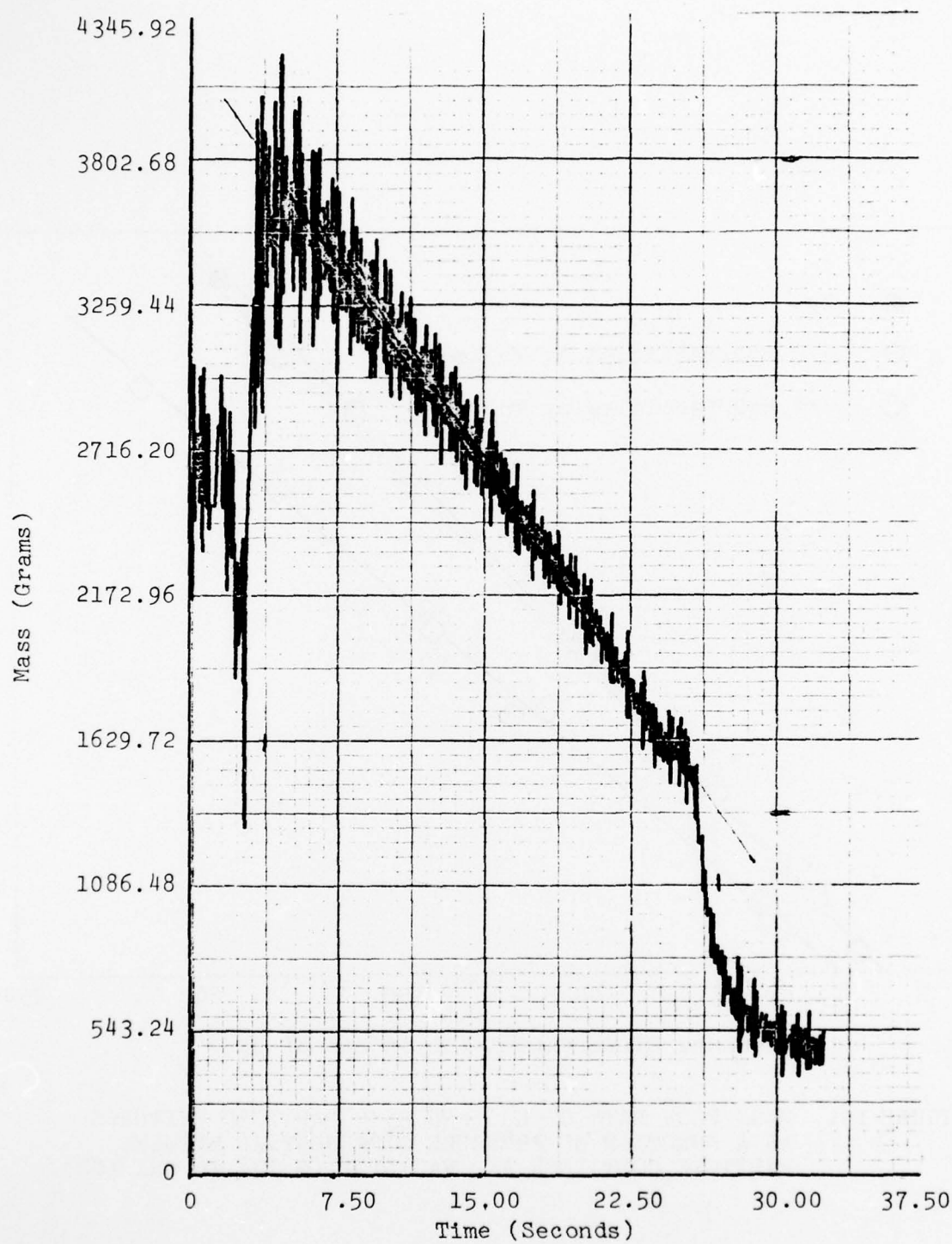


FIGURE 18. WEIGHT VARIATION AS A FUNCTION OF TIME FOR LARGE TANK -  
2/3 PARTICLE/H<sub>2</sub>O MIXTURE BY VOLUME ( $\Delta P = 110$  inches H<sub>2</sub>O)

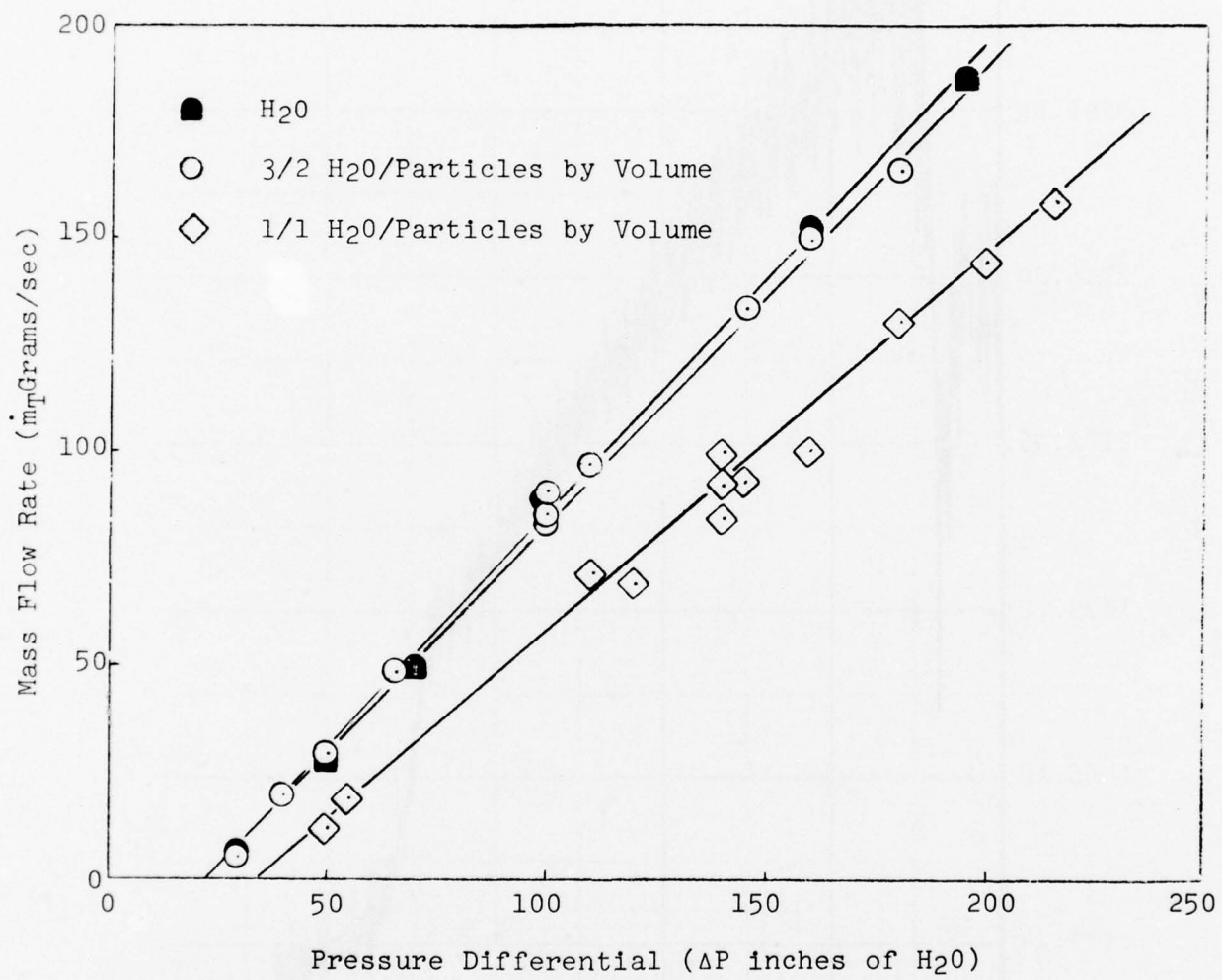


FIGURE 19. MASS FLOW RATE OF  $H_2O$  AND  $H_2O/$  PARTICLE MIXTURES AS A FUNCTION OF PRESSURE DIFFERENTIAL BETWEEN PARTICLE CONTAINER AND FACILITY (0.108 in ORIFICE).

was modified by the addition of a motor equipped with a shaft and propeller. During operation, the motor and propeller were run continuously at 1000 RPM in the particle container to keep the particle suspended in the liquid. This modification to the particle injector added considerable mass to the system and required a counterbalance to maintain the required sensitivity of the strain gage-cantilever beam configuration. Operation of the motor introduced additional vibrations into the system, reducing the signal to noise ratio in the mass-measuring instrumentation system. However, as shown in Figure 20, the weight variation as a function of time indicates sufficient sensitivity with an easily defined slope of mass versus time. The components of the particle injector are shown in Figure 21 and the system is shown assembled in the bench-top facility in Figure 22.

The results indicate that the use of a slurry consisting of  $\text{SiO}_2$  particles and  $\text{H}_2\text{O}$  in a volume ratio of 1/1 within a pressurized particle container equipped with an orifice and mixer results in a particle injection system with well controlled particle flow rates. Experimental correlations have been determined to give the particle mass flow rate as a function of pressure differential which can be applied to other facilities.

Although  $\text{H}_2\text{O}$  was used as the fluid, any appropriate liquid could be used to create the necessary suspension as long as the particles are not soluble in the fluid. When mixed properly, there was no evidence of coagulation and there did not appear to be any effects on the particle size distribution. It may be noted that when a slurry is used in a facility such as an erosion-ablation test configuration where relatively high gas temperatures are experienced, the fluid probably evaporated, releasing the particles to the main stream early in the expansion process.

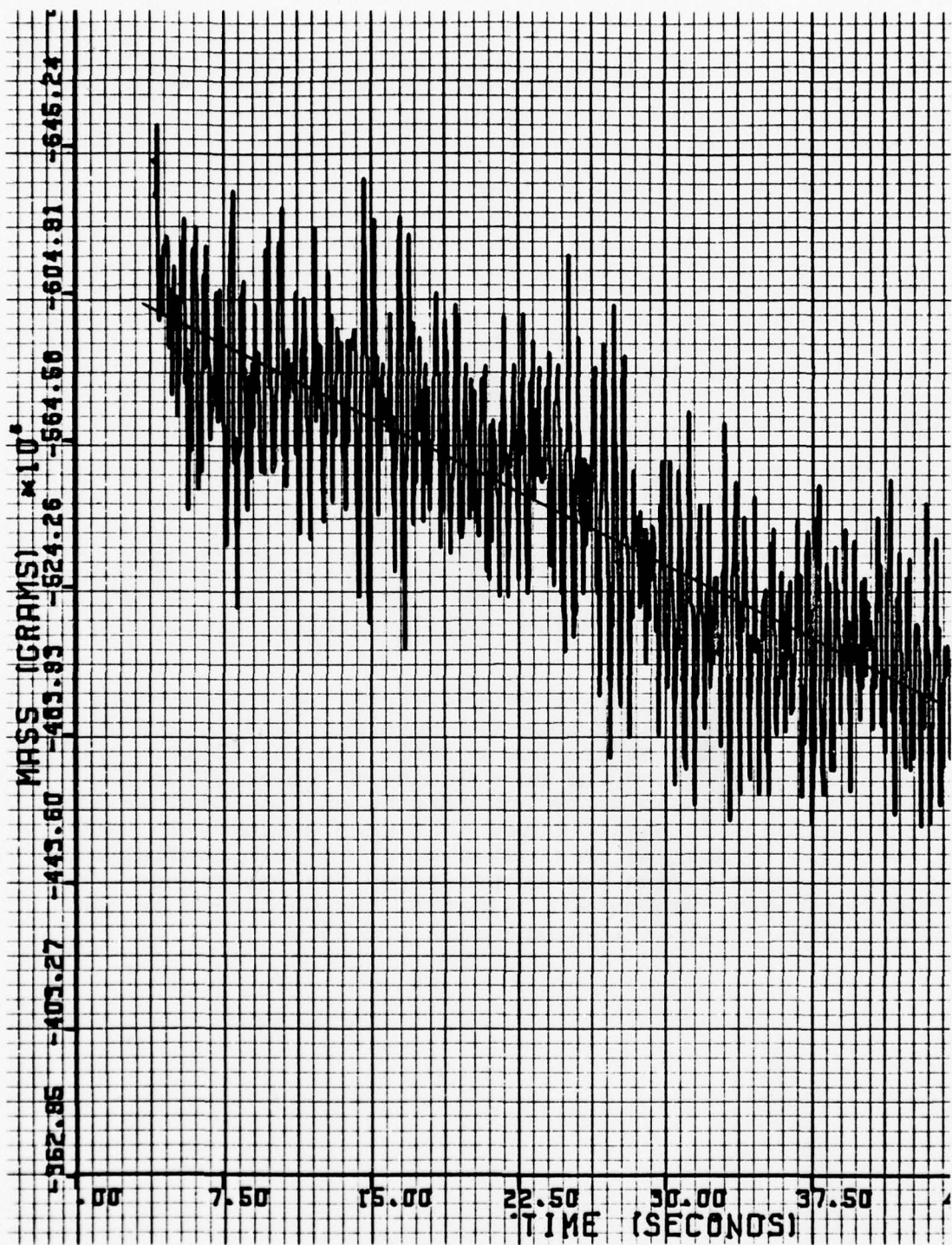


FIGURE 20. WEIGHT VARIATION AS A FUNCTION FOR  
MODIFIED PARTICLE INJECTOR-MOTOR ACTIVATED.

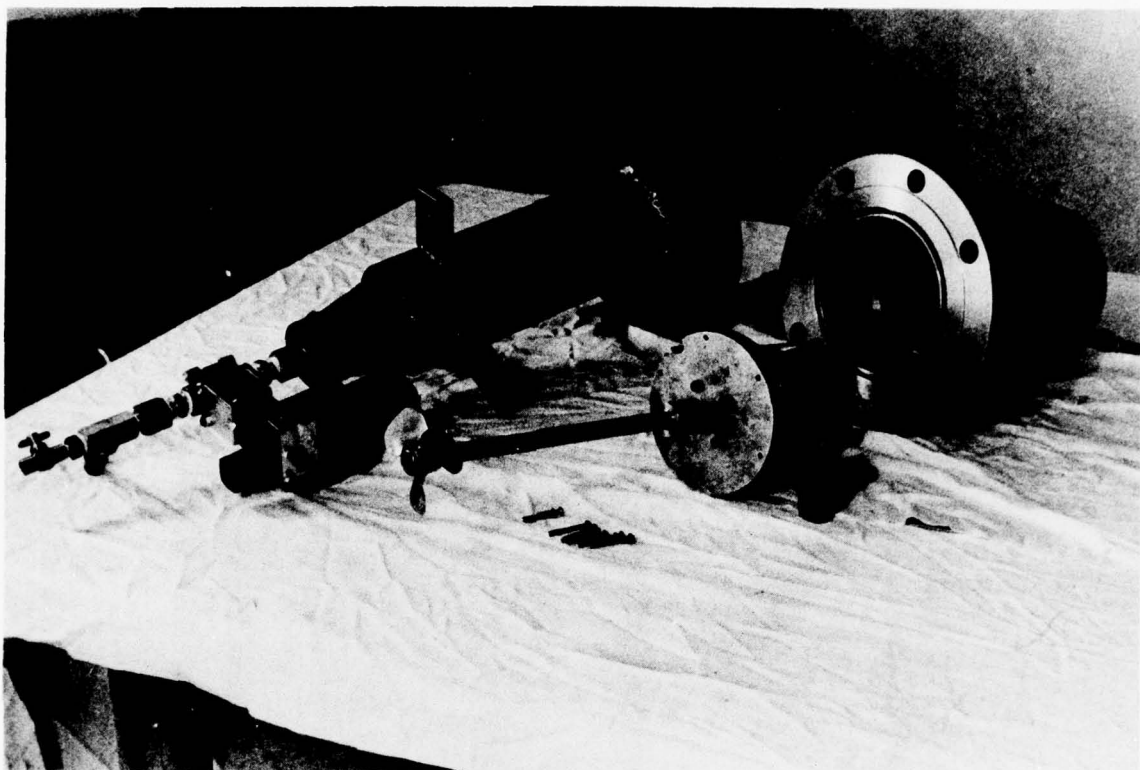


FIGURE 21. COMPONENTS OF MODIFIED PARTICLE INJECTOR.

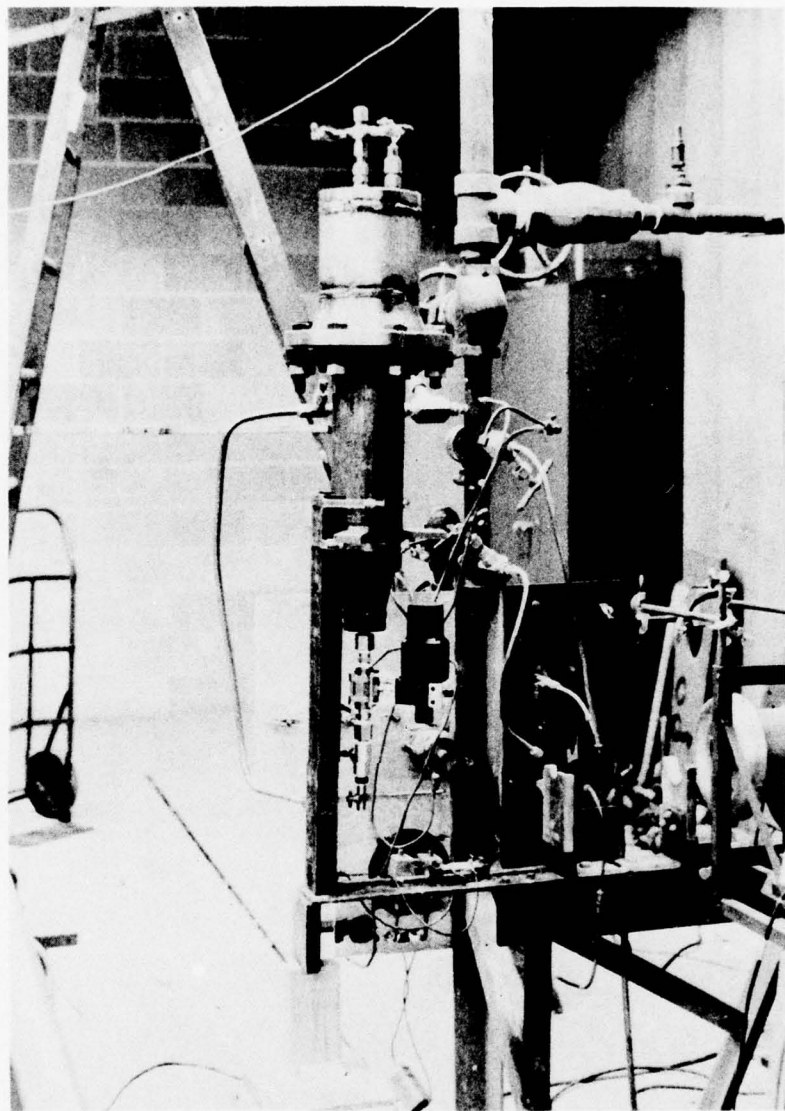


FIGURE 22. MODIFIED PARTICLE INJECTOR INSTALLED ON BENCH TOP FACILITY.

## SECTION IV

### EROSION-ABLATION TEST FACILITY

A combustion-heated wind tunnel system was assembled to provide high temperature, high pressure gases into which solid particles are injected and accelerated to hypersonic speeds. The facility is shown in Figures 23-24 and consists of a hydrogen-air combustor, a low-expansion angle nozzle exhausting to a free-jet test cabin, a diffuser, and a two-stage air ejector pumping system. The mass flow rate of each supply gas is determined by measuring the pressure drop across a calibrated orifice. The facility is located in a test pit and is controlled remotely.

The expansion nozzle has an exit half angle of  $0.50^\circ$ , a throat diameter of 0.10 inch, and a throat-to-exit length of 2.86 feet. It was constructed of nickel using electro-forming techniques. A separate throat section is employed and is connected to the electroformed expansion section with a collar arrangement. A simple water bath is used to cool the expansion section. The nozzle is shown in Figure 25.

The particle injection system is shown in Figures 26-27. Pressurization of the particle container is controlled by a dome loader and a solenoid valve located in the main line. A Whitey Model 133 SR ball valve, which is controlled by air pressure, in the feed tube from the particle container to the tunnel allows remote activation of the feed. In addition, a water flush system is employed to allow the particle injection system to be cleaned after each facility run and to insure there is not build-up of particles in the container or valve configuration. The particle-water slurry system described previously is employed and the particle mass flow rate is determined with the calibrated cantilever beam balance.

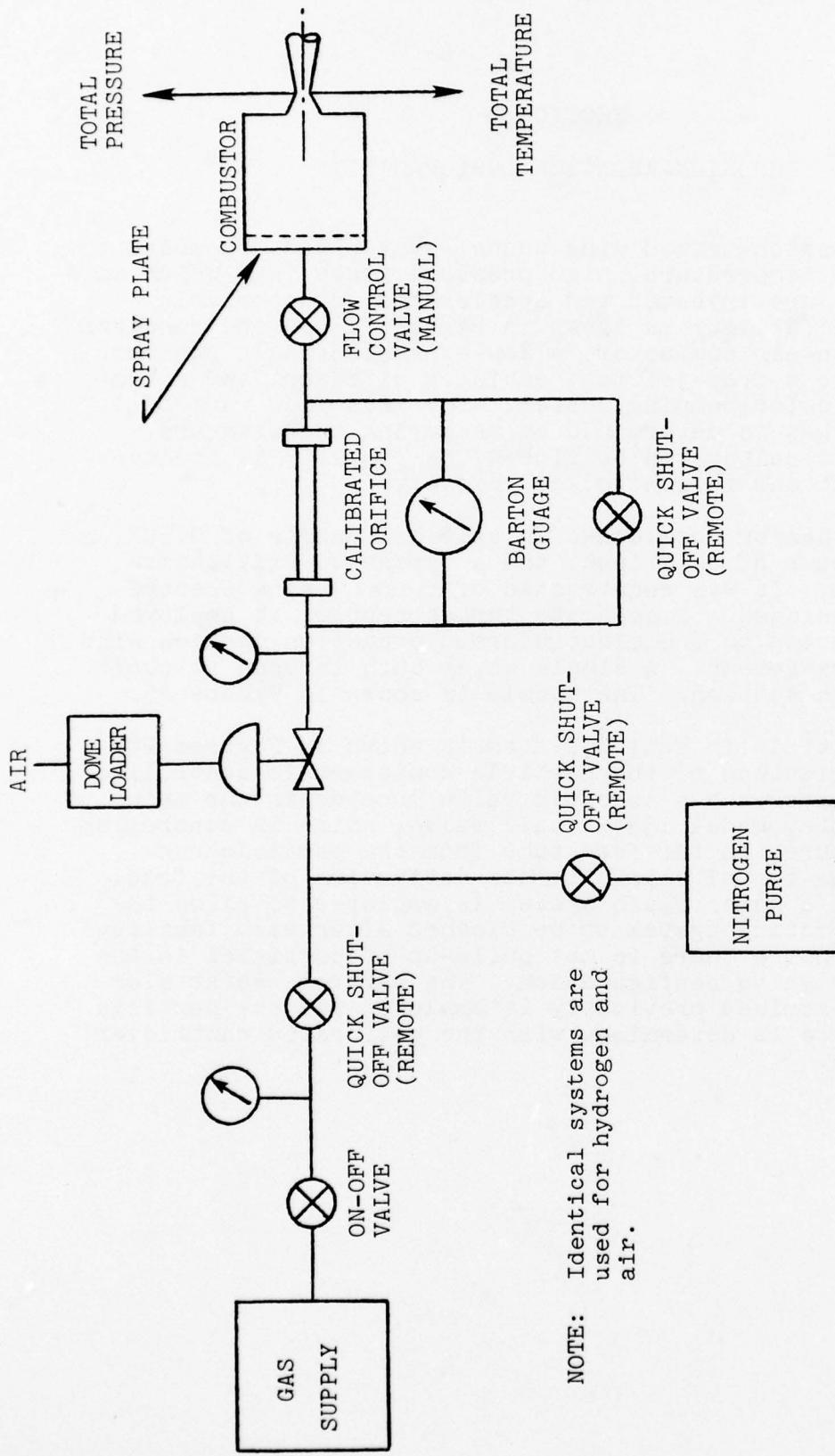


FIGURE 23. SCHEMATIC OF EROSION-ABLATION COMBUSTION FACILITY.

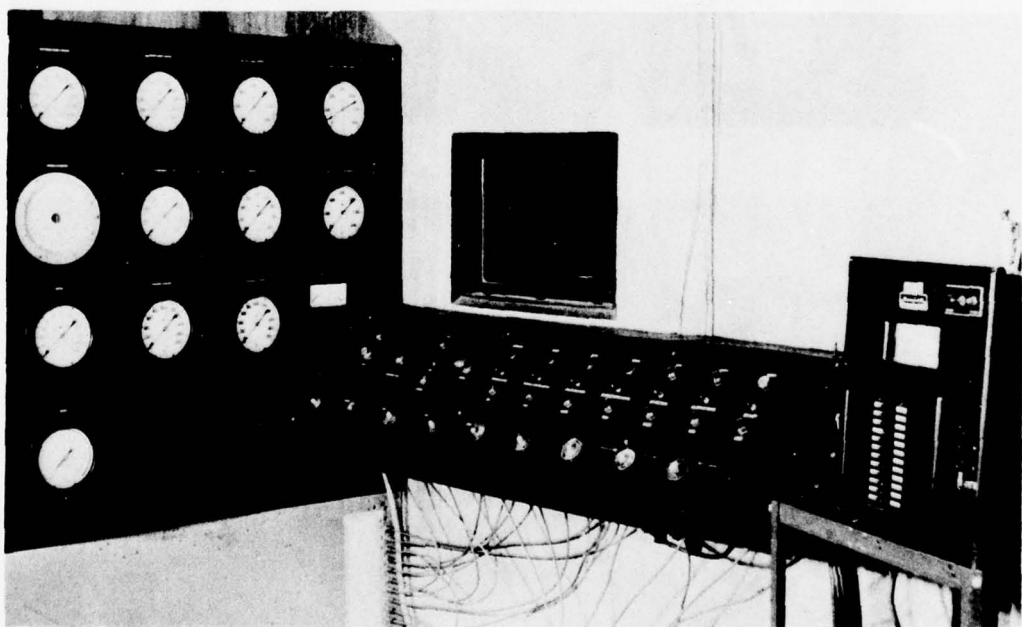
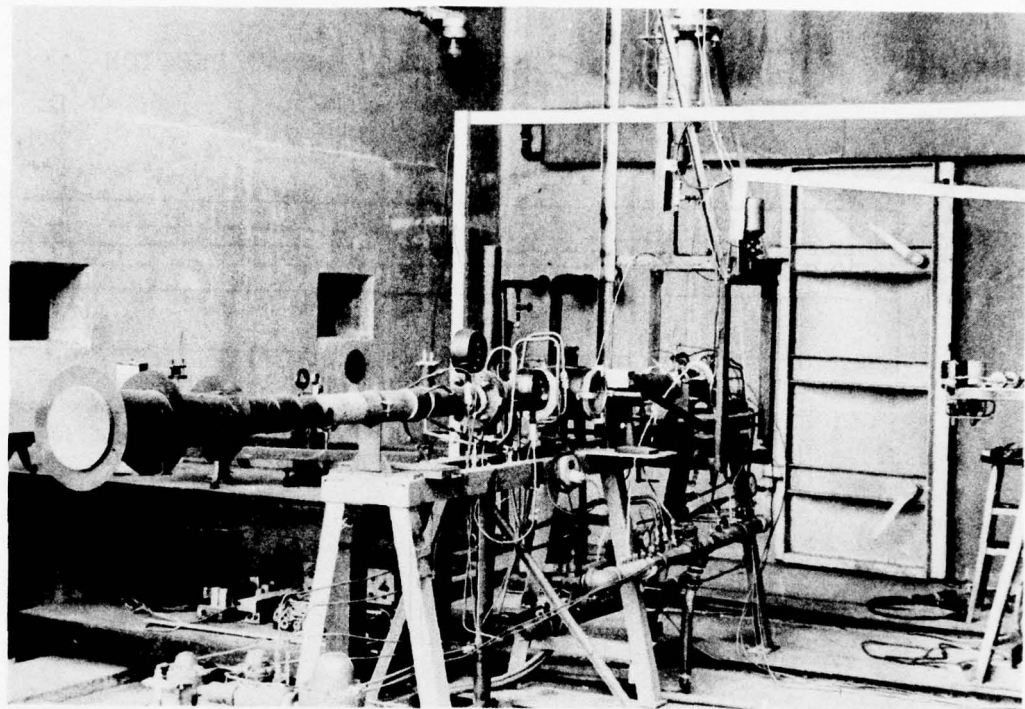


FIGURE 24. EROSION-ABLATION FACILITY AND ASSOCIATED CONTROL PANEL.

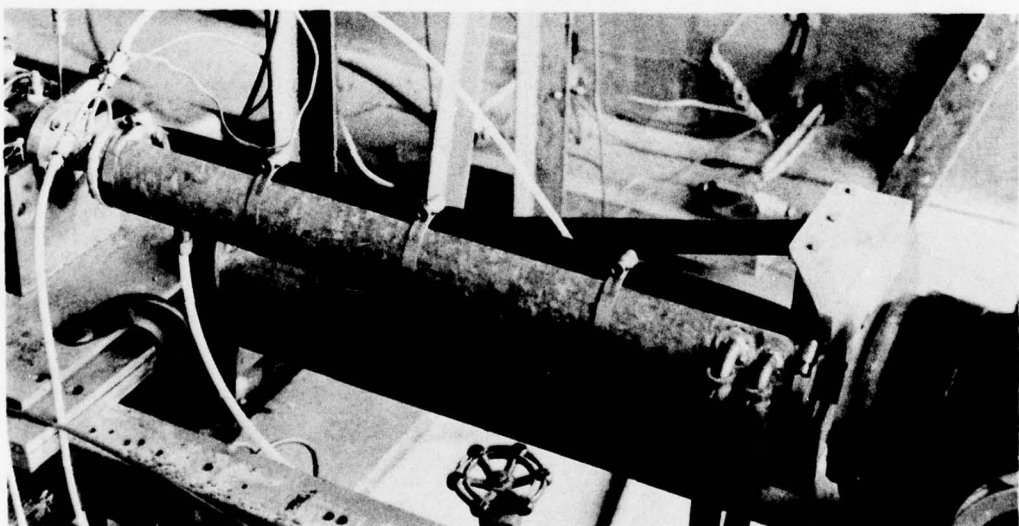
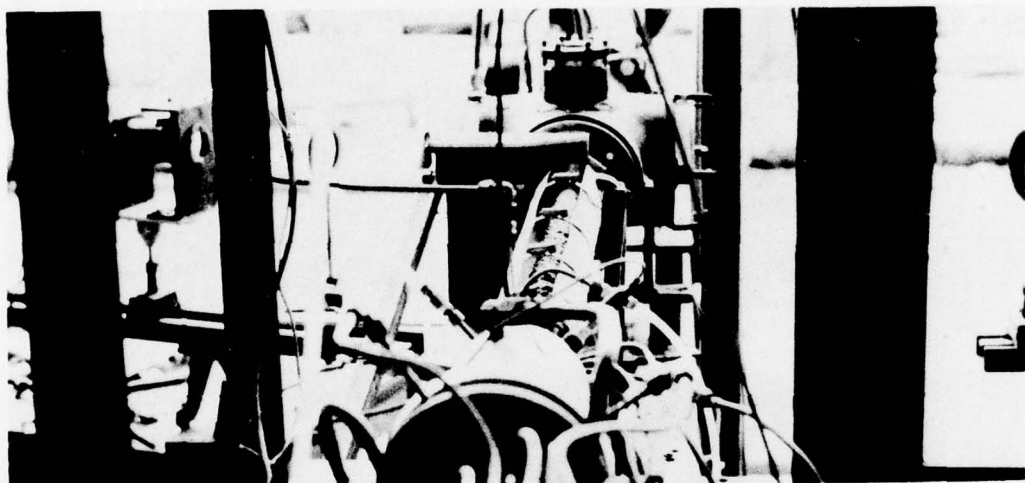
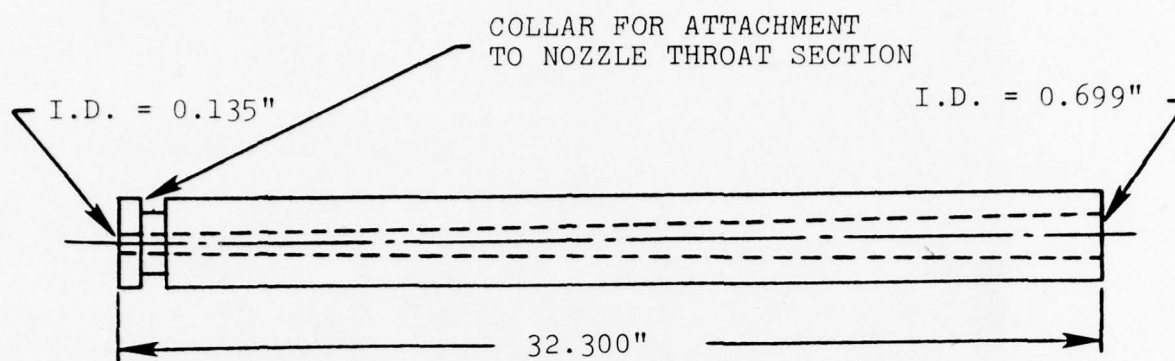


FIGURE 25. ELECTROFORMED DESIGN NOZZLE FOR EROSION-ABLATION COMBUSTION FACILITY.

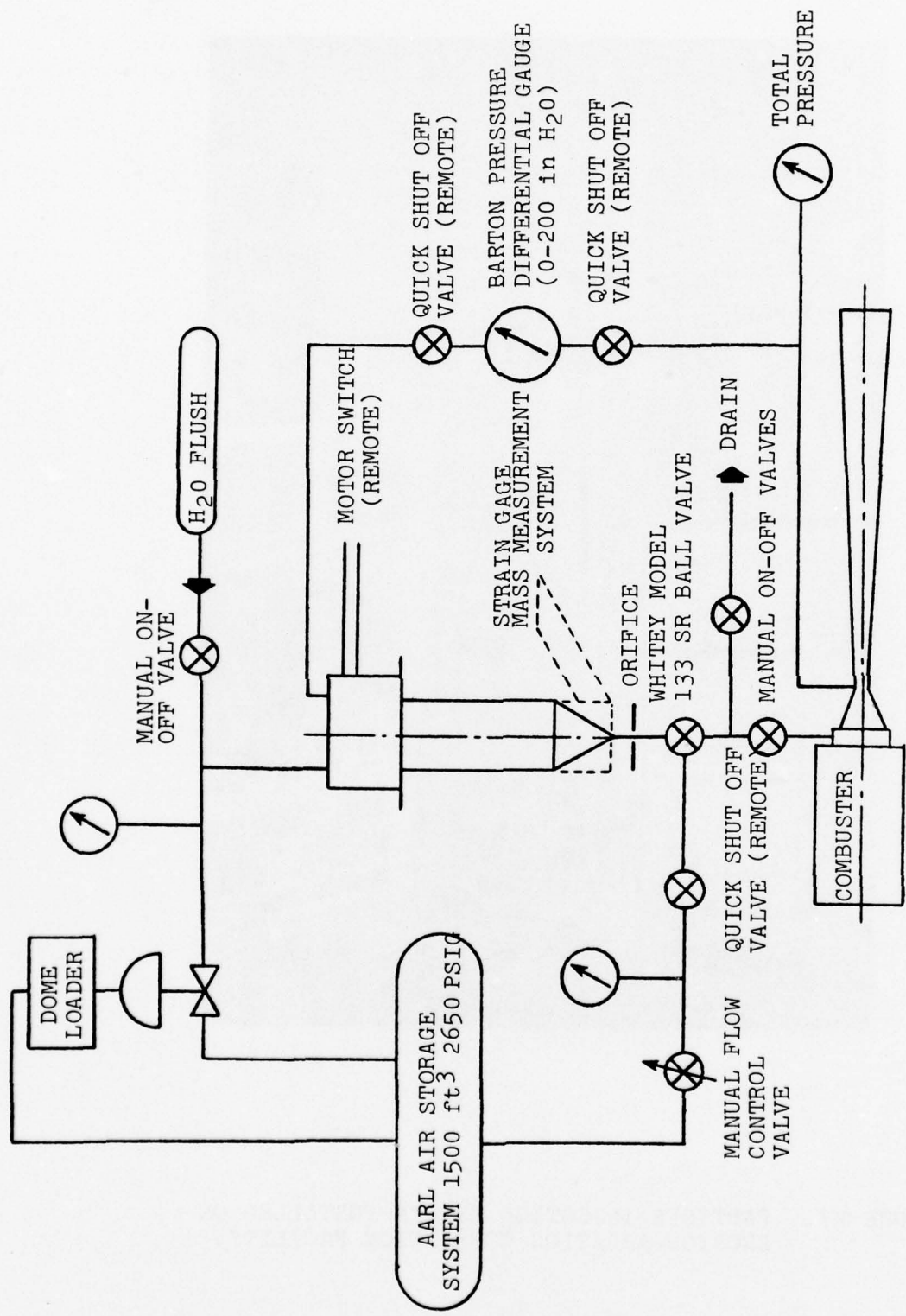


FIGURE 26. SCHEMATIC OF EROSION-ABLATION COMBUSTION FACILITY PARTICLE INJECTION SYSTEM.

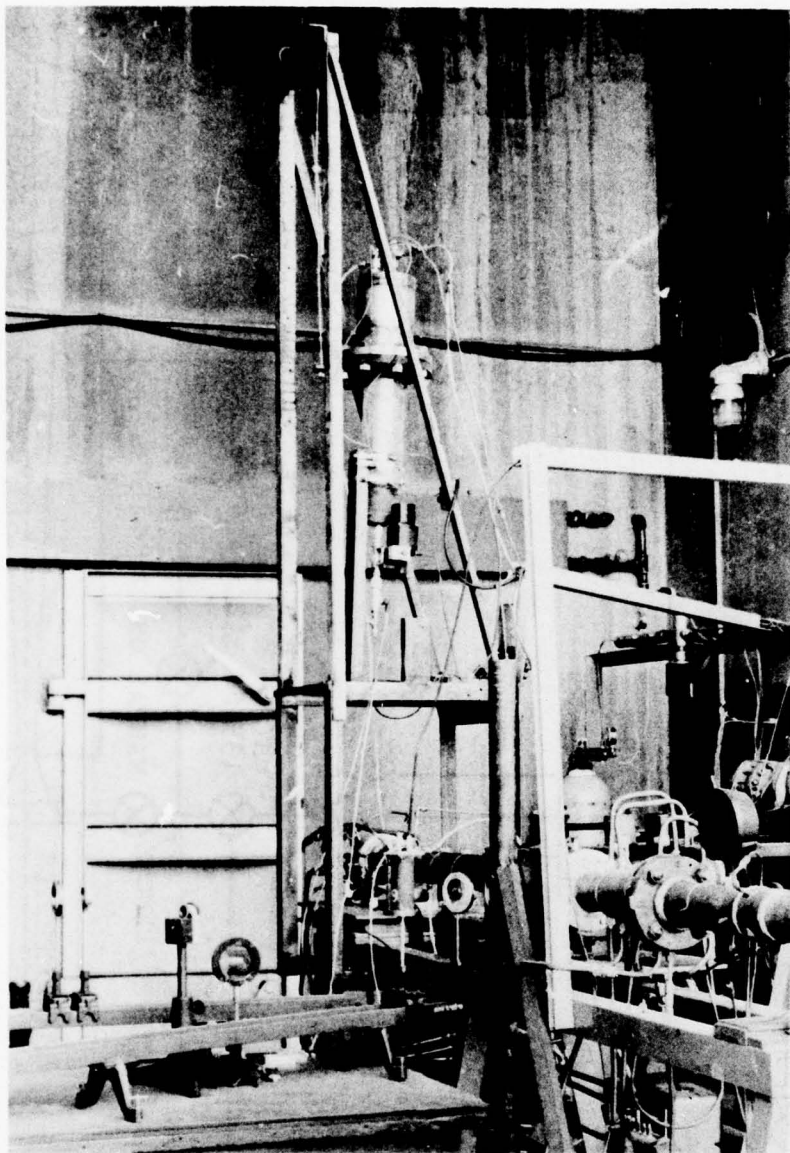


FIGURE 27. PARTICLE INJECTION SYSTEM INSTALLED ON EROSION-ABLATION COMBUSTION FACILITY.

## SECTION V

### LASER DOPPLER VELOCIMETER

The main components in the Laser Doppler Velocimeter (LDV) System used in this study can be placed into two categories: (1) the laser and optical system, and (2) the signal processor. Although many LDV optical arrangements have been used in previous studies, the object of the present approach is to provide an optical system where the total angle between the two beams (hence, the fringe spacing) can be easily changed. Signal processing techniques are areas of current research. These include spectrum analyzers (13), F-M de-modulators (14), and frequency trackers (15). Frequency counters (16) are also used and employ direct measurement of the signals resulting from single particles passing through the fringe volume. The resulting signal analysis is termed burst processing or monitoring of the discontinuous LDV signal. The signal processor used in the present study utilizes burst processing and is derived from a basic design developed by Zammit (17, 18).

A number of factors must be considered before a burst processor LDV system can be applied to a high-speed flow field. These include calibration procedures, filter selection, and the computer related interface and software. These topics are discussed in detail.

#### A. LASER

For the present study, a five watt argon-ion laser operating on the  $4880\text{\AA}$  line was used. The laser was placed in a room adjacent to the erosion-ablation facility with the beam passing through a port into the transmitting optics. The point under examination in the flow field was on the nozzle centerline a small distance downstream of the nozzle exit plane.

#### B. OPTICAL ARRANGEMENT

The LDV optical system is shown in Figures 28 and 29. The laser beam passes through a splitter which results in two beams of approximately equal intensity which are focused by a lens with a positive focal length of 11.5 inches. Another lens with a negative focal length is placed before the focal point of the positive lens. The relative position between the positive and negative lens determines the total

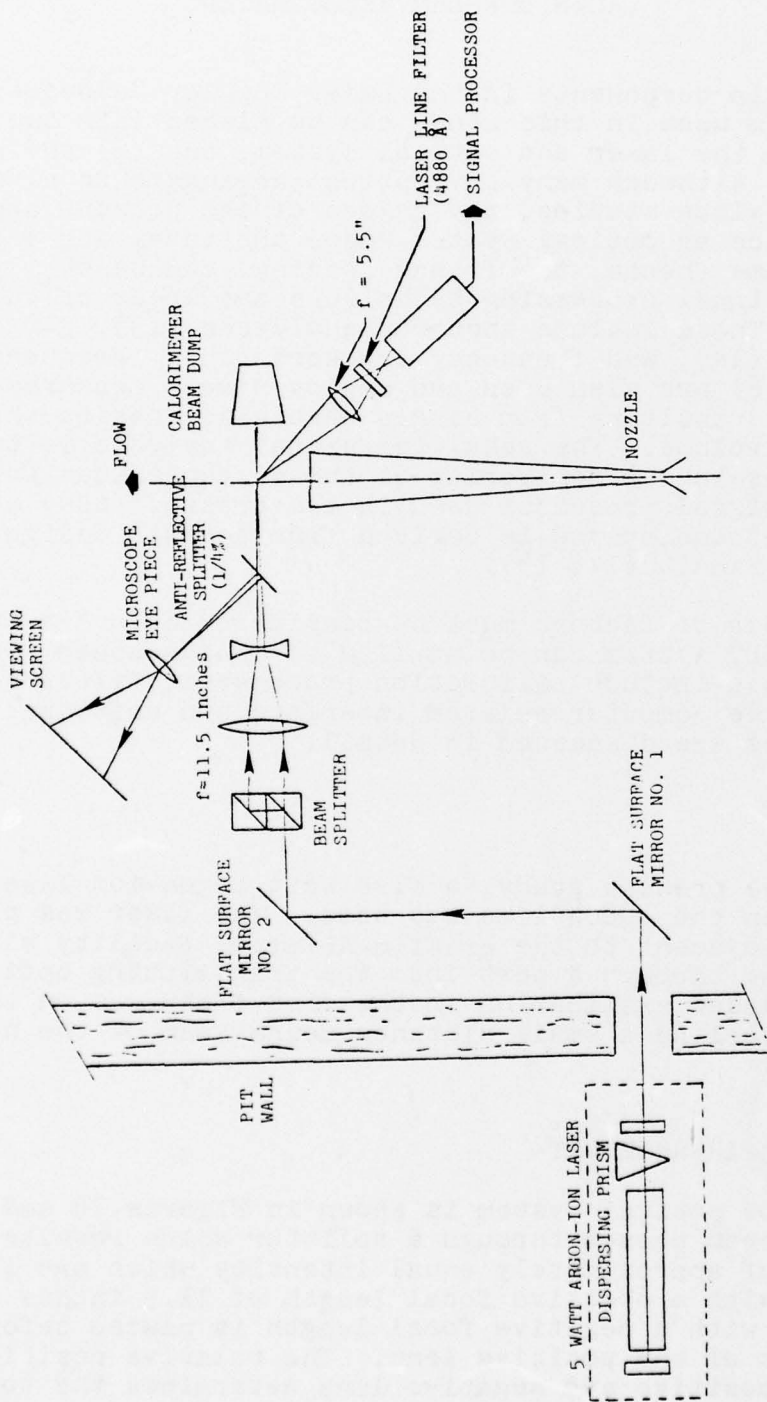


FIGURE 28. OPTICAL SCHEMATIC FOR LASER DOPPLER VELOCIMETER.

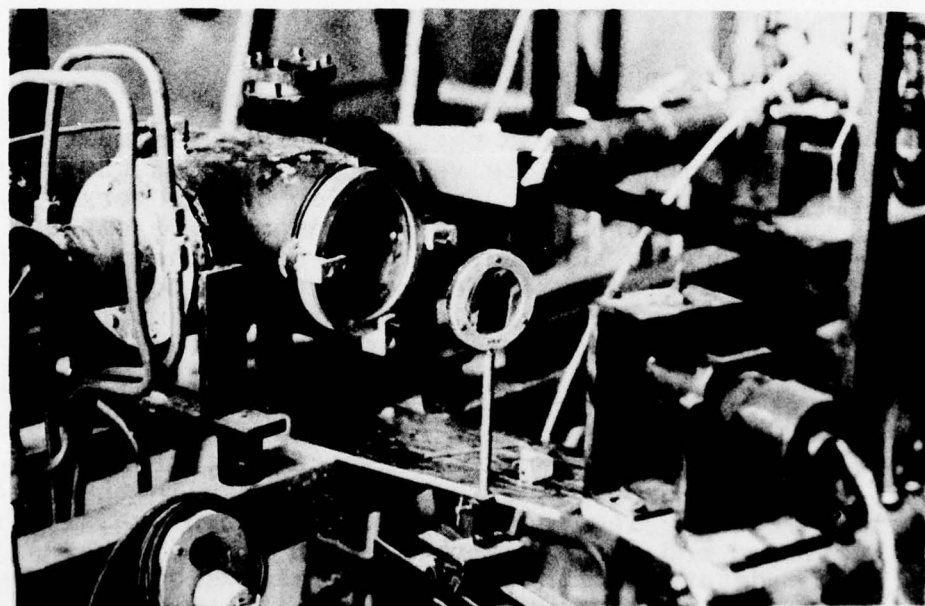
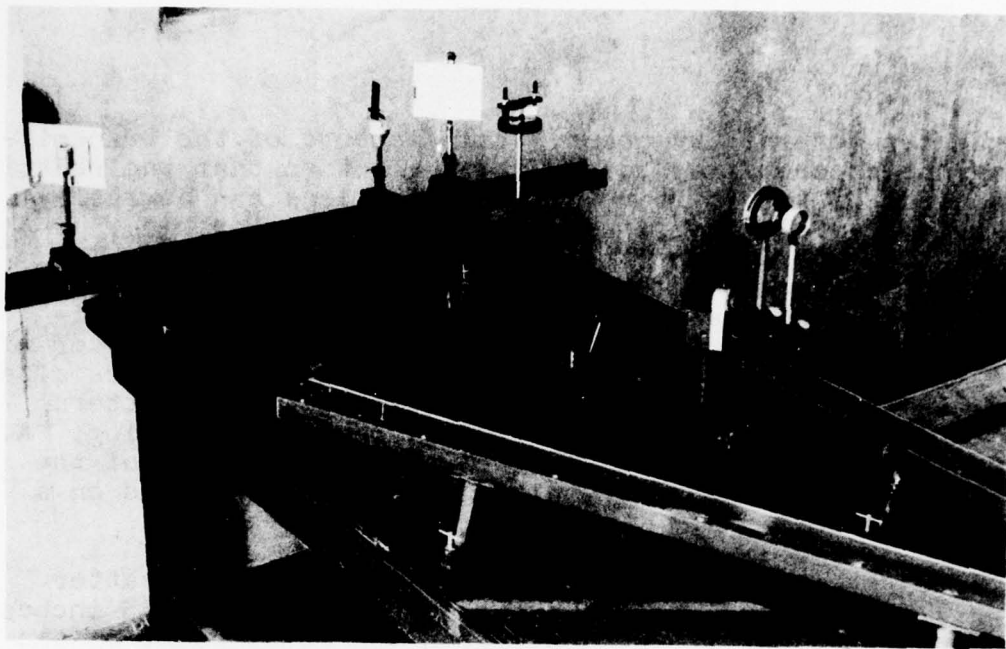


FIGURE 29. OPTICAL ARRANGEMENT FOR THE LASER DOPPLER VELOCIMETER.

angle between the two beams. All elements of the transmitting optics are fixed to optical benches so that the relative positions of the positive and negative lens can be easily changed to yield the required total beam angle.

The two beams, after passing the focal point in the flow field, enter a calirometer beam dump which is monitored during operation of the facility. A beam splitter with 0.25% reflectance is placed in the transmitting optics after the negative lens to form an image of the fringe pattern which can be monitored to determine the fringe spacing. A microscope eyepiece is placed near the focal point of the reflected beams and the resulting image is displayed on a viewing screen.

The receiving optics are placed in a forward scatter mode. The collection lens has a focal length of 5.5 inches and is approximately 12 inches from the focal point of the two beams in the flow field. The collected light is passed through a narrow band pass filter set on the  $4880\text{\AA}$  line and is focused on the cathode of an EMI 62565 photomultiplier tube (PMT).

#### C. AARL SIGNAL PROCESSOR

The signal processor for the present studies must be capable of measuring particle velocities up to 5,000 feet/sec. Therefore, the doppler frequencies become very large (90 MHz) and pulse stretching techniques must be employed to achieve reasonable accuracy. Also, since the particle size varies, the velocity difference between successive particles may be large, dictating the requirement for a large dynamic range in the measuring system.

The doppler signal from the photomultiplier tube is preamplified and passes through a high pass and low pass filter network. The filtering is necessary to remove the bias voltage caused by the Gaussian intensity in the laser beam and the square law photo detection. Zero crossing timing is utilized and measurement of eight doppler cycles results in the determination of the particle velocity. The unique feature of this signal processor is that time to voltage conversion is accomplished by Time to Amplitude Height Converters (TAC) rather than by digital clock. The TAC measures the time interval between pulses to its start and stop inputs and generates an analog output voltage proportional to the measured time and inversely proportional to velocity. The TAC's are free of the inherent limitation of clock-based units which have a minimum resolution equal to the clock frequency.

A functional diagram of the AARL Signal Processor is shown in Figure 30. The input to the processor is preamplified, filtered, and postamplified where the post amplifier output goes to two comparators producing a square wave at the doppler frequency. Two counters are used to generate rectangular pulses equal in time to four and eight doppler periods, respectively. The ramp voltage from each of the TAC's, whose output is proportional to its doppler count (4 or 8), is differentiated to give a negative spike which is used for the start-stop inputs.

The ramp output voltage from the eight period TAC is read into the high speed Sample & Hold No. 1. For a valid data point, the output voltage from the four period TAC should be half the output of the eight period TAC. An error check circuit is used to compare these outputs and only valid signals are processed. Sample & Hold No. 2 stores the valid output, and an interrupt is sent to the AARL computer to indicate that data is available for processing. The AARL computer activates a high-speed analog to digital converter to digitize Sample & Hold No. 2's output.

A discriminator compares the incoming signal to a fixed bias level, thereby insuring that only preselected burst signal levels are processed, and enables the comparator gate to start the zero crossing timing when the threshold level is satisfied. The TAC's are designed to produce a constant voltage when signaled to stop, and a strobe pulse is generated to gate the TAC outputs, disable the discriminator, and reset the counters.

The AARL signal processor is mounted on two printed circuit boards. All integrated circuits and the majority of the discrete components are mounted on Board No. 1 which is shown in Figure 31. It consists of an August ECL/TTL multi-layer printed circuit board. The error amplifier and the Sample & Holds No. 1 and 2 are mounted on printed circuit Board No. 2 as shown in Figure 32. Both printed circuit boards are housed in a Nuclear Instrumentation Module (NIM), which is installed in an Ortec Modular System bin with common power supplies (NIMBIN) as shown in Figure 33.

A detailed block diagram of the signal processor\* is given in Figure 34. The output from the first comparator is a square wave

\*Appendix A contains the pertinent AARL Signal Processor wiring diagrams.

Appendix B gives the parts list for the processor.

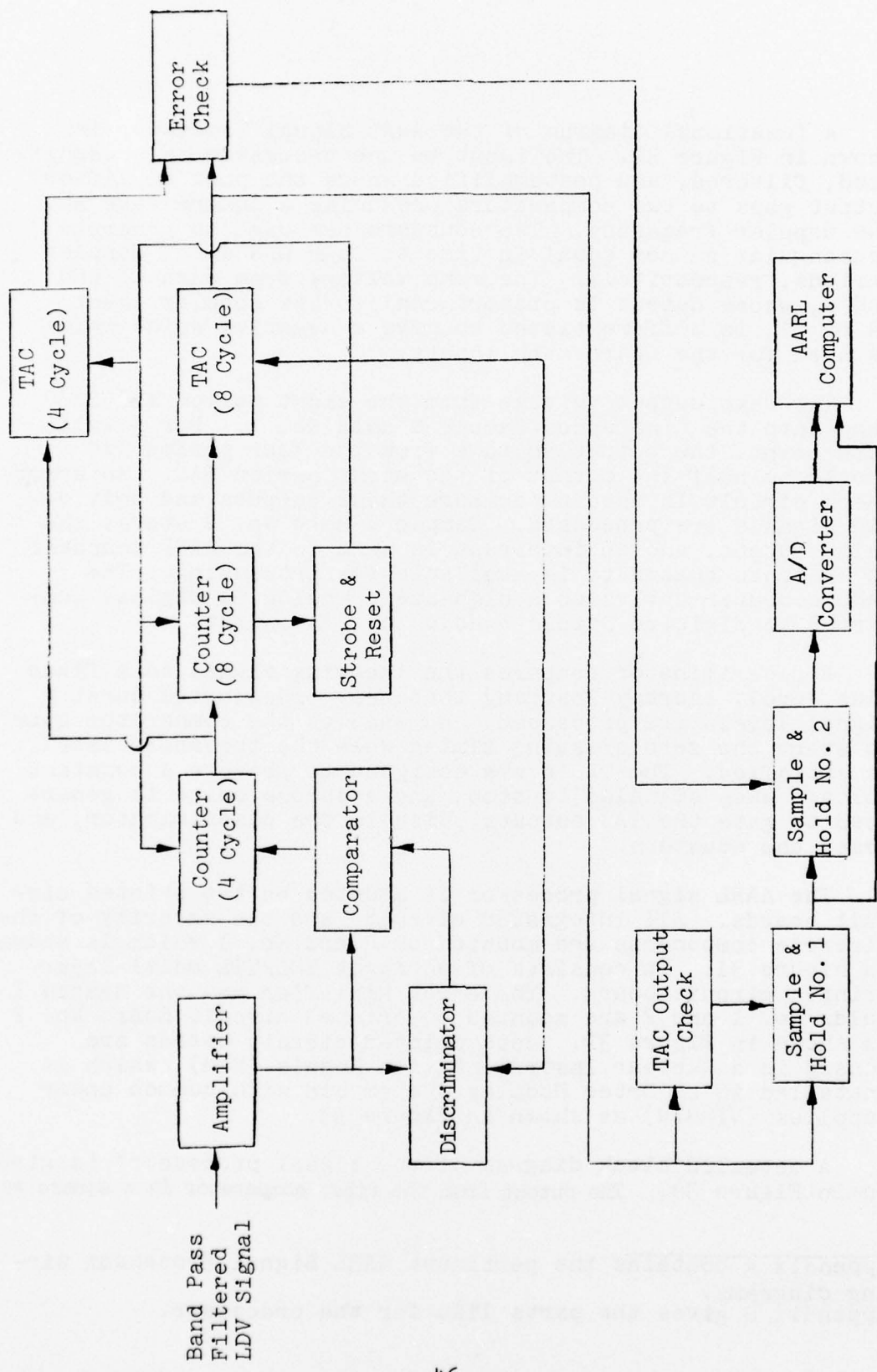


FIGURE 30. SIGNAL PROCESSOR FUNCTIONAL BLOCK DIAGRAM

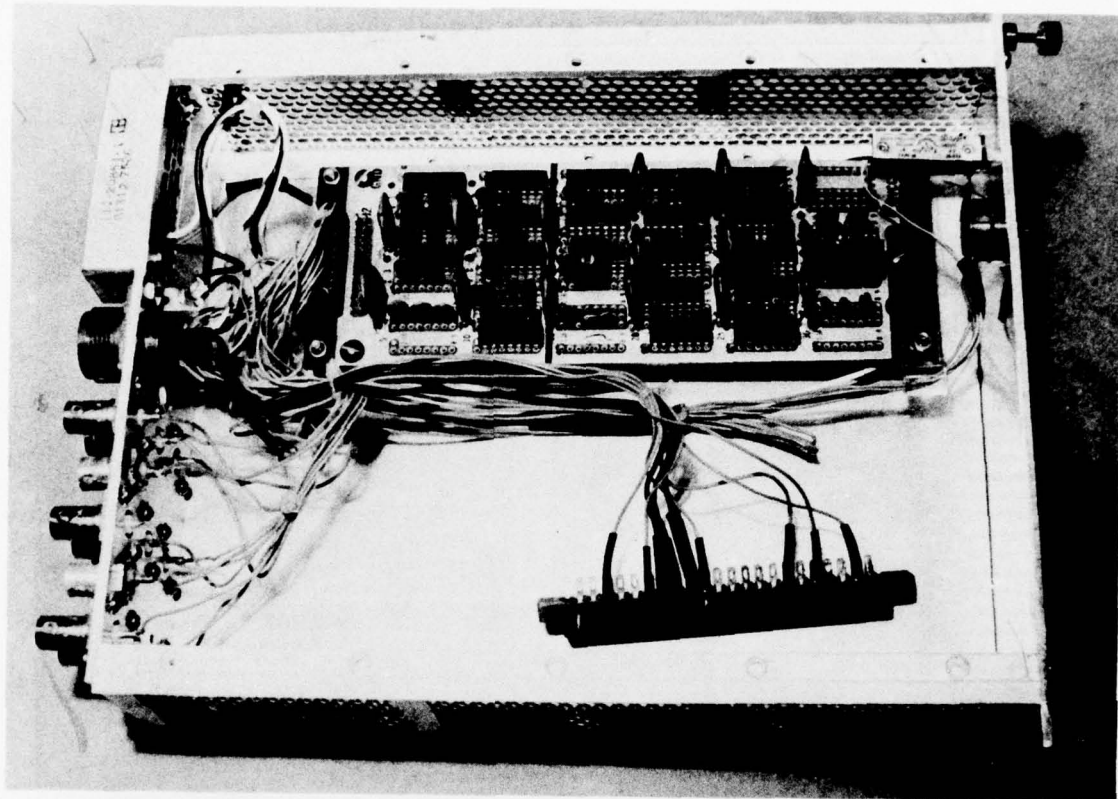


FIGURE 31. SIGNAL PROCESSOR PRINTED CIRCUIT BOARD NO. 1.

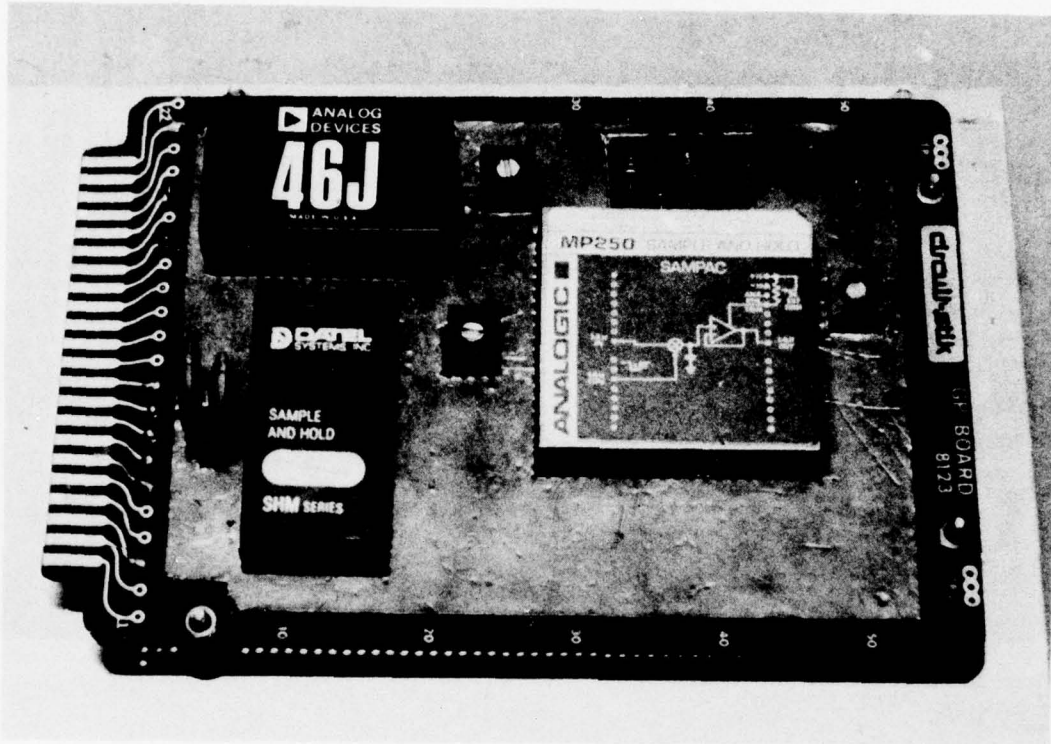


FIGURE 32. SIGNAL PROCESSOR PRINTED CIRCUIT BOARD NO. 2.

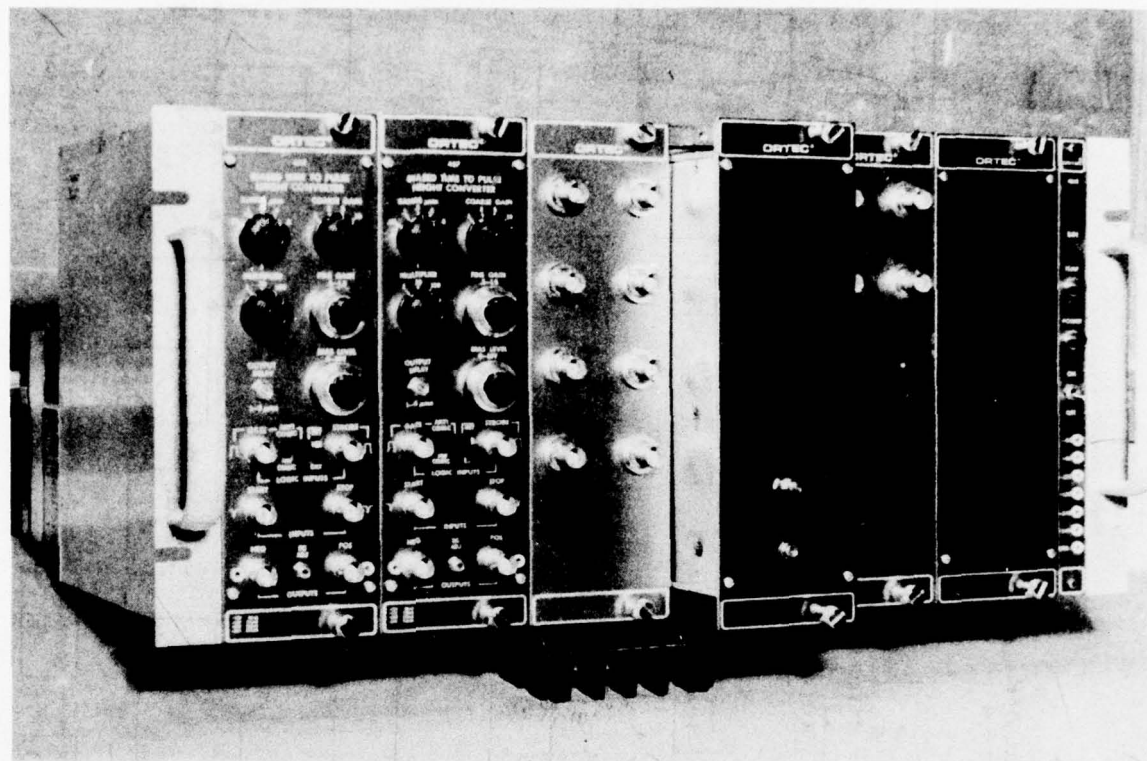


FIGURE 33. ASSEMBLED SIGNAL PROCESSOR IN NIMBIN

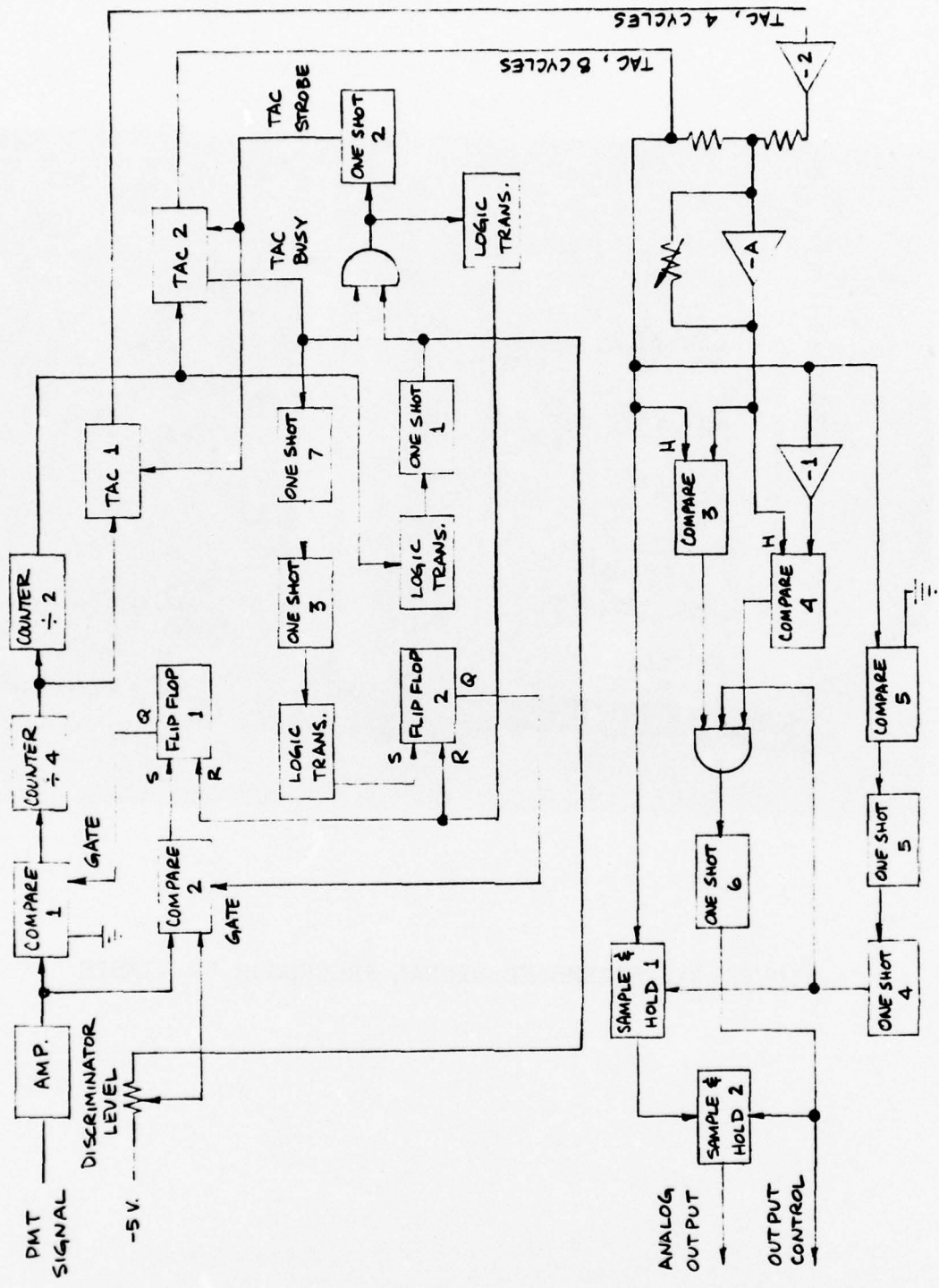


FIGURE 34. BLOCK DIAGRAM OF SIGNAL PROCESSOR

at the doppler frequency. The doppler square wave is then fed to two MECL II binary counters consisting of four Type D flip flops that can be triggered at frequencies in excess of 170 MHz. Both binary counters are reset at the end of each doppler burst. The first doppler period is ignored, which insures that the signal processor uses the higher amplitude doppler signals near the center of the burst. The four and eight counters start counting at the second doppler period with the four counter ending at a count of five and the eight counter ending at a count of nine. Two Ortec 457 time-to-height converters (TAC) are used to convert the doppler four and eight period counter outputs to a standard analog ramp voltage. The ramp amplitude is directly proportional to the start-stop pulse inputs, and the gain of the TAC's are adjusted so that their output voltages will be equal when the four and eight counters are at a count of four and eight, respectively.

A high-speed discriminator, which monitors the doppler input, controls comparator No. 2. The discrimination level is set with a front panel adjustment. When the incoming doppler signal exceeds the set bias level, comparator No. 2 sets flip flop 1 enabling comparator No. 1 to pass the doppler signal. The gate of comparator No. 2 is closed at the end of the eighth cycle by flip flop 2, and both counters, including flip flop 1, are reset. The signal processor will not re-cycle until the eight cycle TAC has completed counting. The "not busy" signal from the eight cycle TAC opens the gate on comparator No. 2, allowing a new signal to be processed.

A comparison of the TAC's output is necessary; that is, twice the four cycle pulse, plus or minus some percentage error, must be accepted by the signal processor as equal to an eight cycle pulse. To accomplish this, the eight cycle pulse and twice the negative of the four cycle pulse are fed into a resistance divider, with the result passed to an amplifier with a gain of  $-A$  (Figure 35). This error signal is compared to the 8 cycle TAC output pulse to obtain the relative error. With a high TAC output, the error voltage may also be high since the acceptable percentage is constant. The error signal is compared to the 8 cycle TAC pulse with two comparators. One comparator uses the TAC output as a positive pulse, and the other comparator uses a negative TAC pulse.

As an example, assume an acceptable error of  $\pm 2.5\%$  in the first four cycles. If each cycle in time were equal to one volt of TAC output, then eight cycles would be a pulse with an amplitude of eight volts. Therefore, with an acceptable error of  $\pm 2.5\%$ , the first TAC would be allowed to have an output of 4.1 volts. The output of the resistive network would be - 0.2 volts, and the gain of the amplifier ( $-A$ )

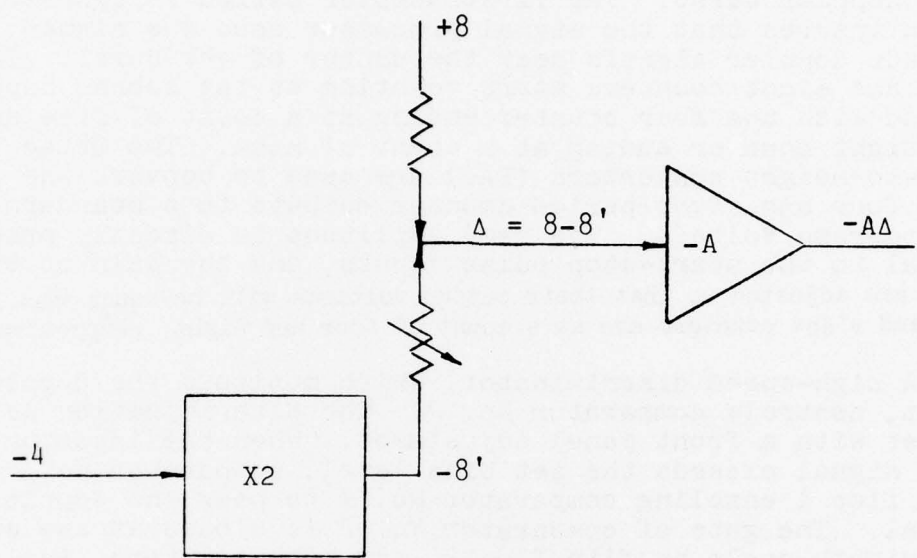


FIGURE 35. SIGNAL PROCESSOR ERROR CIRCUIT

would be set slightly less than -40 so that the output of the amplifier would be +8- volts. The comparators give a true output if the terminal marked "H" (Figure 34) is higher in voltage than the remaining input. With 8 volts at "H" and 8- volts from the output of the amplifier, the No. 3 comparator yields a true output. At comparator No. 4, 8- volts compared to -8 volts will give a true output and the signal will be conditionally accepted. If the first four cycles have an error of -2.5%, the first TAC will have an output of 3.9 volts. The input to the amplifier will be +0.2 volts, the output -8+ volts, and once again the comparators will give true outputs for conditional acceptance. Note that if the four cycles were greater than 4.1 or less than 3.9 volts, the comparators would not have allowed an output by not switching on the triple AND gate at their output. Also note that by adjusting the gain of the error amplifier, not only is the error in acceptable pulse changed, but the data rate is changed by rejecting a smaller or larger number of doppler bursts.

Acceptance of the signal is delayed to allow the error circuit and associated comparators to settle. Comparator No. 5 is triggered by the 8 cycle TAC pulse, which fires one shot 5 and 4 (Figure 34). After a delay, Sample & Hold No. 1 is signalled to sample the TAC output. One shot 4 also signals the triple input AND gate. After the delay, if the AND gate has the required output from the two error comparators, the AND gate triggers Sample & Hold No. 2 via one shots 6 and 7 to sample the signal from Sample & Hold No. 1. Sample & Hold No. 2 has a relatively long hold time allowing the output to be read without voltage changes. One shot 7, which triggers the final Sample & Hold, also supplies a signal to the computer interrupt logic via a TTL line driver. This signal is used to tell the AARL computer that the signal processor has an analog signal to be digitized. The A/D converter can digitize an analog signal every ten microseconds, after which it is processed and stored on the AARL computer for later use.

The waveforms at various points in the processor are discussed to illustrate the operational features. In this case, 2 MHz and 400 kHz signals from a Wavetek Model 130 signal generator are used to simulate the doppler signals, and several of the basic waveforms may be compared with the diagram of Figure 36. The output of comparator No. 1 is shown in Figure 37 (Figure 36-A), which is the doppler signal after the discriminator bias level is satisfied, while the output of comparator No. 2 is shown in Figure 38. The waveform of the eight cycle counter is shown in Figure 39 (Figure 36-B), and the four cycle counter waveform is given in Figure 40. The differentiated signal, shown in Figure 41

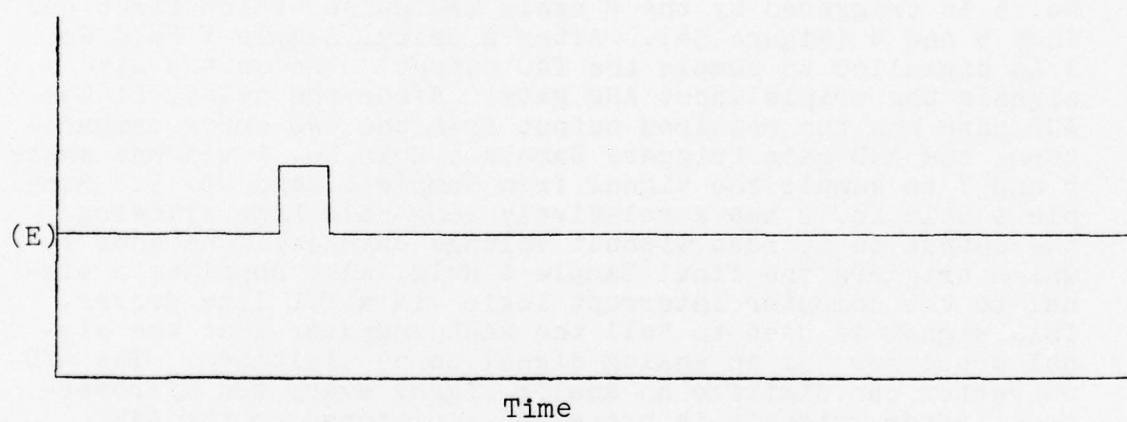
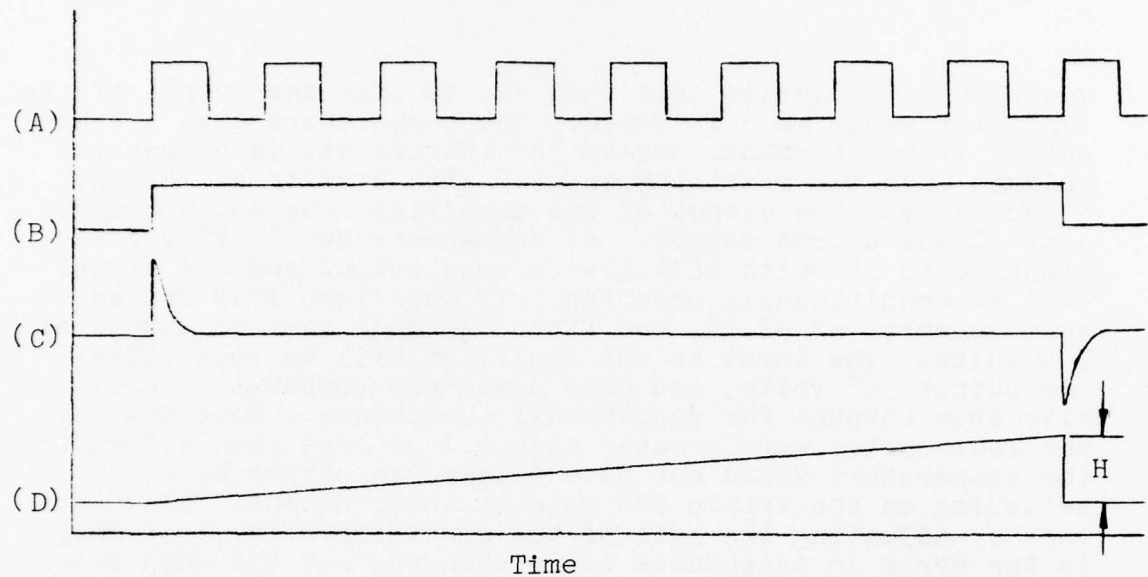


FIGURE 36. SIGNAL PROCESSOR TIMING DIAGRAMS

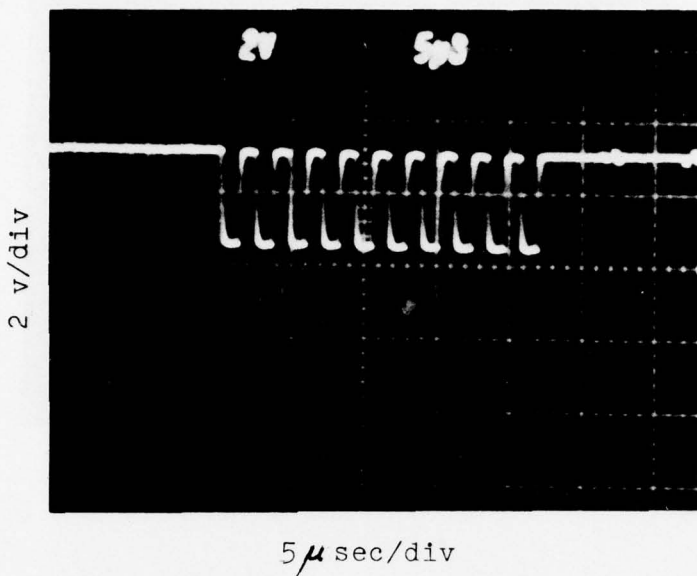


FIGURE 37. OUTPUT OF COMPARATOR 1 (400KHz SIGNAL)

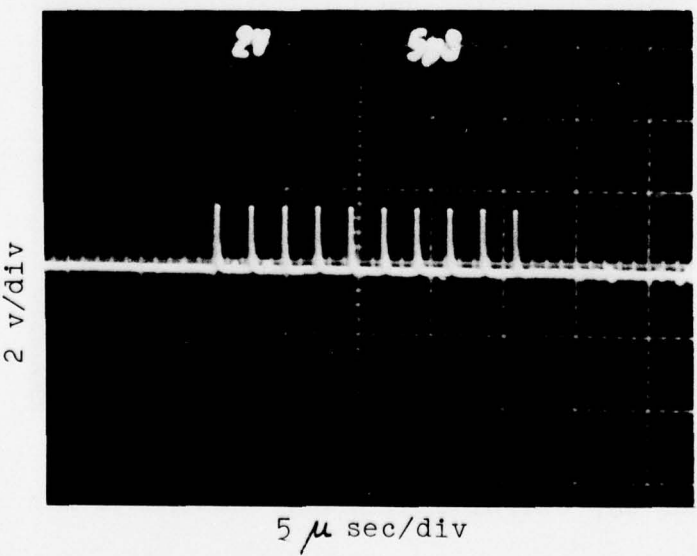


FIGURE 38. OUTPUT OF COMPARATOR 2 (400KHz SIGNAL)

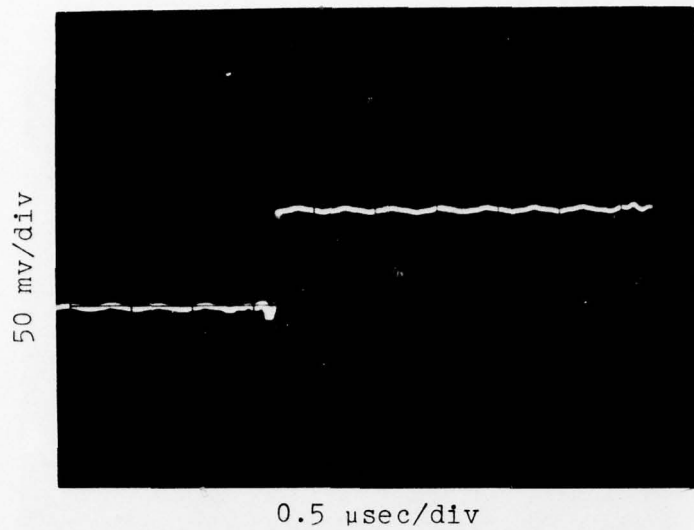


FIGURE 39. OUTPUT OF 8 CYCLE COUNTER (2 mHz SIGNAL)

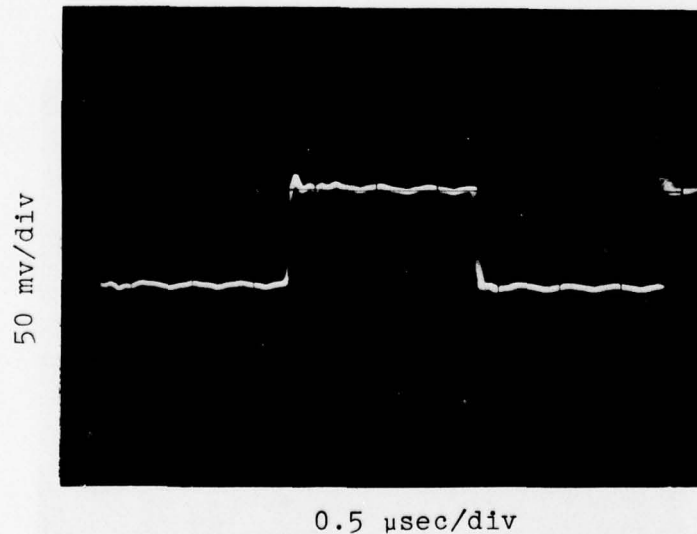


FIGURE 40. OUTPUT OF 4 CYCLE COUNTER (2 mHz SIGNAL)

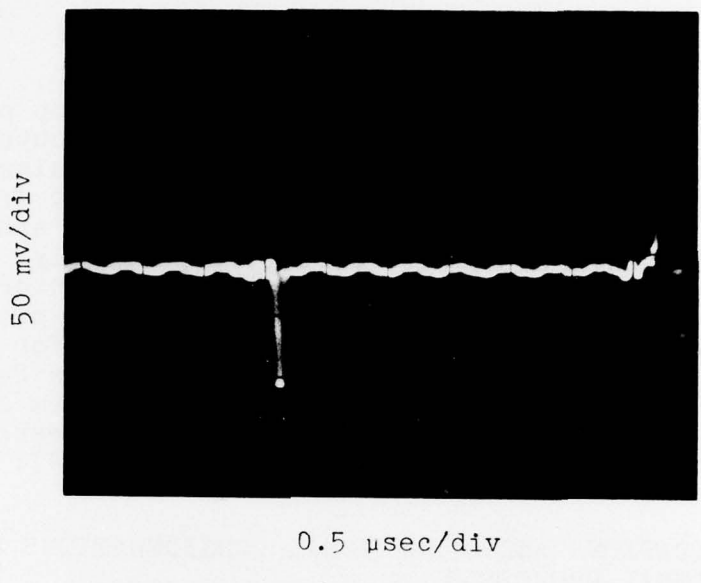


FIGURE 41. DIFFERENTIAL 8 CYCLE PULSE (2 mHz SIGNAL)

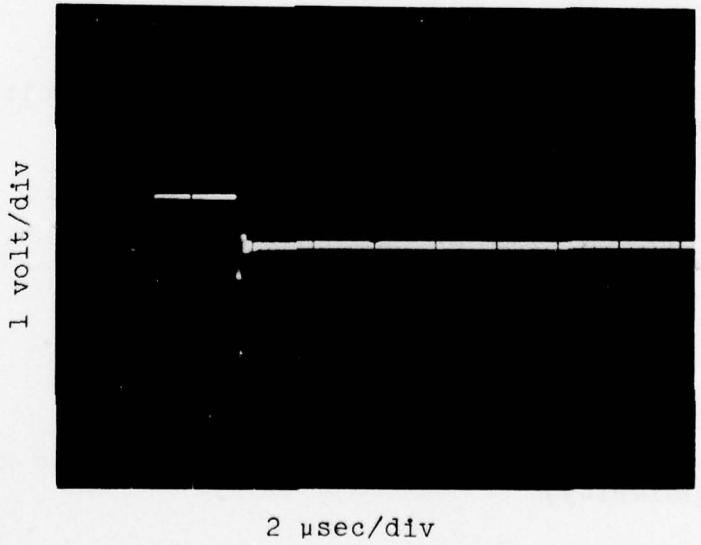


FIGURE 42. TAC OUTPUT PULSE (2 mHz SIGNAL)

(Figure 36-C), is required for the TAC start-stop pulse pair, and is equal to eight doppler cycles. The TAC output is directly proportional in time to the start-stop pulse pair and is given in Figure 42 (Figure 36-D). The output from comparator No. 3 and 4 is shown in Figures 43-44, and are the +8 cycle error and minus 8 cycle error, respectively. The output from the error amplifier is shown in the bottom waveform of Figure 45, where the top waveform is the LDV processor output at 400 kHz (Figure 36-E). The waveform for Sample & Hold No. 1 strobe is given in Figure 46, whereas Sample & Hold No. 1 output is shown in the bottom waveform of Figure 47. Sample & Hold No. 2 in effect is the processor output and is indicated in the top waveform of Figure 47.

#### D. SPECIFICATIONS AND OPERATIONAL CONSIDERATIONS OF THE AARL SIGNAL PROCESSOR

##### BASIC TIMING ELEMENTS

ORTEC #457 Time to Amplitude Converters  
Time ranges 50  $\mu$ sec to 80  $\mu$ sec in 15 steps  
External strobe capability  
Busy signal indicating total time of conversion  
Positive and negative outputs (0-10 volts)

##### UPPER FREQUENCY LIMIT

100 MHz

##### DEAD TIME

$\sim$  14  $\mu$ sec Processing time after acquisition of eight cycles

##### MAXIMUM DATA RATE

100,000 Hz @ 90 MHz input frequency

##### OUTPUT VOLTAGE RANGE

0-10 volts (positive)

##### VALID SIGNAL OUTPUT PULSE

5 volts adjustable length (positive or negative polarity)

##### INPUT SIGNAL VOLTAGE LEVEL

200 millivolts with preamplifier; Higher voltages may be used by reducing the gain of the input amplifier.

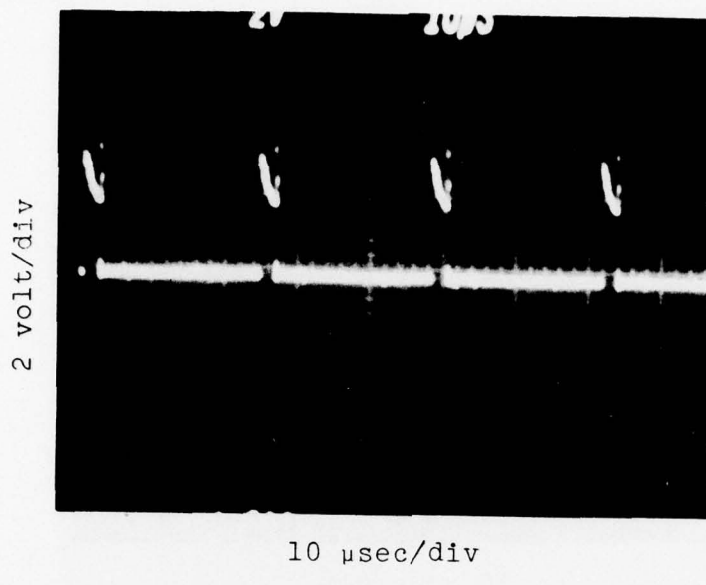


FIGURE 43. +8 ERROR OUTPUT (400 KHz SIGNAL)

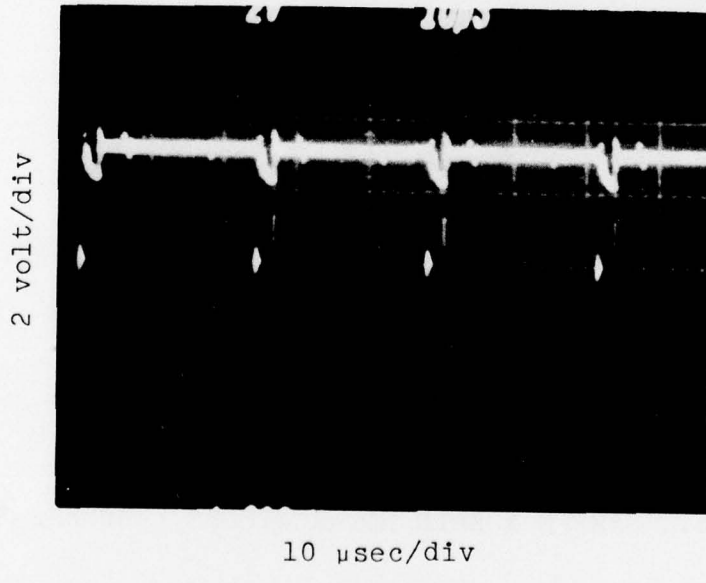


FIGURE 44. -8 ERROR OUTPUT (400 KHz SIGNAL)

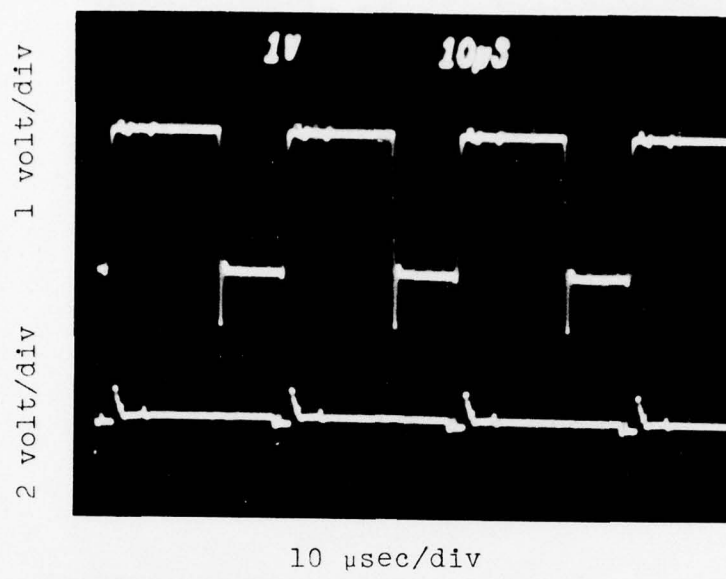


FIGURE 45. TOP WAVEFORM - PROCESSOR OUTPUT  
 BOTTOM WAVEFORM - ERROR OUTPUT AMPLIFIER  
 (400 KHz SIGNAL)

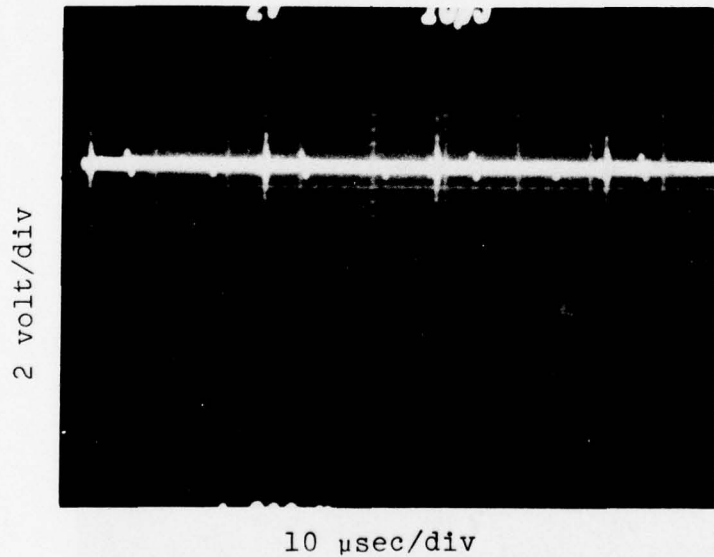


FIGURE 46. SAMPLE & HOLD NO. 1 STROBE (400 KHz SIGNAL)

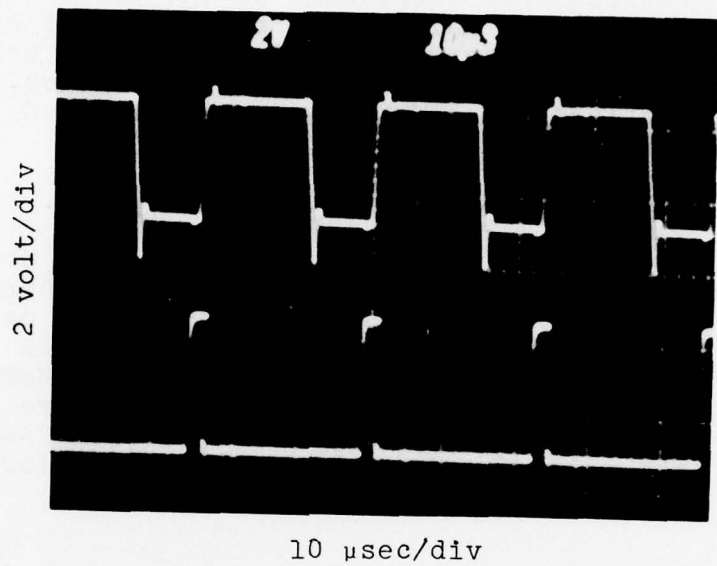


FIGURE 47. TOP WAVEFORM - SAMPLE & HOLD NO. 2  
(PROCESSOR OUTPUT)  
BOTTOM WAVEFORM - SAMPLE & HOLD NO. 1  
OUTPUT (400 KHz SIGNAL).

#### APPROXIMATE PROCESSOR ACCURACY LIMITS

$\pm 2.0\% @ 50 \text{ MHz}$ ;  $\pm 1.0\% @ 10 \text{ MHz}$

The operational considerations of the Laser Doppler Velocimeter System involve calibration of the signal processor, filter selection, and the computer interface and software in the data acquisition and data reduction schemes. These and other operational considerations are discussed.

#### E. CALIBRATION OF THE AARL SIGNAL PROCESSOR

Calibration of all solid state equipment is done before each run, which is turned on for approximately thirty minutes before operation. The signal processor was calibrated at 1, 2, 5, and 10 MHz with a Tektronic Model 180A Time Mark Generator accurate to  $\pm 100 \text{ Hz}$ , and a Tektronic Model 5403 Oscilloscope equipped with a 5B42 time base (Figure 48). The discriminator is set below saturation, and both TAC's are adjusted so the voltage output from the four period TAC is equal to the output of the eight period TAC.

#### F. FILTER SELECTION

To remove the low frequency component or pedestal from the doppler signal and the noise outside of the frequency band of interest, a network consisting of high pass and low pass filters is placed at the input to the signal processor. However, careful consideration should be given to the selection of these filters to provide as wide a band pass as possible since the network will usually limit the signal processor's dynamic range.

The following assumptions (17) are made to arrive at an approximate guide for filter selection:

- (1) Particle size is less than or equal to the fringe spacing;
- (2) The crossing beams have equal Gaussian intensity profiles and the LDV is focused exactly on the probe volume;
- (3) The laser is operating in the  $\text{TEM}_{00}$  mode.

Following the suggestion of Rudd (19), the differential doppler LDV is formed when the two crossing laser beams are viewed as forming a set of fringes due to the constructive

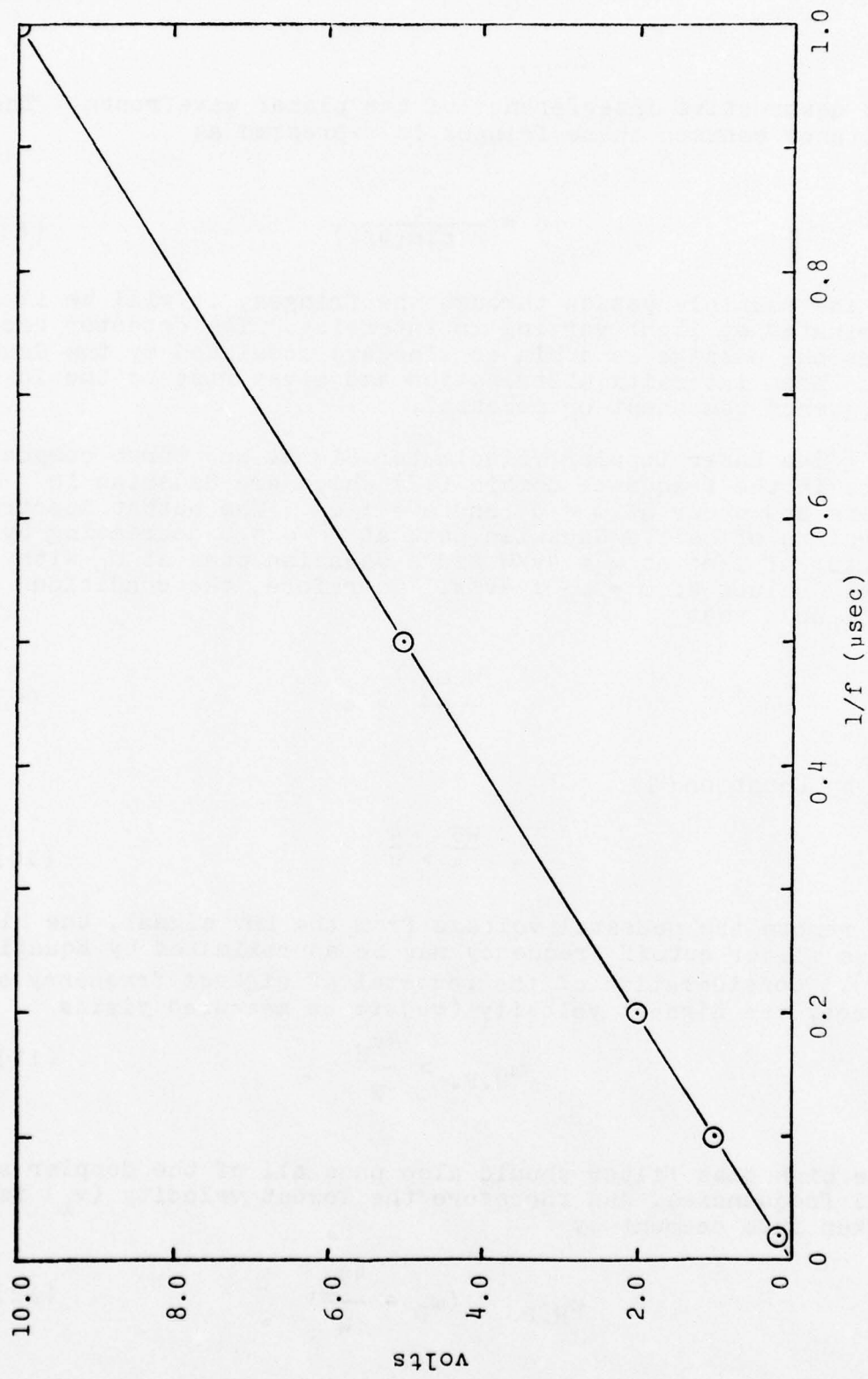


FIGURE 48. CALIBRATION CURVE FOR ARL SIGNAL PROCESSOR

and destructive interference of the planar wavefronts. The distance between these fringes is expressed as

$$d = \frac{\lambda_0}{2 \sin(\theta/2)} \quad (8)$$

As the particle passes through the fringes, it will be illuminated by light varying in intensity. The detector records the passage as a biased sinewave modulated by the Gaussian beam intensity distribution and gives rise to the low frequency component or pedestal.

The Laser Doppler Velocimeter Signal has three components in the frequency domain (17) which are Gaussian in shape and occur at  $\omega = 0$  and  $\omega = \pm \omega_D$ . The output spectrum consists of half a Gaussian peak at  $\omega = 0$  decreasing by a factor of  $1/e^2$  at  $\omega = 4v/W$  and a Gaussian peak at  $\omega_D$  with  $1/e^2$  values at  $\omega = \omega_D \pm 4v/W$ . Therefore, the condition must hold that

$$\frac{W \omega_D}{v} > 8 \quad (9)$$

or by Equation (8)

$$\frac{W \theta}{\lambda} > \frac{4}{\pi} \quad (10)$$

To remove the pedestal voltage from the LDV signal, the high pass filter cutoff frequency may be approximated by Equation (9). Consideration of the pedestal of highest frequency and hence, the highest velocity ( $v_H$ ) to be measured yields

$$\omega_{H.P.} > \frac{4v_H}{W} \quad (11)$$

The high pass filter should also pass all of the doppler signal frequencies, and therefore the lowest velocity ( $v_L$ ) is taken into account by

$$\omega_{H.P.} < (\omega_D - \frac{4v_L}{W}) \quad (12)$$

Therefore for the high pass filter

$$\left(\frac{4v_H}{w}\right) < \omega_{H.P.} < \left(\omega_D - \frac{4v_L}{w}\right) \quad (13)$$

The low pass filter, used to filter out high frequency noise, is chosen by the same approach yielding

$$\omega_{L.P.} > \left(\omega_D + \frac{4v_H}{w}\right) \quad (14)$$

The doppler frequency,  $\omega_D$ , in Equations (13) and (14) may be computed by combining Equations (8) through (10), i.e.,

$$\omega_D = \frac{2\pi v}{d} \quad (15)$$

For the present study, one-half of the laser beam width (W) was taken as 132  $\mu\text{m}$  using the 4880 $\text{\AA}$  line of the Argon-Ion Laser. A fringe spacing, d, was chosen as 100  $\mu\text{m}$ , and therefore dictated that the angle between the two beams be 0.28 degrees. A series of calculations were performed utilizing Equations (13) through (15) to determine the high pass-low pass filter combinations that could be used for the particle velocities of interest.

Particle Velocity (ft/sec)	High-Pass Filter (MHz)	Low-Pass Filter (MHz)
2500	20	70
5000	7	50
10000	3	70

The filter combinations, as purchased from the manufacturer, could only be used in these specific pairs and were not interchangeable. Both the high pass and low pass filter combinations were mounted on a table and installed in the standard 19-inch rack in close vicinity to the signal processor (Figure 49). Selection of each filter combination is made either prior to the facility run or during the data acquisition mode by means of a two-tier rotary switch.

A sharp cutoff was desired in order to obtain good dynamic range and therefore a Tchebycheff (Shape D) type filter was specified in addition to the standard 50  $\Omega$  impedance. There are problems that do occur with sharp cutoff filters,

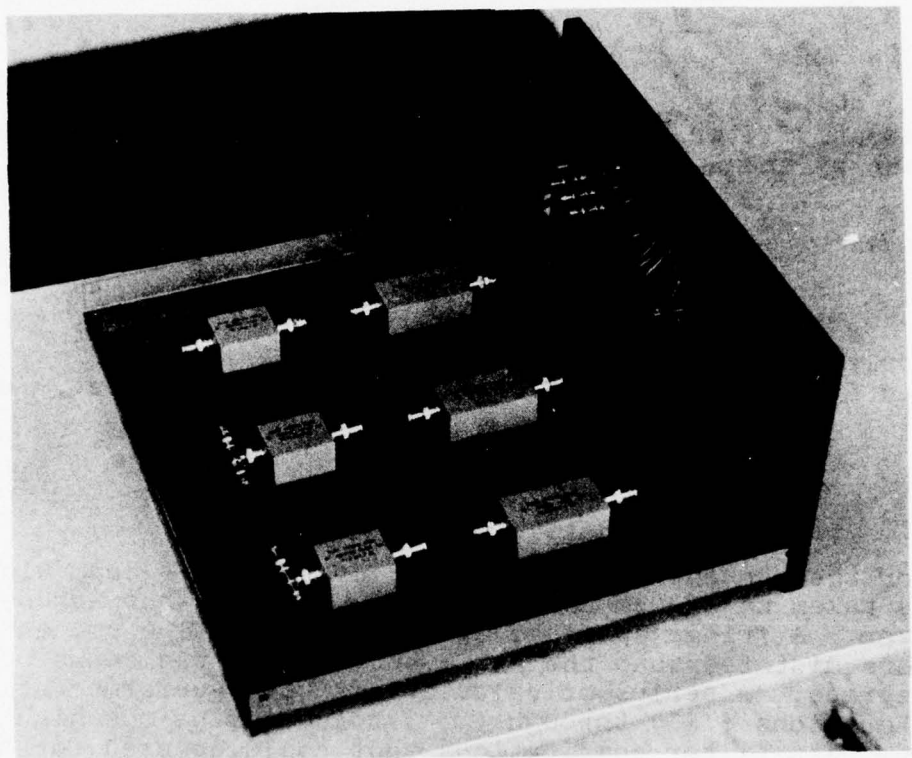


FIGURE 49. SIGNAL PROCESSOR FILTER NETWORK

e.g., the filter may get excited by noise or a discontinuous doppler signal and ring resulting in the doppler signal being superimposed on low frequency ringing.

#### G. AARL COMPUTER INTERFACE/SOFTWARE

The AARL Signal Processor analog output is digitized by a Datel 100 KHz analog to digital converter with a ten bit resolution. Prior to being sent to the computer interrupt logic, Sample & Hold No. 2's clock pulse is sent to a SN 75121 TTL driver. The clock pulse is sent simultaneously to Sample & Hold No. 2 and the computer interrupt logic and computer is alerted that the analog signal is being held for digitizing (Figure 50).

The AARL Digital Computer consists of a Harris 6024/5 with 32K of memory (24 bit word size), and operates under an "on-line" real time data acquisition system (20). After the analog signal has been digitized by the 100 kHz A/D converter and processed by the AARL Computer, the data is spooled out to the AARL 450 LPM printer. During the time that the analog signal is being digitized, all information is being stored on a 9-track 800 BPI magnetic tape for later use.

The comparisons between the experimentally determined particle velocities as determined in this study, and the theoretical values are presented in Section 6.0. The data is digitized by the A/D converter and processed by the AARL Digital Computer before being spooled out to the AARL 450 LPM printer.

As a basic requirement, the instantaneous velocity of the particle is measured while an image of the doppler signal is obtained on the Tektronix Type 555 dual-beam oscilloscope to determine particle size before being filtered.

In the data acquisition mode, the computer operator is allowed to select a series of acquisition parameters, including the number of desired LDV acquisition "windows" per run and number of LDV samples desired. LDV data collection is accomplished on a wait-interrupt basis; e.g., upon processor output full interrupt is fired within a certain maximum period. The Sample & Hold No. 2 is received by the 100 kHz A/D converter and the software resets to wait for another interrupt. However, it must be noted that this reset process requires  $\sim 14$   $\mu$ sec. The interrupt is inhibited during periods between LDV sampling windows, at which time particle container weight is periodically sampled and displayed to the operator via an alphanumeric-graphic CRT to provide data on particle feed rates. These periods are typically five to ten seconds in length.

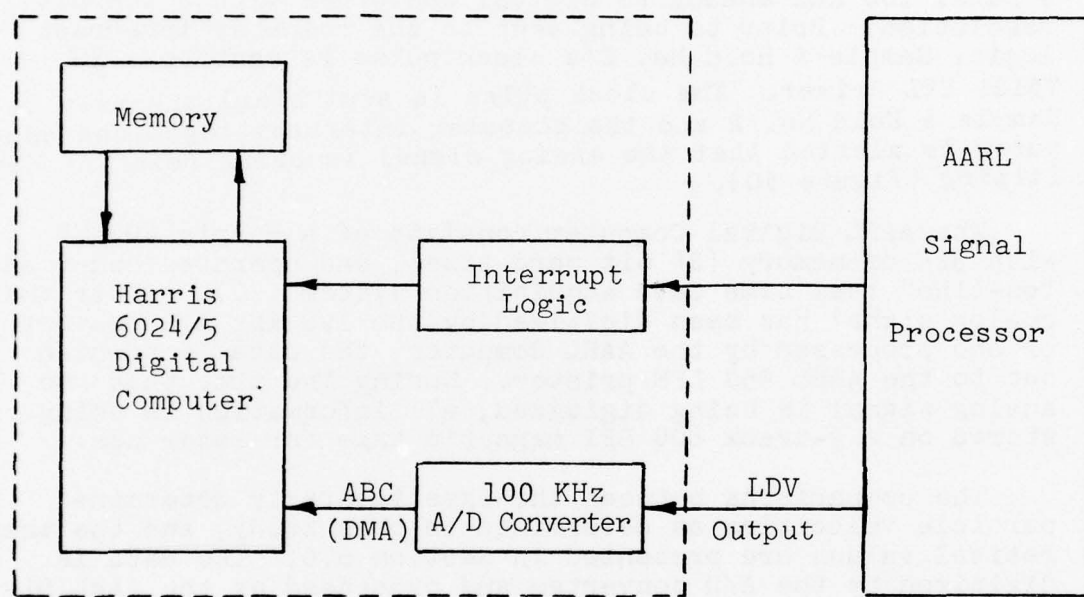


FIGURE 50. LASER DOPPLER VELOCIMETER SIGNAL PROCESSOR COMPUTER INTERFACE BLOCK DIAGRAM.

Following the test run, the raw data is stored on magnetic tape and reduction of the data is initiated. Average particle mass flow rates are calculated from the particle container weight data by forward differencing formulas, and hard copy plots of container weight vs. run time are prepared.

Particle velocity histograms for each LDV acquisition window are then displayed to the operator via the CRT, and hard-copy provided. In addition, a standard statistics software package is used to provide information about the set of particle velocity samples, which usually number 2000 for each window. For example, the average mean velocity is determined by

$$\bar{V} = \frac{1}{N} \sum_{j=1}^N V_j \quad (16)$$

whereas the standard deviation of the velocity,  $\sigma$ , is given by

$$\sigma = \sqrt{\frac{1}{N} \sum_{j=1}^N (V_j - \bar{V})^2} \quad (17)$$

Equations (16) and (17) are based on Gaussian velocity distribution and therefore, higher order moments must be used to evaluate the deviation of the histogram from a normal distribution. The deviations are usually expressed in terms of skewness and kurtosis, i.e.,

$$\text{Skewness} = \frac{\frac{1}{N} \sum_{j=1}^N (V_j - \bar{V})^3}{N\sigma^3} \quad (18)$$

where 0 indicates a symmetric distribution and a + value determines the skewness to the right or left of the central maximum, respectively. Kurtosis, or sometimes termed the flatness coefficient of fourth moment, is given by

$$\text{kurtosis} = \frac{\frac{1}{N} \sum_{j=1}^N (V_j - \bar{V})^4}{N\sigma^4} \quad (19)$$

and the value of three corresponds to a normal distribution.

## SECTION VI

### TWO-PHASE FLOW DIAGNOSTICS

The present study has involved a thorough investigation of the various components of an erosion-ablation facility, e.g., two-phase flow theoretical analyses, particle injection systems, combustion test facility including a specially designed and constructed nozzle, and each of the necessary elements of the Laser Doppler Velocimeter. It was intended to conclude the present effort by operation of the AARL Erosion-Ablation Facility including all of the peripheral components and conduct two-phase flow diagnostics. However, the magnitude of this phase has been reduced due to time restrictions and this Section contains only the preliminary results of such a study.

#### A. TEST CONDITIONS

The AARL Erosion-Ablation Facility was initially operated using air without particle injection to test the integrity of the electroformed nozzle under high pressure. Total pressures up to 1000 psig were used and the nozzle performed as expected, i.e., no visible mechanical fractures and the tunnel was easily placed into flow resulting in test cabin pressures of approximately 7 mm Hg. The next test performed was use of the H<sub>2</sub>-air combustor to obtain total temperatures on the order of 3000°F. The combustor ignited easily and the facility with the aid of the ejectors was placed into flow with total conditions corresponding to P<sub>0</sub> of 250 psig and T<sub>0</sub> of 2000°F. Higher values of total conditions could have been achieved, however because of the limitations of the water-cooled jacket surrounding the electroformed nozzle, it was decided to maintain these conditions and inject particles to test not only the particle injection system but also investigate if the signal level was adequate for operation of the AARL Signal Processor. The results of these tests indicated that the particle injector system described earlier had functioned properly, however the signal level was not adequate (200 mv) for operation of the AARL Signal Processor. As a result, no data corresponding to the combustion P<sub>0</sub>, T<sub>0</sub> condition was obtained. However, tests were conducted for cold flow at high pressure in which the particle velocity and particle size analysis were obtained by means of the Tektronic 5441 Variable Persistence Storage Oscilloscope.

Establishment of the optical arrangement given in Figure 28 results in the fringe pattern after magnification

shown in Figure 51. The 0.003-inch wire was placed in front of the eye piece to verify the spacing which is approximately 87 microns. This pattern was monitored during the tests to check alignment and also to determine the effect of vibration from operation of the facility. Using the Tektronic 5441 Scope, doppler traces of the particles were obtained (Figure 52) to determine both particle size and velocity.

#### B. PARTICLE VELOCITY/SIZE ANALYSIS

The particle velocity may be obtained from photographs of the doppler traces by using the known time base of the scope. However, the particle size is found by the visibility function,  $V$ , which is defined as the ratio of the AC to DC components of the observed scattered signal, i.e.,

$$V = \frac{I_{\max} - I_{\min}}{I_{\max} + I_{\min}} \quad (20)$$

where  $I_{\max}$  is the maximum scattered intensity from a bright fringe and  $I_{\min}$  is the corresponding minimum scattered intensity from the next consecutive dark fringe. The visibility function, as shown by Farmer (21, 22), can be reduced to a spherical particle diameter/fringe spacing parameter analytically which is expressed as

$$V \approx \frac{2J_1(\pi d/\delta)}{(\pi d/\delta)} \quad (21)$$

where  $J_1$  is a first-order Bessel function with argument  $(\pi d/\delta)$ . As pointed out by Gieseke, et al. (23), the multi-nodal nature of  $V$  can lead to ambiguous results, and therefore should not be employed for values greater than  $d/\delta \approx 1.1$ .

With the aid of Figure 53, which shows Equation (21) and an approximation proposed by Gieseke, et al. (23), doppler signatures were evaluated to yield particle velocities and diameters with the results shown in Figure 54. The data shown in this Figure for three total pressure conditions indicates that the nozzle did exhibit an inviscid core and accelerated the particles to velocities corresponding to approximately 70% of the gaseous flow. Note that only the predominant particle classes were observed, i.e., particle diameters ranging from 30 to 95 microns which corresponds to the classes in Figure 4. No comparisons were made with the

theoretical results described earlier due to the difference in total gaseous conditions.

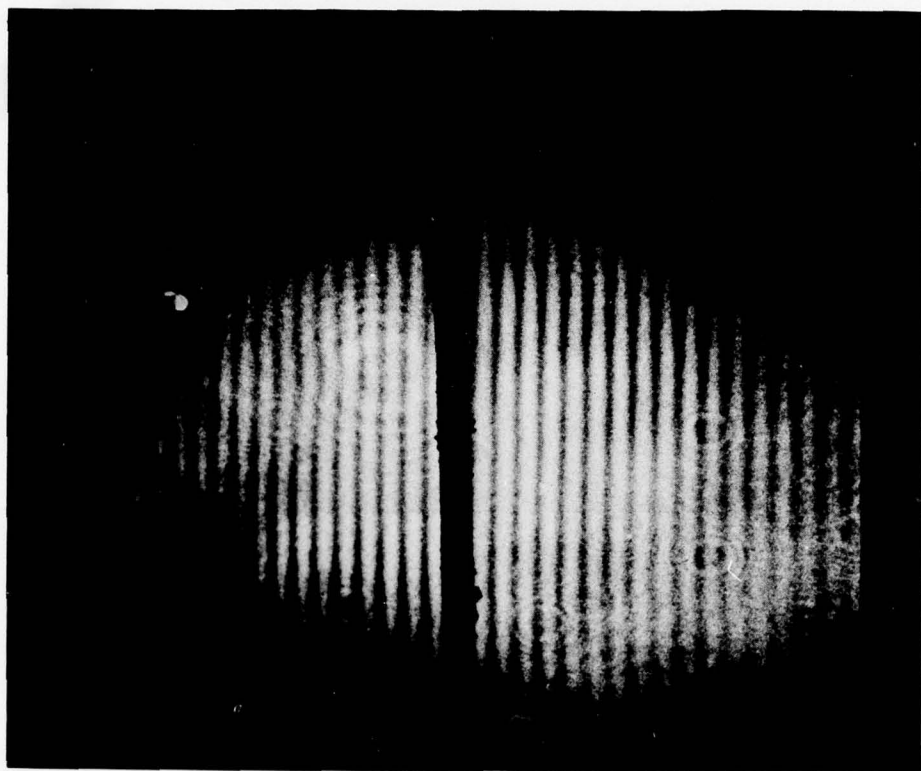
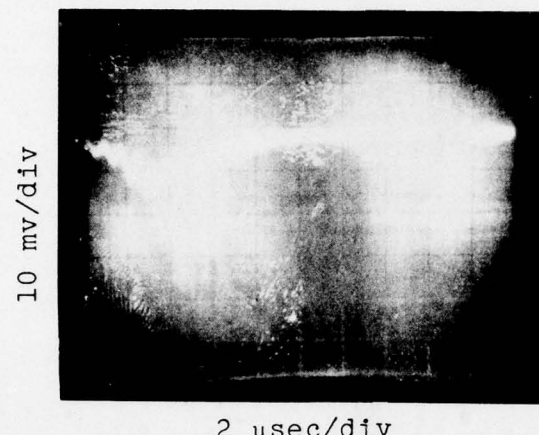


FIGURE 51. FRINGE PATTERN OBTAINED UTILIZING PRESENT  
OPTICAL ARRANGEMENT (WIRE DIAMETER 0.003 INCHES).



10 mv/div

2  $\mu$ sec/div



10 mv/div

2  $\mu$ sec/div

FIGURE 52. TYPICAL DOPPLER TRACES OF PARTICLES UTILIZING PRESENT OPTICAL ARRANGEMENT.

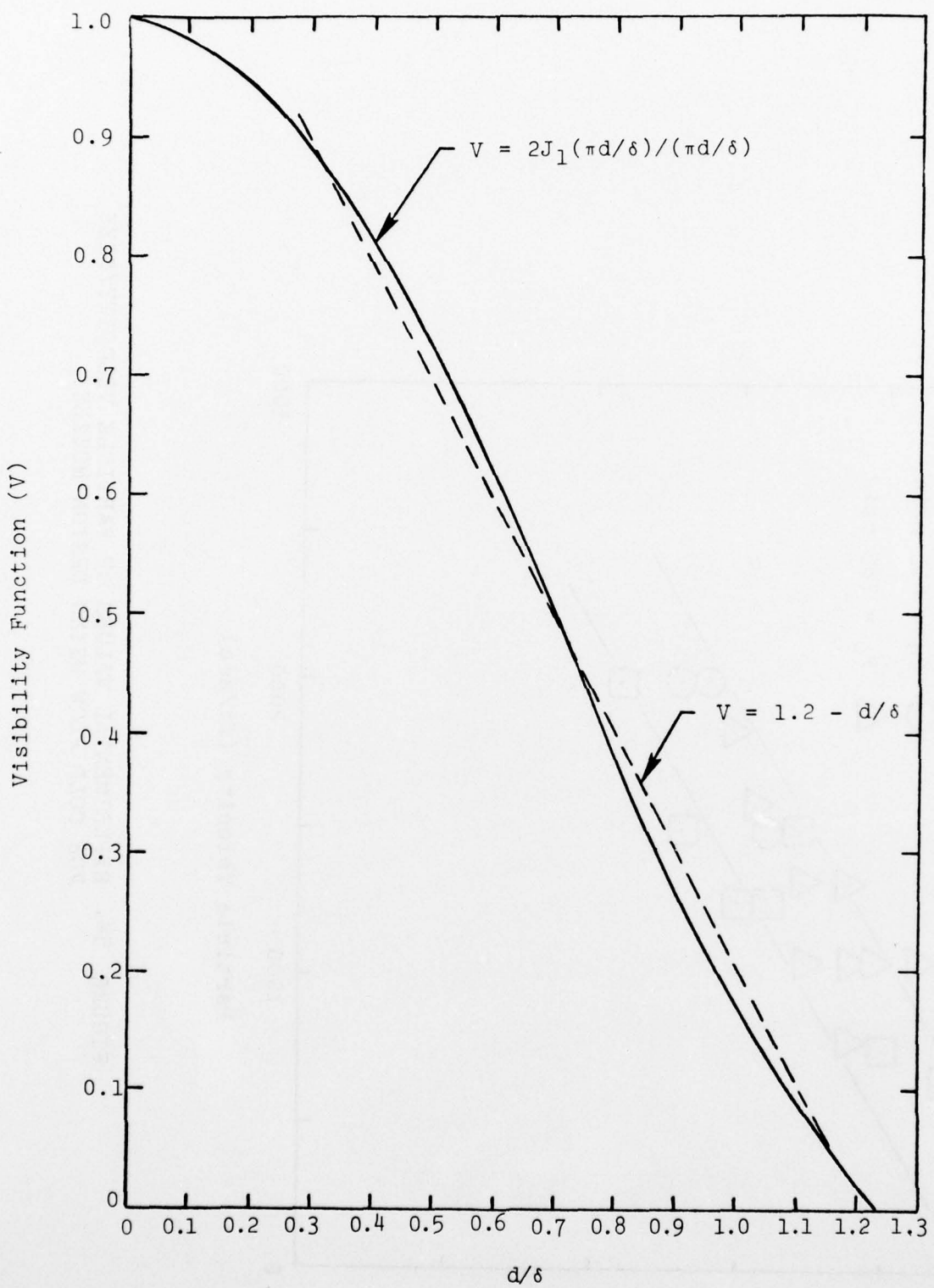


FIGURE 53. PARTICLE DIAMETER/FRINGE SPACING RATIO VERSUS VISIBILITY FUNCTION.

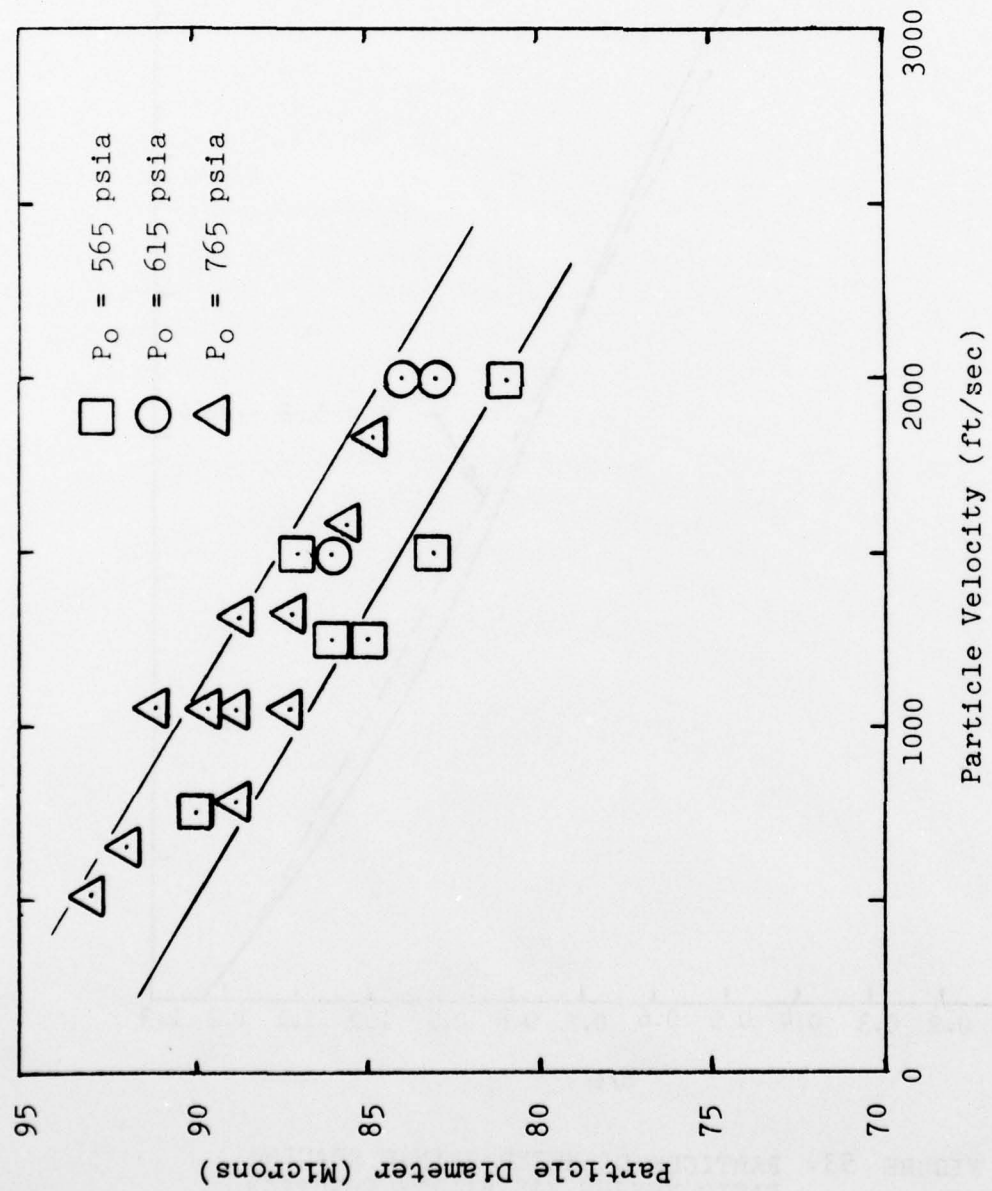


FIGURE 54. EXPERIMENTAL VALUES OF PARTICLE VELOCITY/SIZE FOR COLD FLOW USING DESIGN NOZZLE.

## SECTION VII

### SUMMARY AND CONCLUSIONS

A systematic theoretical study has been conducted to investigate the geometrical and fluid mechanical parameters that affect particle velocities. It has been found that the parameter  $\tan \zeta / R_*$  is the predominant factor and should be minimized to obtain maximum particle velocities. Also, the present study also indicates that there is an upper limit in terms of nozzle length beyond which no appreciable gain in particle velocity is attained. Theoretical studies of both coupled/uncoupled two-phase flow have been conducted and have shown that there is a significant effect when theoretically considering coupled flow for particle loadings in excess of 10% for both particle velocity and temperature. Experimental studies were conducted on various particle injection schemes in order to arrive at a system that could be accurately controlled. A total of four different methods were examined to control particle loadings up to 10%. The various particle injection techniques were evaluated by a laser scattering approach to determine qualitatively the consistency of particle feed in addition to cantilevered beam/strain gage arrangement to quantitatively measure particle mass flow rate. The results indicate that the use of a slurry consisting of  $\text{SiO}_2$  particles and  $\text{H}_2\text{O}$  in a volume ratio of 1/1 and use of a pressurized particle container equipped with an orifice and mixer results in a particle injection system that can be controlled and free from clogs and bursts. Experimental correlations have been determined to predict the particle mass flow rate as a function of pressure differential. An erosion-ablation  $\text{H}_2$ -air combustion test facility was constructed to obtain the necessary total enthalpies to simulate the ablation environment after a theoretical investigation and comparison of  $\text{H}_2\text{-O}_2$ ,  $\text{H}_2\text{-air}$ , and  $\text{CH}_4\text{-O}_2$  mixtures was accomplished. The erosion-ablation facility utilized an electroformed nozzle with a total angle of one degree and length of 2.86 feet. The facility performed satisfactorily including the nozzle and particle injection system for total pressures up to 1000 psig and total temperatures on the order of  $2400^\circ\text{R}$ . A Laser Doppler Velocimeter was used with an optical arrangement which yielded a fringe spacing of 87 microns. A Signal Processor was assembled with time-amplitude convertors to measure particle velocities and sizes for  $\text{SiO}_2$  whose particle diameters ranged from 20 to 100 microns. Although the AARL Signal Processor was checked and found to function properly using a signal generator up to 50 MHz with the appropriate filter network, no data was taken due to an insufficient

signal level (200 mv) in addition to difficulties encountered with the preamplifier. However, data was taken by analyzing the doppler signatures resulting in particle velocities up to approximately 1800 fps for a range of particle diameters from 80 to 95 microns. This result indicated that the nozzle did maintain the inviscid core and accelerated the particles as predicted in the theoretical analysis.

APPENDIX A

AARL SIGNAL PROCESSOR WIRING DIAGRAMS

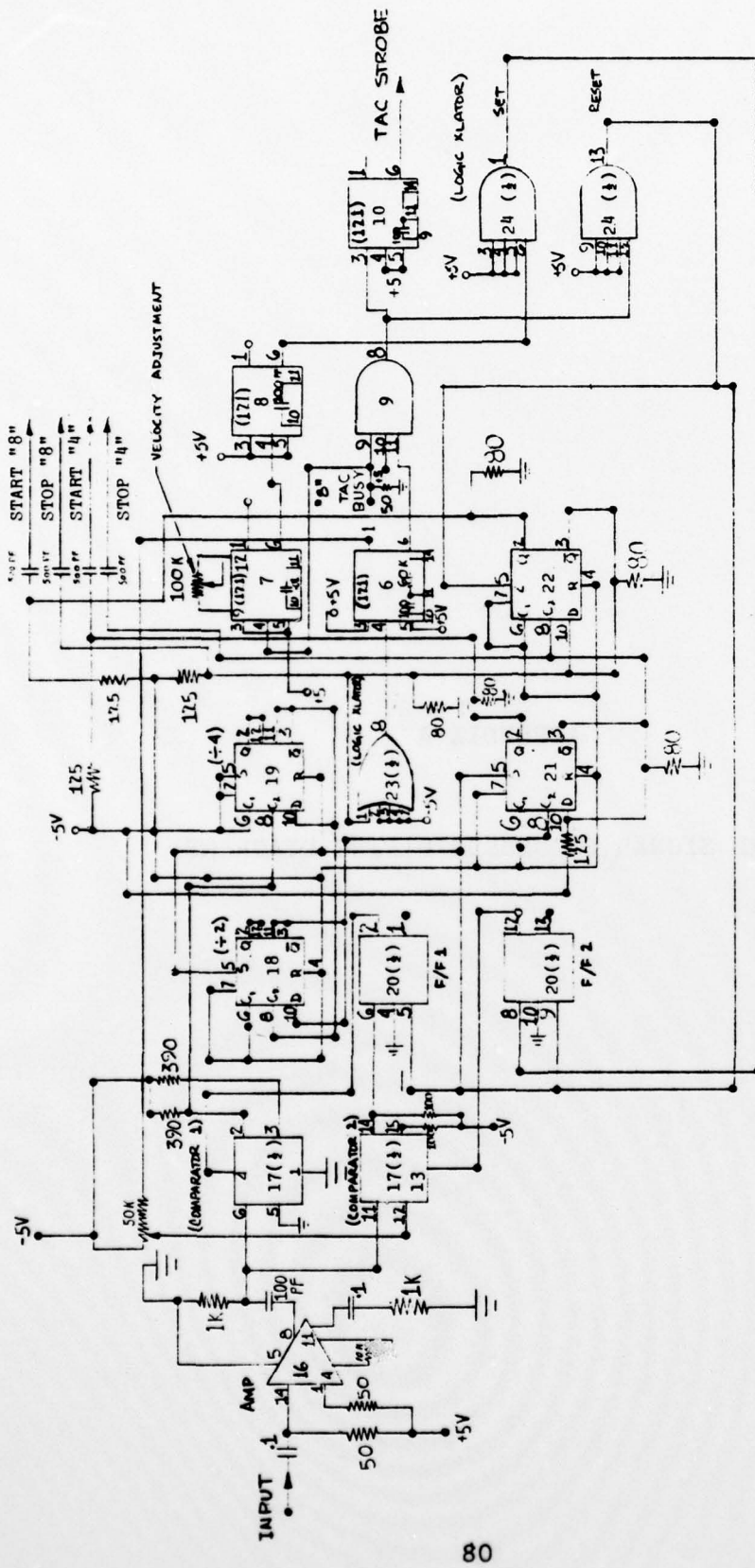


FIGURE A-1. SIGNAL PROCESSOR CIRCUIT DIAGRAM PRIOR TO TAC ENTRY (PC BOARD NO. 1).

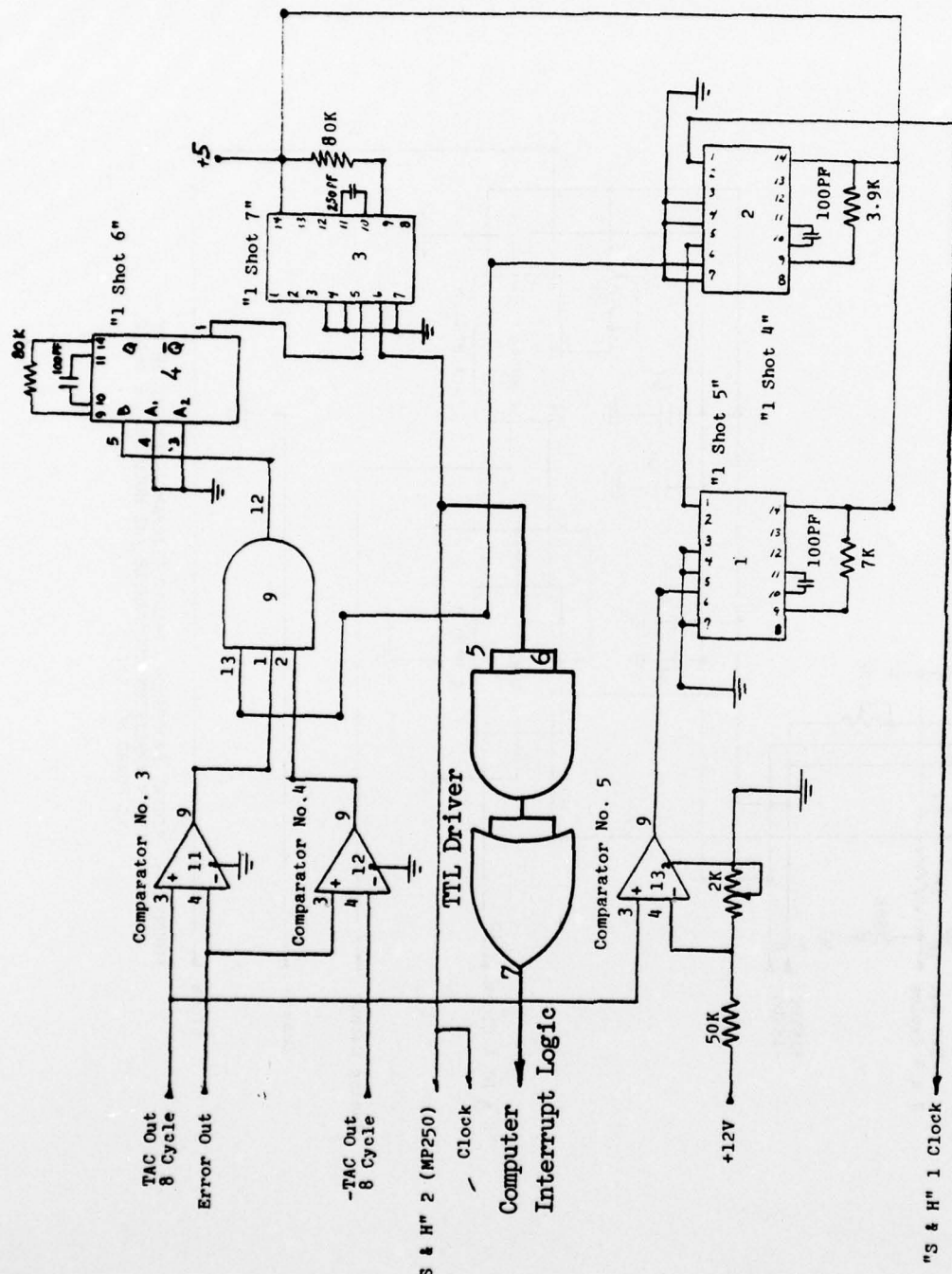


FIGURE A-2. SIGNAL PROCESSOR CIRCUIT DIAGRAM AFTER TAC ENTRY -  
SAMPLE AND HOLD NO.'S 1 AND 2 TIMING (PC BOARD NO. 1).

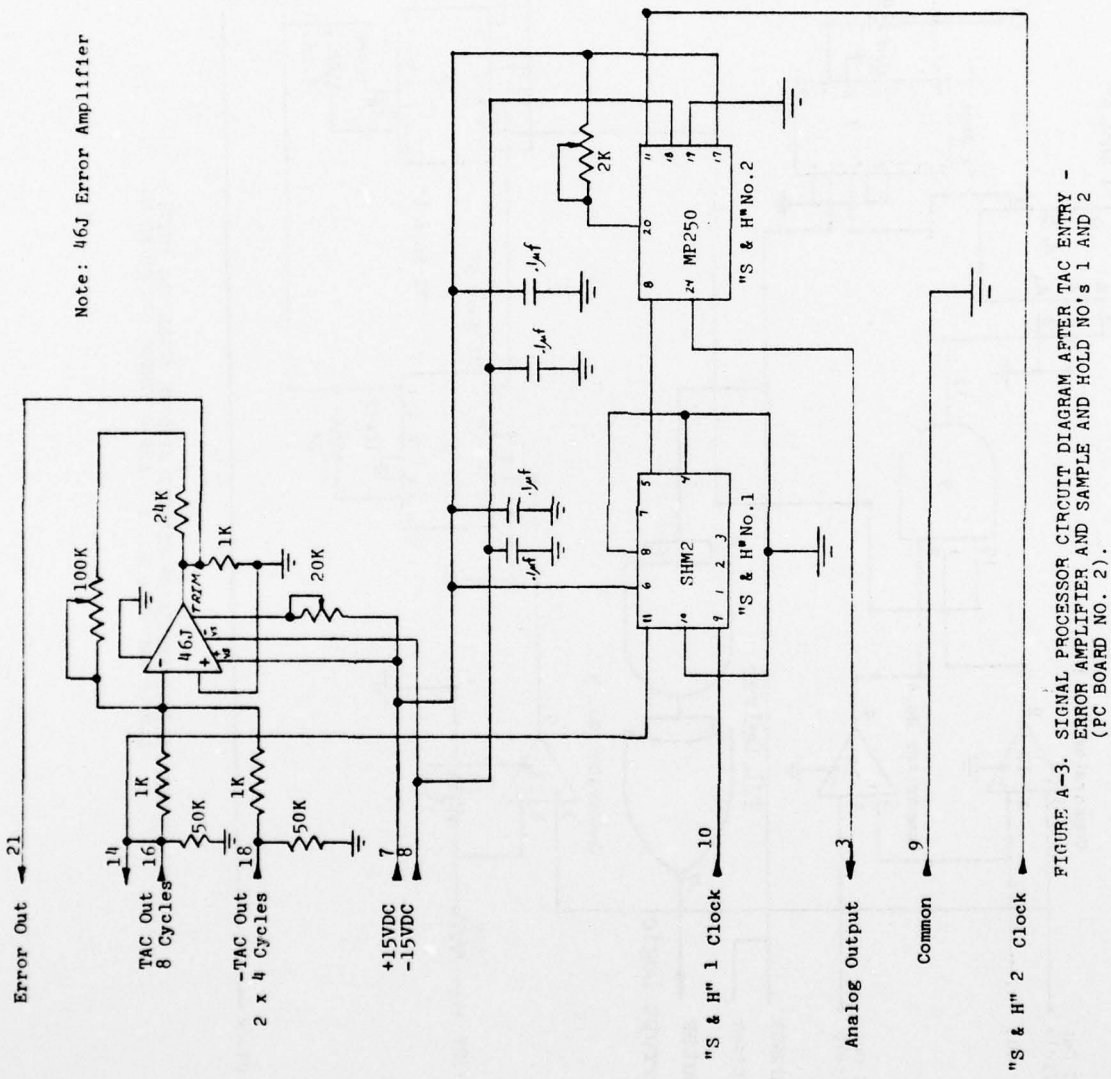


FIGURE A-3. SIGNAL PROCESSOR CIRCUIT DIAGRAM AFTER TAC ENTRY -  
ERROR AMPLIFIER AND SAMPLE AND HOLD NO'S 1 AND 2  
(PC BOARD NO. 2).

APPENDIX B

AARL SIGNAL PROCESSOR PARTS LIST

AARL PROCESSOR PARTS LIST

Board No. 1

<u>Part</u>	<u>Device Number</u>	<u>Manufacturer</u>	<u>Function</u>
I.C. 16	SN72733	Texas Inst.	Amplifier
I.C. 17	MC1650 L	Motorola	Comparators 1 & 2
I.C. 18	MC1034	Motorola	Binaries Used in the ÷4 and ÷2 Counters
I.C. 19	MC1034	Motorola	
I.C. 21	MC1034	Motorola	
I.C. 22	MC1034	Motorola	
I.C. 20	MC1014	Motorola	Flip-Flops 1 & 2
I.C. 23	MC1018	Motorola	Logic Trans- lator
I.C. 6	SN74121	Texas Inst.	One Shot 1
I.C. 10	SN74121	Texas Inst.	One Shot 2
I.C. 9	SN7421	Texas Inst.	AND Gate
I.C. 7*	SN74121	Texas Inst.	One Shot 8
I.C. 8	SN74121	Texas Inst.	One Shot 3
I.C. 24	MC1017	Motorola	Logic Trans- lator

AD-A053 809 OHIO STATE UNIV COLUMBUS AERONAUTICAL AND ASTRONAUTI--ETC F/G 20/4  
ADVANCED TWO-PHASE INVESTIGATION IN AN EROSION-ABLATION FACILITY--ETC(U)  
AUG 77 K D KORKAN, S L PETRIE, T S RICE F33615-76-C-3002  
UNCLASSIFIED AFFDL-TR-77-78 NL

2 OF 2  
AD  
A053809



END  
DATE  
FILED  
6 -78  
DDC

AARL PROCESSOR PARTS LIST (continued)

Board No. 2

46J	46J	Analog Devices	Error Amplifier
I.C. 11	MC1710C	Motorola	Comparator 3
I.C. 12	MC1710C	Motorola	Comparator 4
I.C. 3	SN74121	Texas Inst.	One Shot 7
I.C. 4	SN74121	Texas Inst.	One Shot 6
I.C. 2	SN74121	Texas Inst.	One Shot 4
I.C. 1	SN74121	Texas Inst.	One Shot 5
I.C. 13	MC1710	Motorola	Comparator 5
SHM 2	SHM 2	Datel	Sample & Hold 1
MP250	MP250	Analogic	Sample & Hold 2

Input Filters

<u>Manufacturer</u>	<u>Cutoff Frequencies and Type</u>
Allen Avionics	3 MHz highpass
	20 MHz highpass
	7 MHz highpass
	70 MHz lowpass
	70 MHz lowpass
	50 MHz lowpass

## REFERENCES

1. Lewis, H. F., "Description and Calibration Results of the AEDC Dust Erosion Tunnel," AEDC-TR-73-74 (May 1973).
2. Dunbar, L. E., Courtney, J. F., and McMillen, L. D., "Heating Augmentation in Erosive Hypersonic Environments," AIAA J. 13, No. 7, pp. 908-912 (1975).
3. Johnson, E. G., MacDermott, W. N., and Kessel, P. A., "Prospects for an Ablation/Erosion Facility Employing the RHEA Concept," AIAA Paper No. 74-605, AIAA 8th Aerodynamic Testing Conference, Bethesda, Maryland (July 1974).
4. Fewell, K. P. and Kessel, P. A., "Analysis Design, and Testing of Components of a Combined Ablation/Erosion Nozzle," AEDC-TR-75-154 (March 1976).
5. Korkan, K. D., Petrie, S. L., and Bodonyi, R. J., "Particle Concentrations in High Mach Number Two-Phase Flows," ARL TR 74-0102 (July 1974).
6. Korkan, K. D., "Theoretical and Experimental Studies of Multicomponent Flow Systems," Dissertation presented in partial fulfillment of the requirements for the Degree Doctor of Philosophy, The Ohio State University (June 1975).
7. Bailey, W. S., Nilson, E. N., Serra, R. A., and Zupnik, T. F., "Gas Particle Flow in an Axisymmetric Nozzle," ARS J. 31, 793-798 (1961).
8. Carlson, D. J. and Hoglund, R. F., "Particle Drag and Heat Transfer in Rocket Nozzles," AIAA J. 2, 1980-1984 (1964).
9. Petrie, S. L., "A Preliminary Study of the Hypersonic Flow of Helium-Air Mixtures," Aerospace Research Laboratories, Wright-Patterson AFB, Ohio, ARL 62-375 (July 1962).
10. Gordon, S. and McBride, B. J., "Computer Program for Calculation of Complex Chemical Equilibrium Compositions, Rocket Performance, Incident and Reflected Shocks, and Chapman-Jouguet Detonations," NASA SP-273 (1971).
11. Lee, J. D., "Axisymmetric Nozzles for Hypersonic Flows," TN(ALOSU) 459-1, The Ohio State University (June 1959).
12. Turman, B. N., "Private Communication," ARL/Energy Conversion Laboratory (February 1973).

13. Goldstein, R. J. and Hagen, W. F., "Turbulent Flow Measurements Utilizing the Doppler Shift of Scattered Laser Radiation," *Physics of Fluids*, 10, No. 6, pp. 1349-1352 (1967).
14. Wang, C. P. and Snyder, D., "Laser Doppler Velocimetry: Experimental Study," *Applied Optics*, 13, No. 1 (1974).
15. Meyers, J. F. and Feller, W. V., "Processing of the Laser Doppler Velocimeter Signals," Presented at the Fifth International Congress on Instrumentation in Aerospace Simulation Facilities, Pasadena, California (September 1973).
16. Thompson, H. D. and Stevenson, W. H., editors, "The Use of the Laser Doppler Velocimeter for Flow Measurements," Proceedings of the Second International Workshop held at Purdue University, West Lafayette, Indiana (March 1974).
17. Zammit, R. E., "The Design and Operation of a High Frequency Burst Signal Processor for Laser Doppler Velocimeter Applications," Ph.D. Dissertation, Purdue University, West Lafayette, Indiana (May 1975).
18. Zammit, R. E., Pedigo, M. K., and Stevenson, W. H., "A High Frequency Burst Signal Processor for Laser Velocimeter Applications," U.S. Army Missile Command Report No. RD-CR-74-4 (January 1973).
19. Rudd, M. J., "A New Theoretical Model for the Laser Doppler-meter," *J. of Physics E. Series 2*, 2, pp. 55-58 (1969).
20. Freuler, R. J., "State-of-the-Art Data Acquisition and Reduction Techniques for Transonic Airfoil Testing," Paper presented to the International Congress on Instrumentation in Aerospace Simulation Facilities, Ottawa, Canada (September 1975).
21. Farmer, W.M., "Measurement of Particle Size, Number Density, and Velocity Using a Laser Interferometer," *Applied Optics*, 11, 2603-2612 (1972).
22. Farmer, W. M., et al., Spectron Development Laboratories, Inc., Report SDL-756805.
23. Gieseke, J. A., Boiarski, A. A., Schmidt, E. W., Barnes, R. H., and Luce, R. G., "Atomization and Evaporation of Fuel for Turbine Combustors: Phase I, Experimental Spray Measurement Feasibility," BATTELLE Columbus Laboratories (25 January 1976).